



Etude de la dérive et de la déformation de la banquise Arctique par l'analyse de trajectoires Lagrangiennes

Pierre Rampal

► To cite this version:

Pierre Rampal. Etude de la dérive et de la déformation de la banquise Arctique par l'analyse de trajectoires Lagrangiennes. Océan, Atmosphère. Université Joseph-Fourier - Grenoble I, 2008. Français.
NNT : . tel-00352799

HAL Id: tel-00352799

<https://theses.hal.science/tel-00352799>

Submitted on 13 Jan 2009

HAL is a multi-disciplinary open access archive for the deposit and dissemination of scientific research documents, whether they are published or not. The documents may come from teaching and research institutions in France or abroad, or from public or private research centers.

L'archive ouverte pluridisciplinaire **HAL**, est destinée au dépôt et à la diffusion de documents scientifiques de niveau recherche, publiés ou non, émanant des établissements d'enseignement et de recherche français ou étrangers, des laboratoires publics ou privés.



Laboratoire de Glaciologie et Géophysique de l'Environnement

LABORATOIRE DE GLACIOLOGIE
ET GEOPHYSIQUE DE L'ENVIRONNEMENT
UMR 5183

Centre National de la Recherche Scientifique

Université Joseph Fourier

54, rue Molière – Domaine Universitaire

BP 96 – 38402 Saint Martin d'Hères Cedex (France)

Etude de la dérive et de la déformation de la banquise Arctique par l'analyse de trajectoires lagrangiennes

Pierre RAMPAL

Thèse de doctorat de l'Université Joseph Fourier (Grenoble 1)

Spécialité : Sciences de la Terre et de l'Univers

Date de Soutenance : 6 novembre 2008

Composition du jury :

M. Bernard BARNIER

Président du Jury

M. Stéphane ROUX

Rapporteur

M. Jean-François PINTON

Rapporteur

M. Jean-Claude GASCARD

Examinateur

M. Martin DOBLE

Examinateur

M. Jérôme WEISS

Directeur de thèse

M. David MARSAN

Co-directeur de thèse



Remerciements

Avant toute chose, je vais tenter de me soumettre à l'exercice difficile que constitue la rédaction des remerciements... Difficile non pas parce que je n'en ai aucun à faire ! Mais plutôt le contraire...

Pour commencer, je souhaiterais remercier sincèrement Stéphane Roux et Jean-François Pinton d'avoir accepter de rapporter ce travail. J'ai été profondément honoré que ce soit eux, et positivement impressionné lors de la soutenance par leur gentillesse et la qualité de leurs commentaires. J'espère que j'aurai l'occasion de les recroiser très vite, de près ou de loin, afin de les écouter encore. En effet, la traditionnelle séance de questions que j'ai partagé avec eux lors de la soutenance, séance tant redoutée parfois, m'est apparue vraiment trop courte...

Merci également à Jean-Claude Gascard qui, ne pouvant finalement pas être présent le jour même, nous a fait l'amitié de se déplacer quelques jours avant la soutenance afin d'écouter ma présentation et de rédiger un rapport sur mon travail. Tout cela en 4h chrono de Paris à Paris.

Bien évidemment, je remercie aussi Bernard Barnier qui endossa le brassard de président du Jury, et Martin Doble qui, malgré les grèves de train, parvint à rallier Nice et Grenoble en une petite demi-journée...

Comment ne pas mentionner largement ici l'immense respect ainsi que les plus sincères remerciements à mes directeurs de thèse...? En effet, j'ai eu la chance d'en avoir deux. Pour moi, Jérôme et David ne firent pourtant qu'un, tant leur complémentarité aussi bien sur le plan scientifique qu'humain est totale. Cette dernière m'aura permis de me former tout en m'ouvrant l'esprit et en excitant pour longtemps je crois, ma curiosité scientifique. Au-delà de cela, ils m'auront fait grandir, tout simplement... Ils auront su, je le crois, me préparer de la meilleure façon qu'il soit au métier d'enseignant-chercheur. J'insiste ici sur « enseignant » car ils ont fait preuve d'une grande pédagogie tout au long de ces trois ans, chose qui à mon avis est indispensable mais qui reste rare dans le monde de la recherche. En ces jours où le maître mot est « l'excellence », et malgré le fait que je n'affectionne pas particulièrement ce qualificatif dans certaines situations, je pense pouvoir dire aujourd'hui que Jérôme et David sont excellents. Merci encore, pour tout...

Je remercie l'ensemble des personnels du LGGE, mon laboratoire d'accueil, ainsi que ceux du LGIT, mon laboratoire d'accueil par intermittence.... Ils sont très nombreux, et je ne pourrai donc pas les nommer ici. Mais je pense à eux en rédigeant ces lignes.

Merci également à mes ami(e)s et collègues qui ont partagé avec moi quelques bouts de vie plus ou moins longs au cours des trois dernières années, et dont voici une liste qui est loin d'être exhaustive : Manu (qui est le premier, et qui sera le dernier), Sisi, Poussimon, Pycotte, Toitoine, Le pti spaghetti, Suave, Lucas, ma Fofie..., Sebouille, ma voisine de bureau préférée qui se reconnaîtra..., Hélène, Christine, Winnie d'en face, et tant d'autres.... Un grand merci à Isa (alias doudou), qui m'a épaulé, supporté, et beaucoup fait grandir aussi (oui je sais... pas vraiment en taille!). Merci au petit lardinou, pour ce que nous avons partagé depuis un an, et ce que nous partagerons dans le futur... ainsi qu'à Gillian, Didou et Natach pour m'avoir adopté comme vous l'avez fait.

Enfin, et non le moins important, je tiens à terminer ces remerciements avec ceux que j'adresse à toute ma famille, qui depuis le début est présente juste ce qu'il faut, quand il le faut... et qui le sera dans le futur, j'en suis absolument certain. Quelle chance inestimable...

Résumé

La banquise arctique est une plaque de glace flottant à la surface de l'océan sur plusieurs millions de km². La variation spatiale et temporelle de son épaisseur contrôle les échanges d'énergie mécanique et thermique entre l'atmosphère et l'océan. De ce fait, la banquise est une sorte d'isolant pour l'océan arctique, qui lui même joue un rôle déterminant dans la circulation thermohaline de l'océan mondial, et par voie de conséquence sur le climat de la planète.

On observe une disparition significative et progressive de la banquise depuis environ un demi siècle, disparition qui s'est accélérée au cours des dernières années, a tel point qu'elle dépasse les prévisions les plus alarmistes des modèles les plus sophistiqués.

Nous montrons dans cette thèse que cette sous-estimation pourrait être le résultat de l'utilisation d'un cadre de modélisation inadéquat : en considérant la banquise comme un milieu continu fluide, les modèles actuels ne parviennent pas à reproduire, entre autres, les propriétés d'intermittence et d'hétérogénéité de son champs de déformation que nous mettons en évidence. De ce fait, la fracturation de la banquise, bien que largement observable sur le terrain et/ou par satellite, n'est pas correctement reproduite. Or, elle apparaît comme essentielle au regard de son contrôle sur le caractère isolant décrit plus haut.

Dans ce travail, nous suggérons également d'adopter un nouveau schéma de modélisation, considérant la banquise comme une plaque rigide ayant un comportement mécanique elasto-fragile.

Abstract

The arctic sea ice is a solid plate that floats on the ocean over several millions of squared kilometers. Temporal and spatial variations of the sea ice thickness control the mechanical and thermal exchanges between the arctic atmosphere and the Arctic Ocean. This later plays a fundamental role on the thermohaline circulation, and consequently, on the earth climate. Thus, as it isolates the ocean from the atmosphere, the sea ice cover can be viewed as a key parameter of the global climate. Since approximately five decades, we can observe a significant sea ice shrinking, which accelerated during the last years. All the most sophisticated global climate models under-estimate this acceleration.

In this work, we show that this under-estimation can be due to the modeling framework used in these models: indeed, the sea ice cover is modeled as a viscous plastic material and, as an example, do not exhibit some fundamental properties of its dynamics, i.e. the intermittency and the heterogeneity of its deformation field. Then, the induced fracturing of the sea ice cover is not reproduced, and its consequences in terms of energy exchanges between the atmosphere and the ocean are neglected.

We suggest that the arctic sea ice has to be considered as a deforming solid plate, and modeled with an alesto-brittle rheology.

A mes deux pères...

...représentant à mes yeux respectivement la Mathématique et la Physique dans tout ce qu'elles ont de plus noble,

mais aussi tant d'autres choses...

Table des matières

Résumé	5
Table des matières	9
Introduction	13
Contexte: le recul de la banquise Arctique	13
Rôle de la banquise Arctique dans le climat	19
Variation du flux d'eau «douce» à la surface de l'océan	19
Rôle d'isolant de la banquise Arctique	19
La boucle de rétroaction de l'albédo	20
La banquise dans les modèles de climat global (MCG)	23
La banquise : un fluide visqueux ?	23
Evaluation des modèles de banquise	25
Les observations de la banquise Arctique	27
Objectifs et organisation du mémoire	29
Chapitre I : Evolution récente de la vitesse de dérive et du taux de déformation de la banquise Arctique	31
1. Introduction	33
2. Dataset	35
3. Analysis of the time variation of buoy speed	39
3.1 Monthly averages of buoy speed	39
3.2 Seasonal averages of buoy speed	42
4. Are the mean IABP buoy speeds représentative of the mean Arctic sea ice speeds ?	43
4.1 Constructing the mean speed fields	44
4.2 Monthly mean speeds estimated from the interpolated speed fields	46
5. Increase of the mean déformation rate of the sea ice cover over the last 29 years	47
5.1 Relation between dispersion of buoys and sea ice déformation	48
5.2 Results	50
6. Discussion	51
6.1 External forcing	52
6.2 Sea ice déformation, thinning and export	54
6.3 Year 2007	56
7. Conclusion	59
Appendix-I	60

Chapitre II : Champ de vitesse de la banquise Arctique	61
1. Introduction	63
2. Dataset: Lagrangian trajectories of buoys	65
3. Estimating the mean velocity field $\langle \mathbf{u}(\mathbf{x}, t) \rangle$ of the Arctic sea ice	67
3.1 Classical approach: the turbulent diffusion theory (Taylor, 1921)	68
3.2 Definition of the mean velocity $\langle \mathbf{u} \rangle$	70
3.3 Methodology	73
3.4 Results and conclusions	75
3.5 Discussion	78
4. Analyzing the fluctuating velocity field of Arctic sea ice	81
4.1 Spectral analysis	82
4.2 Distributions of fluctuating velocity	85
4.3 Intermittency and scaling	87
4.4 Diffusion regimes of sea ice	90
4.5 Discussion.....	93
5. Conclusion	95
Chapitre III : Champ de déformation de la banquise Arctique	97
1. Introduction	99
2. Dataset	103
3. Methodology	105
4. Introduction to the dispersion process: two examples of buoy dispersions	107
5. Sea ice dispersion and deformation over the whole Arctic Ocean: Results	115
5.1 Time scaling	115
5.2 Spatial scaling	117
6. Discussion	119
6.1 Time scaling.....	119
6.2 Spatial scaling	120
6.3 Seasonal dynamics of sea ice	122
6.4 Perspectives for future studies	122
7. Conclusion	123
Appendix-III	124
Chapitre IV : Conclusions et perspectives	125
1. Conclusions	127
2. Discussion et perspectives	129
2.1 Intensification de la boucle de rétroaction de l'albédo	129
2.2 Prise en compte du processus de fracturation dans les modèles	130
2.3 La banquise : un objet géophysique modèle	132

2.3.1 Origine des propriétés d'échelle de la banquise Arctique	132
2.3.2 Un modèle de fracturation multi-échelle afin d'expliquer les lois d'échelle de la banquise et le couplage espace-temps associé	132
2.3.3 Conclusion	133
Bibliographie	135
Annexe	145

Introduction

1. Contexte : Le recul de la banquise Arctique

La banquise, fine pellicule de glace d'eau de mer d'une épaisseur de l'ordre du mètre, recouvre la totalité de la surface de l'Océan Arctique en hiver (~14 millions de km²), mais seulement une partie de celui-ci en été (~7 millions de km²) (Figure 1).

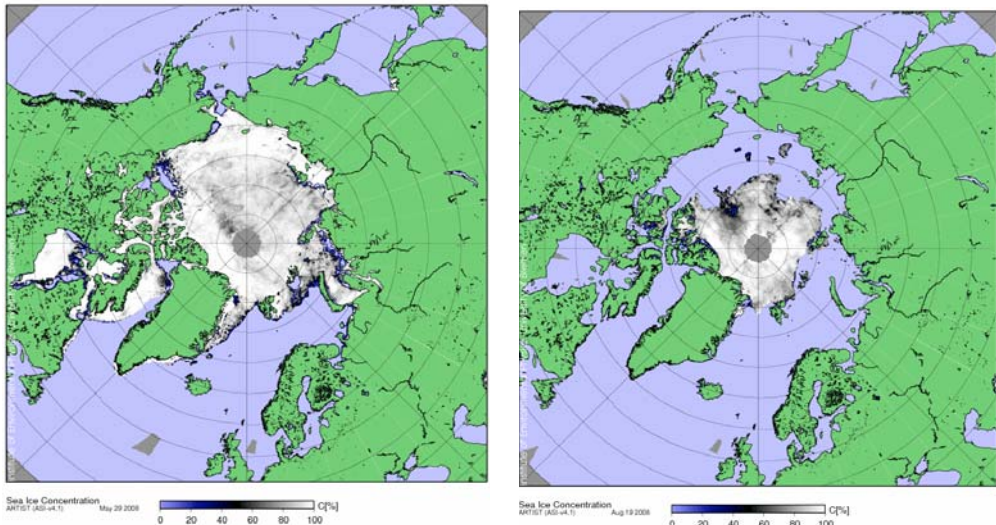


Figure 1. Concentration de glace de mer dans le bassin Arctique, à la fin de l'hiver polaire 2008 (à gauche), et durant l'été 2008 (à droite). *Source:* <http://iup.physik.uni-bremen.de:8084/>.

Les mesures satellitaires de la concentration de glace recueillies depuis la fin des années 1970 suggéraient déjà une tendance persistante à la diminution de l'étendue des glaces de mer Arctique, dans une proportion moyenne de 4 à 7% par décennie selon les études et les périodes considérées [Comiso, 2001 ; Comiso *et al.*, 2003; Serreze *et al.*, 2003; Stroeve *et al.*, 2005]. Mais elles montraient également que cette diminution, clairement visible sur l'étendue minimale de glace en été, semblait affecter principalement les glaces jeunes de l'Est de l'Arctique, au large du continent Eurasien, et restait peu perceptible en hiver. Or récemment, le radiomètre SSM/I de la NASA révélait qu'en 2005, la couverture hivernale de glace avait subi le même sort [Comiso, 2006] avec une étendue maximale, mesurée à la fin du mois de Mai, en nette diminution par rapport aux années précédentes, suivi d'un minimum record de son étendue mesurée au mois de Septembre de la même année avec 5.6 millions de km². Cette

tendance se confirma durant les hivers 2006 et 2007, avant d'atteindre un nouveau record à la fin de l'été 2007 avec 4,3 millions de km² seulement (Figure 2).

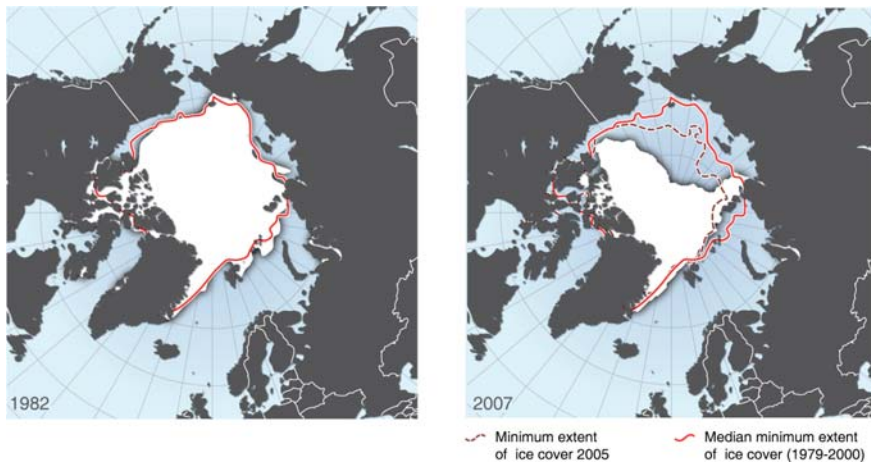


Figure 2. Etendue minimale en Septembre 1982, 2005 et 2007, montrant ainsi l'ampleur du retrait de la banquise observée ces 25 dernières années. *Source:* UNEP/GRID - Arendal Maps and Graphics Library, <http://maps.grid.no/go/graphic/arctic-sea-ice-minimum-extent-in-september-1982-2005-and-2007>.

Comiso [2002,2005] observa qu'en plus de la réduction de la couverture spatiale de la banquise, la proportion de glace de différents âges s'est fortement modifiée au cours des 30 dernières années (Figure 3), laissant apparaître la possibilité d'une disparition totale de la glace pluriannuelle (c'est à dire la glace résistant à la fonte durant au moins un été) dans les prochaines décennies. En d'autres termes, cela signifierait que l'Océan Arctique pourrait se retrouver libre de glace à la fin de chaque été, avant de régler l'hiver suivant. Dans le même temps, Rothrock *et al.* [1999, 2008] ont montré grâce à l'analyse de données de sonars recueillies par des sous-marins américains, que la banquise s'est amincie de 36% entre 1975 et 2000 sur un large domaine de l'Arctique. De manière plus générale, toutes les études récentes tendent à conclure que la disparition progressive de la banquise Arctique, en particulier estivale, semble inéluctable [Serreze *et al.*, 2007, Lemke *et al.*, 2007].

Cependant, les périodes d'observations des différents appareils de mesures restent courtes au regard de l'inertie qu'est supposée avoir la banquise en réponse aux changements de forçages auxquels elle est soumise. En effet, les séries temporelles précises d'étendue de glace atteignent tout juste 30 ans, ce qui peut sembler court pour extraire une tendance significative au sein d'un bruit interannuel important.

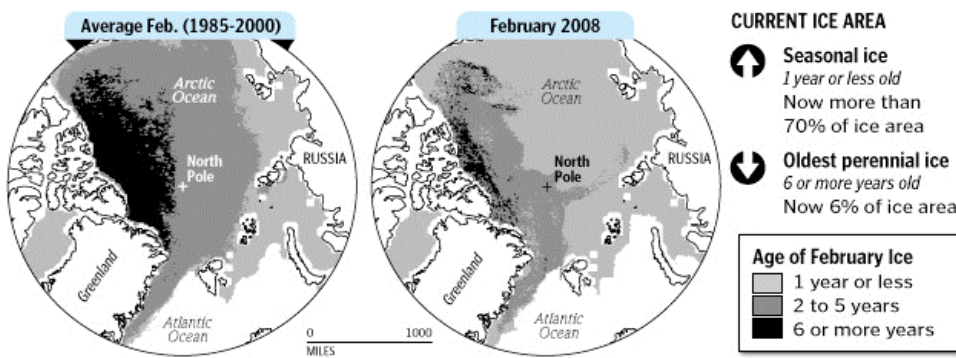


Figure 3. Proportions de glaces de mer d'âges différents dans le bassin Arctique, estimées à partir de données satellitaires de température de brillance AMSR et SSM/I. Par rapport à la moyenne des épaisseurs estimées pour les mois de Février entre 1985 et 2000, le mois de Février 2008 montre un recul exceptionnel et sans précédent des glaces pluriannuelles. *Source:* fournie par W. Meier du National Snow and Ice Data Center (NSIDC) de l'Université Boulder dans le Colorado, et publiée dans le *Washington Post* du mercredi 19 Mars 2008, en page A03.

Ainsi, au cours de ces 30 dernières années, on a pu assister à des périodes où l'étendue de glace de mer est restée quasi constante. De plus, de forts contrastes régionaux sont observés [Comiso, 2003b], liés en grande partie à la distribution spatio-temporelle inégale des réchauffements atmosphérique et océanique en Arctique. Sur les 40 dernières années, le réchauffement de l'atmosphère Arctique a été de plus de 1.3°C, soit 2 à 3 fois la valeur pour la planète [Chapman et Walsh, 2003]. Depuis l'année 2000, l'océan Arctique de surface qui entoure la banquise montre quand à lui des anomalies positives de température pouvant aller jusqu'à 5°C dans les Mers de Beaufort, Chuckchi et Sibérie de l'Est (voir carte de la figure 4) avec toutefois une variabilité interannuelle importante [Steele et al., 2008]. Une part importante de l'incertitude sur l'évolution des glaces est aussi liée à l'impossibilité jusqu'à ce jour d'obtenir une cartographie globale de leur épaisseur et d'en suivre l'évolution. La connaissance de l'épaisseur de la banquise Arctique permettrait en effet d'en évaluer sa masse et donc d'estimer l'inertie thermique de l'Océan Arctique ainsi que sa capacité à répondre aux changements climatiques observés dans cette région [Comiso, 2003; McBean et al., 2005]. Si l'on exclut le détroit de Fram par lequel la majeure partie de l'export de masse de glace s'effectue (de l'ordre de 2000 km³ par hiver en moyenne, voir Kwok et Rothrock [1999]), la banquise Arctique se situe dans un bassin confiné. De ce fait, la redistribution de l'épaisseur des glaces résulte de leur déformation/fracturation sous l'action des vents principalement, mais aussi des courants marins, conduisant à la formation de « chenaux » libres de glace (Figure 5a) ou de « crêtes de compression » (Figure 5b). L'épaisseur de la glace de mer dépend donc des champs de pression atmosphérique de surface. La circulation atmosphérique sur l'Arctique se caractérise par une suite de régimes, dominés alternativement par une hausse ou une baisse de pression au centre du bassin associée respectivement à une baisse ou une hausse de pression en périphérie du bassin.

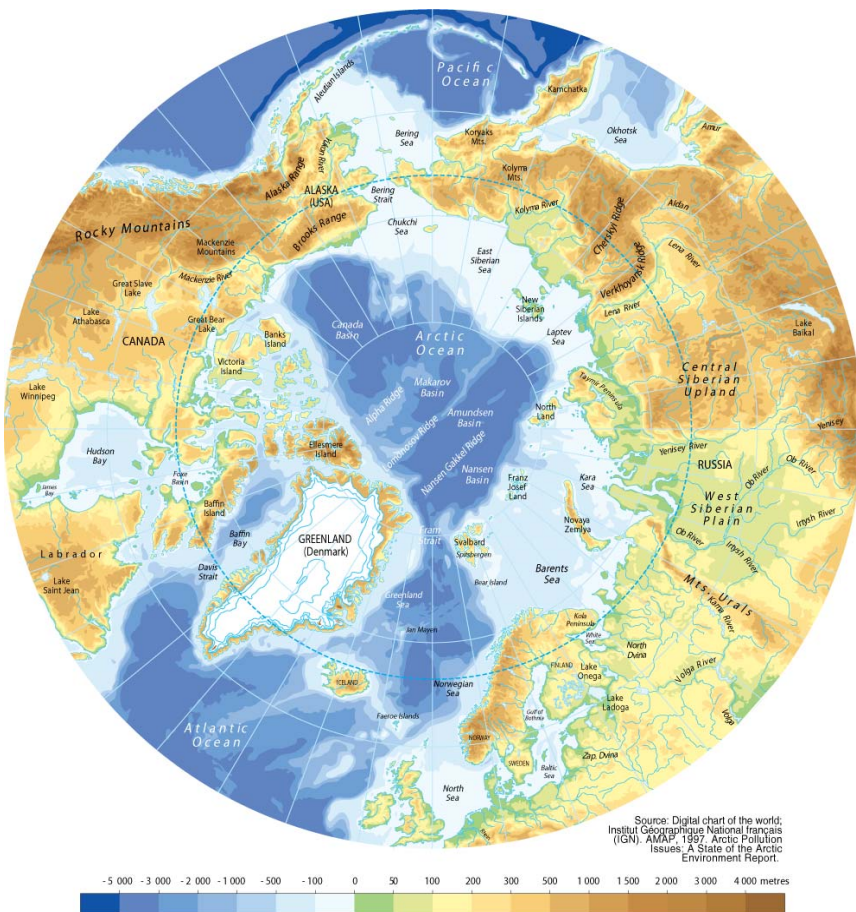


Figure 4. Carte topographique et bathymétrique de l'Arctique.

Cette alternance d'anomalie est attribuée à l'oscillation Arctique (OA). Lorsque cette dernière est en phase positive, on assiste à un transfert des glaces du bassin eurasien vers le bassin canadien conduisant à une accumulation, et donc à un épaissement, des glaces dans les régions situées au nord du Groenland et du Canada. Or les phases d'OA positive ont dominées durant les années 1989-1995, au moment même où les données d'épaisseur de banquise étaient récoltées par les sous-marins américains (voir plus haut). La question qui peut alors se poser est de savoir si l'on peut interpréter ces variations d'épaisseur estimées à partir d'un échantillonnage spatio-temporel restreint et hétérogène négligeant en particulier les zones d'accumulation de l'ouest de l'Arctique, comme une diminution du volume global de la couverture de glace à l'échelle du bassin et sur les dernières décennies. C'est en partie dans le but de répondre à ces incertitudes que le projet DAMOCLES (Developing Arctic Modeling and Observing Capabilities for Long-Term Environmental Studies), porté par l'Union Européenne, est en cours de réalisation.

Si l'on considère que le réchauffement global de la planète, qui est observé depuis le début de l'ère industrielle par les enregistrements de température de l'air, n'a commencé à ébranler l'équilibre de la banquise que ces dernières décennies, on est donc en droit de se demander si le déclin de la banquise aux

hautes latitudes n'est pas l'empreinte d'un emballement du système climatique en Arctique (« Polar amplification » en anglais). Le renforcement de ce déclin depuis le début du 2^{ème} millénaire pose quand à lui la question du possible franchissement par le système *banquise* d'un point de non-retour (« Tipping point » en anglais) [Lindsay et Zhang, 2005], conduisant à une irréversibilité des processus liée à des rétroactions positives sur le déclin de la couverture de glace.



Figure 5a. Photo prise d'avion d'un chenal dans la banquise. *Crédit photo* : F. Dominé.



Figure 5b. Crête de compression de plusieurs mètres d'épaisseur. *Crédit photo* : E. Brossier.

2. Rôle de la banquise Arctique dans le climat

2.1 Variation du flux d'eau "douce" à la surface de l'océan

La glace de mer et l'océan exercent l'un sur l'autre un contrôle mutuel lié entre autres aux variations de la couverture de glace dans les régions polaires. Ces variations pourraient avoir des répercussions sur la circulation océanique globale [McBean *et al.*, 2005]. Les régions subpolaires de l'Atlantique Nord sont des sites de convection où se forme une part importante des eaux denses de l'océan mondial. L'activité convective dépend de la stabilité des eaux (i.e. de leur stratification) qui, dans ces régions, est assurée par la présence d'une couche de surface froide mais non salée. Lors de sa formation, la banquise est constituée d'une combinaison de cristaux de glace d'eau peu salée et de poches d'eau très salée (appelées « *brines* » en anglais). Suivant la vitesse de formation de la glace de mer, qui dépend des conditions de salinité et température de l'eau de mer et de la température de l'air, la spéciation du sel entre la phase solide et la phase liquide sera plus ou moins forte : Une glace qui se formera lentement présentera une teneur en sel élevée, tandis que dans le cas contraire, elle pourra présenter des teneurs en sel très faible, entre 0 et 10 g/L. De plus, au cours du temps, la banquise rejette peu à peu le sel qu'elle contient par migration vers le bas des poches de saumure. Une banquise dite « vieille » peut ainsi atteindre des teneurs en sel parfois proche de 0 g/L. Par rapport à l'océan sous-jacent, la glace de mer peut alors être considérée comme « douce ». De ce fait, un excédent de glace apporté par le détroit de Fram qui vient fondre dans les régions subpolaires, implique une injection d'eau douce dans la couche de surface de l'océan, renforçant ainsi sa stabilité. Ce mécanisme pourrait dès lors affaiblir la convection. Or cette dernière est un maillon essentiel de la circulation thermohaline océanique dont elle alimente la branche profonde qui transporte les eaux denses formées vers l'équateur. De plus, il apparaît de manière presque certaine que la variabilité de la circulation thermohaline influence en retour l'état de la banquise: Dans l'Atlantique, la circulation thermohaline transporte en surface vers le nord des eaux chaudes et salées d'origine tropicale via le Gulf Stream et la dérive nord-atlantique. La pénétration plus importante dans le bassin Arctique de ces eaux peut contribuer au recul de bord de la banquise, autorisant des échanges de chaleur plus intenses entre l'océan et l'atmosphère. A l'inverse, si ces eaux n'atteignent plus l'Arctique, il est raisonnable d'envisager une extension de la banquise vers le sud, un blocage de la convection dans les régions subpolaires et un refroidissement général des latitudes tempérées. L'éventualité d'un tel ralentissement est l'enjeu des débats actuels sur le devenir du climat.

2.2 Rôle d'isolant de la banquise Arctique

Durant l'hiver, la glace de mer est un isolant thermique efficace entre une atmosphère froide, pouvant atteindre quelques dizaines de degrés en dessous de zéro, et un océan relativement chaud dont la température ne peut descendre en deçà de -2°C. Dès que l'épaisseur de la banquise dépasse quelques

dizaines de cm, les échanges d'énergie entre l'océan et l'atmosphère chutent très rapidement. En été en revanche, lorsque la banquise s'amincie, elle laisse pénétrer plus facilement le rayonnement solaire dans l'Océan Arctique. A titre d'exemple, si l'on considère une banquise dont seulement 0.5% de sa surface sont fait de glace très fine et transparente ou d'eau libre, alors 50% des échanges d'énergie entre l'océan et l'atmosphère s'effectueront au niveau de ces 0.5% de la surface [Maykut and Untersteiner, 1971]. Récemment, *Lupkes et al.* [2007] ont montré qu'il existe une relation fortement non linéaire entre la fraction A d'une région couverte à 90% ou plus de glace, et la température de la couche limite atmosphérique sus-jacente. En hiver, pour $A > 90\%$, une baisse de seulement 1% de la fraction de glace implique une hausse jusqu'à 3.5°C de la température de l'atmosphère à la surface de la glace. Le rôle d'isolant de la banquise est donc essentiel et rend capital la compréhension des mécanismes de formation et d'ouverture des fractures et des chenaux (voir Chapitre III).

2.3 La boucle de rétroaction de l'albédo

La présence de la banquise, de part son albédo très élevé (~90%), permet de réfléchir une grande part du rayonnement solaire incident, et donc d'éviter l'absorption de ce dernier par l'océan. La réduction de la couverture de glace va donc faire varier de manière drastique la « couleur » de l'océan. Dans un contexte de réchauffement climatique particulièrement intense en Arctique, des boucles de rétroactions positives, favorisant la fonte de la glace, peuvent se mettre en place (voir figure 6 ci-après). Une diminution de l'épaisseur comme de la concentration de glace fait diminuer l'albédo de l'océan, ce qui entraîne en été une augmentation de l'absorption d'énergie solaire par ce dernier. Ce phénomène favorise la fonte estivale de la banquise, retarde son regel en début d'hiver, entraîne une diminution de son épaisseur, intensifiant du même coup sa fonte. Cette boucle de rétroaction est donc positive vis à vis de la quantité de glace de mer en Arctique, et pourrait donc conduire à l'emballement de son recul. Cette enchainement de processus est souvent citée par la communauté scientifique comme cause probable de l'intensification du réchauffement climatique dans l'Arctique auquel nous faisions allusion en première partie de cette introduction. D'autre part, nous verrons plus loin dans ce mémoire que la diminution de son épaisseur pourrait également amoindrir sa résistance mécanique, facilitant ainsi sa fracturation et sa dérive, et par voie de conséquence la fraction d'eau libre dans le bassin Arctique (voir chapitre I).

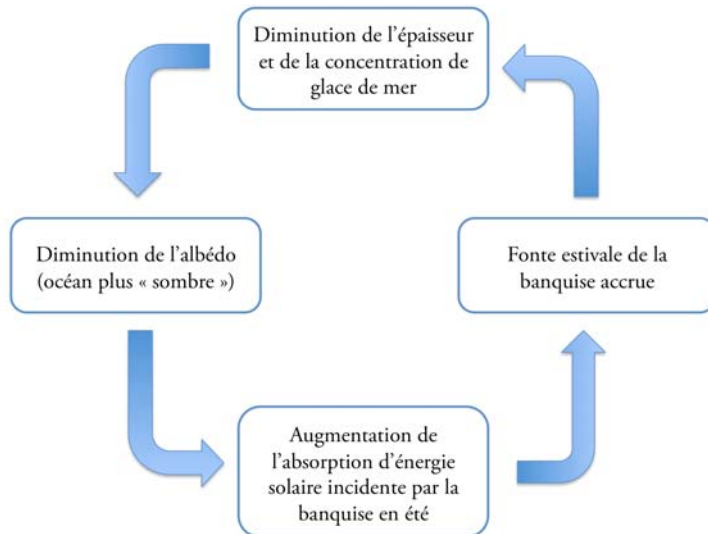


Figure 6. Boucle de rétroaction de l'albédo.

3. La banquise dans les modèles de climat global (MCG)

Au regard du rôle essentiel joué par la banquise dans le climat de la planète, tous les développeurs ont intégré une composante « banquise » à leurs modèles climatiques. Ces modèles sont construits autour d'une superposition de trois couches aux propriétés physiques bien distinctes, et censées représenter l'océan, la banquise, et l'atmosphère. Ils sont dits « couplés » car les trois enveloppes précitées sont en interactions au niveau de leurs surfaces de contact. La difficulté majeure rencontrée par les modélisateurs est d'arriver à modéliser de façon optimale tous les mécanismes d'interaction entre ces trois enveloppes qui se manifestent par des processus de type thermodynamiques et mécaniques. Les processus thermodynamiques sont essentiellement la fonte et le regel qui dépendent des variations de températures de l'air et/ou de l'océan de surface. Les processus mécaniques sont essentiellement la déformation et la fracturation, qui dépendent des forces mécaniques provenant de l'atmosphère et de l'océan, et qui influence fortement la cinématique (vitesse de dérive par exemple) et la dynamique (accélération) de la banquise.

Dans les modèles les plus primitifs, la banquise était considérée comme une couche initialement uniforme et d'épaisseur constante, et dont l'extension spatiale et l'épaisseur n'évoluaient qu'en fonction de processus thermodynamiques. Dès la fin des années 70, un modèle de banquise où les processus thermodynamiques et mécaniques sont couplés, fut proposé par *Hibler* [1979]. A titre d'exemple, la résistance mécanique de la glace dépend dans ce modèle de son épaisseur et de la fraction d'eau libre en son sein, qui elles-mêmes dépendent des conditions de températures de l'atmosphère et de l'océan. Depuis 30 ans, la partie mécanique de la composante « banquise » des MCG n'a conceptuellement que peu évolué.

3.1 La banquise : un fluide visqueux ?

A l'image du schéma de modélisation proposé par *Hibler* [1977], la plupart des modèles de climat utilisés jusqu'à nos jours considèrent la banquise comme un fluide ayant une rhéologie visqueuse-plastique (VP). Plus précisément, la banquise est considérée comme une couche se comportant comme un fluide visqueux newtonien, mais qui peut s'écouler localement de manière plastique lorsque les contraintes en son sein dépassent un seuil de résistance. Ce seuil est communément représenté par une enveloppe de contraintes dans l'espace des contraintes principales, dont la forme proposée initialement par *Hibler* [1977] était elliptique (Figure 7). Ce cadre de modélisation peut apparaître étrange pour un observateur qui regarde une photographie aérienne ou une image satellite de la banquise (voir figure 8 ou encore, *Schulson* [2004]), ou bien une animation sur quelques jours ou quelques heures de son évolution sur une région de quelques mètres à quelques kilomètres. En effet, que ce soit sur l'une ou l'autre de ces

observations et leurs échelles spatio-temporelles associées, l'observateur peut y voir un milieu qui semble très hétérogène et qui se fracture sans cesse.

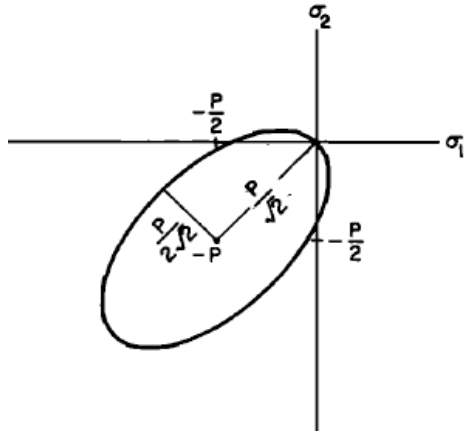


Figure 7. Enveloppe de contrainte représentée dans le plan des contraintes principales. Si l'état de contrainte se situe à l'intérieur de l'ellipse, la banquise se déforme de manière visqueuse. Si l'état de contrainte est sur l'enveloppe elliptique, la banquise se déforme de manière plastique.
Source : Hibler, 1977.

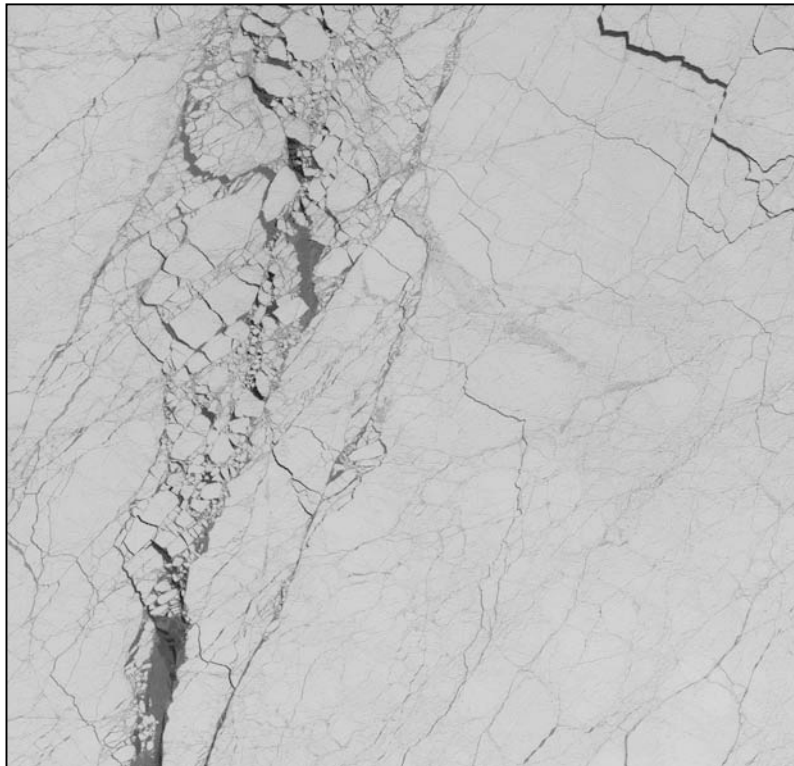


Figure 8. Photographie satellite d'une région de banquise hivernale d'environ 50 km². On peut observer le degré de fracturations très important de la couverture de glace, allant de simples fractures conduisant à l'ouverture de chenaux, jusqu'à de véritables failles ou le mouvement de la glace est purement cisailant. Crédit : spot image

Nous sommes donc ici devant un réel paradoxe, qui consiste à essayer de modéliser un solide elasto-fragile [Weiss *et al.*, 2007] avec une rhéologie visqueuse-plastique. Coon [1974], tout comme un peu plus tard Hibler [1977], avaient conscience de ce paradoxe mais ils firent l'hypothèse qu'aux grandes

échelles de temps (de l'ordre de quelques jours) et d'espace (au delà de 10 km), la banquise se comportait effectivement comme un fluide visqueux et pouvait donc être modéliser comme tel. Nous verrons dans le chapitre III de ce mémoire qu'il n'en est rien. Par la suite, différentes formes d'enveloppes de contraintes furent proposées (voir par exemple *Zhang et Rothrock* [2005]), comme par exemple une courbe elliptique tronquée par des branches de Coulomb permettant à la banquise de se trouver dans un état de contrainte en traction [*Hibler et Schulson*, 2000]. Tout en gardant un concept de modélisation très similaire à celui d'*Hibler* [1979], *Hunk et Dukowicz* [1997] proposèrent une nouvelle rhéologie (Elastico-visqueuse-plastique, ou EVP), afin d'introduire dans les équations d'évolution de la banquise un terme élastique sans réalité physique propre, mais permettant de régler le problème de singularité émergeant lorsque des faibles taux de déformation sont calculés par les modèles.

Le paradoxe existant entre l'observation de nombreuses fractures au sein de la banquise et le cadre de modélisation utilisé par les modèles a été souligné par plusieurs études [*Nye*, 1973 ; *Weiss et al.*, 2007; *Rampal et al.*, 2008; *Girard et al.*, en prép.]. Cependant, ce concept de modélisation ayant l'avantage de permettre un couplage « aisé » entre la banquise et les autres couches fluides comme l'océan et l'atmosphère, il est encore à ce jour largement utilisé, y compris dans les MCG les plus récents. Regardons maintenant dans quelle mesure les modèles actuels de banquise reproduisent les observations, et où se situent leurs limites.

3.2 Evaluation des modèles de banquise

Les modèles actuels parviennent à reproduire raisonnablement bien la circulation grande échelle de la banquise (Figure 9).

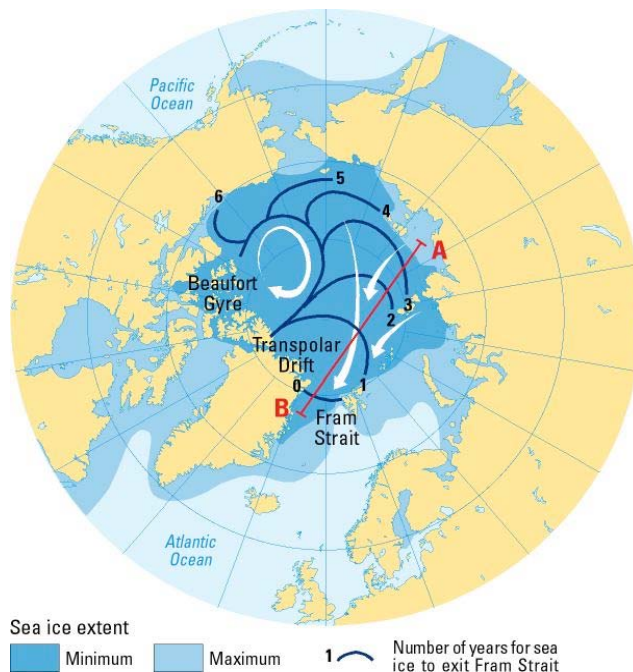


Figure 9. Circulation générale de la banquise Arctique telle qu'on peut l'obtenir en moyennant sur les échelles de temps et d'espace maximales les trajectoires de bouées dérivantes enchaînées dans la couverture de glace. On peut remarquer la présence de deux principales structures : le Gire de Beaufort, et le Courant Transpolaire. *Source:* Pfirman et al., 1997.

Les cartes d'épaisseur de la banquise sont relativement bien corrélées au premier ordre avec les observations récoltées le long de transects effectués par des sous-marins américains dans le bassin Arctique [Rothrock *et al.*, 1999], par exemple en reproduisant correctement les fortes épaisseurs de glace observées au nord du Groenland et de l'archipel canadien [Zhang *et Rothrock*, 2005]. La dérive simulée de la glace est quand à elle comparable avec les champs de dérive obtenus à partir des données satellites SSM/I [Timmermann *et al.*, 2005].

En revanche les champs de déformation sont très mal reproduits [Lindsay *et al.*, 2003 ; Thomas, 1999], et plus particulièrement les zones relativement étroites et quasi linéaire appelés chenaux (dont la longueur peut varier de l'ordre de quelques mètres jusqu'à l'échelle du bassin, i.e. 10^3 km) ou se concentre la déformation de la banquise et qui correspondent, par analogie avec la croûte terrestre, à des failles actives [Weiss *et al.*, 2007]. Les modèles les plus sophistiqués, qui introduisent plusieurs catégories de banquise en fonction de leur épaisseur ainsi qu'une dépendance de la résistance mécanique à la proportion de glace mince [Maslowski *et Lipscomb*, 2003], ou bien encore un mécanisme d'affaiblissement de la couverture de glace en fonction de sa divergence [Hutchings *et al.*, 2005], montrent une localisation plus importante de la déformation, et des champs de déformation en apparence plus réalistes. Cependant, Girard *et al.* (**en prép.**) montrent que d'un point de vue plus quantitatif ces champs de déformation ne sont toujours pas satisfaisants vis à vis des propriétés multi-échelles de la déformation de la banquise déduites à partir de données Lagrangiennes [*International Arctic Buoy Program*] (présentés dans ce manuscrit dans les chapitres 2 & 3), ou bien à partir de données satellitaires RGPS [*Polar Remote Sensing Group*] [Marsan *et al.*, 2004]. Le désaccord entre les résultats des modèles de banquise et les observations constitue l'une des motivations de ce travail de thèse.

4. Les observations de la banquise Arctique

L'intérêt apporté par la communauté scientifique à l'étude de la banquise croît de façon spectaculaire depuis les 30 dernières années dans de nombreux pays. Des observations de qualité et en quantité suffisante ne sont disponibles que depuis la fin des années 70 avec l'avènement, des satellites d'une part, et de programmes internationaux visant principalement à échantillonner l'océan et l'atmosphère arctiques à l'aide de bouées dérivantes enchaînées dans la banquise d'autre part. Le lancement et le suivi des bouées dérivantes dans l'Arctique est du ressort de l'International Arctic Buoy Program (IABP), qui est ensuite chargé de collecter, compiler et distribuer ces données. Grâce à ces dernières, des mesures de paramètres très divers ont été effectuées le long de trajectoires Lagrangiennes: température de l'océan de surface et de l'air dans la couche limite atmosphérique, densité de l'eau de mer ou bien encore de vitesse de vents et de flux turbulents, etc. Ces mesures ont été effectuées avec une bien meilleure résolution temporelle que dans le cas des satellites (jusqu'à 12 minutes pour certaines bouées), et s'étalent sur une période allant de Janvier 1979 à nos jours.



Figure 10. Photo d'une bouée enchaînée dans la banquise faisant partie du programme IABP. *Crédit photo:* D. G. Barton (1992).

Les données satellitaires ont été utilisées pour étudier l'évolution récente de l'étendue de la banquise, profitant d'une couverture spatiale exhaustive et régulière du bassin Arctique (quasiment toute la largeur du bassin, échantillonnée au mieux tous les 10 kilomètres) sur une période de quelques dizaines d'années. Grâce aux données satellitaires toujours, des études sur la cinématique de la banquise (champ

de vitesse et de déformation) ont été réalisées, mais cette fois sur des périodes de temps relativement courtes, de l'ordre de l'année en général. Le jeu de données Lagrangien de l'IABP a, quand a lui, été principalement utilisé pour étudier les processus thermodynamiques mettant en jeu la banquise, l'océan et l'atmosphère. Malgré une couverture du bassin qui, par nature, est plus hétérogène que celle permise par les satellites, ces données ont été également utilisées pour décrire qualitativement et quantitativement la cinématique de la banquise aux grandes échelles (par exemple le champ moyen de dérive) [*Colony et Thorndike, 1984; Thorndike, 1986a*].

C'est le jeu de données Lagrangien de l'IABP (détailée de manière plus exhaustive dans les chapitres de ce mémoire) qui constitue la principale source d'observations pour le travail effectué durant cette thèse. A ce titre, nous pouvons d'ores et déjà indiquer qu'une des originalités de notre travail fut d'étudier la cinématique (dérive et déformation) d'un solide à partir de trajectoires lagrangiennes, en s'inspirant de méthodologies développées pour les fluides (voir chapitres II & III).

5. Objectifs et organisation du mémoire

Dans un contexte où la compréhension et la prévision du réchauffement climatique de la planète est un enjeu majeur, une étude approfondie de la banquise est essentielle au regard de son implication dans la machine climatique et de part l'exceptionnelle pluridisciplinarité à laquelle son étude fait appel.

L'étude de notre objet peut s'entreprendre sous divers angles, à savoir par la modélisation numérique, ou le traitement de données issues d'observations, dans les buts respectifs de modéliser ou de caractériser au mieux les processus dont la banquise est le support. Durant ce travail de thèse, nous nous sommes concentrés sur le traitement et l'analyse multi-échelles (en temps et en espace) de données issues d'observations lagrangiennes (le jeu de donnée de l'IABP), afin de caractériser les processus physiques qui dictent la cinématique de la banquise, à savoir ses vitesses de dérive et de déformation. Pour cela, nous nous sommes inspirés de méthodes d'analyses souvent utilisées pour étudier les fluides turbulents, et en particulier, la diffusion et la dispersion des bouées dérivantes de l'IABP.

De nombreuses interactions mécaniques ayant lieu entre la banquise d'une part, et l'atmosphère et/ou l'océan d'autre part, nous nous sommes forcés d'appréhender les questionnements sur notre objet d'étude de manière globale, c'est à dire en ayant toujours à l'esprit la nature des forçages qui lui sont appliqués. En d'autres termes, nous avons initié notre réflexion par le postula de base suivant : la banquise Arctique est une immense plaque rigide flottant sur l'Océan Arctique, et soumis à un forçage dynamique provenant des deux enveloppes fluides qui l'entourent. Ce postulat témoigne de l'originalité, de la richesse, mais aussi de la complexité de notre étude.

En effet, elle consiste à s'intéresser aux propriétés de diffusion et de dispersion d'un solide, c'est à dire des processus caractéristiques des fluides, tout en ayant à l'esprit qu'elles sont le résultat probable d'une combinaison de processus physiques propres à la mécanique du solide (déformation et fracturation) d'une part, et d'un forçage dynamique provenant de fluides turbulents qui l'entourent d'autre part. De plus, d'un point de vue purement mécanique, il est difficile de ne pas être tenter de faire une analogie entre le comportement de la banquise et celle de la croûte terrestre, en différentiant bien sur la nature de leurs forçages respectifs et surtout, les échelles de temps sur lesquelles ces forçages ont lieu. En étudiant la banquise sous l'angle choisi pour ce travail de thèse, nous nous situons donc toujours à la frontière de la mécanique du solide et de la mécanique des fluides.

D'un point de vue moins fondamental, mais tout aussi important, nous pouvons également supposer que la compréhension incomplète des processus physiques qui opèrent dans le système « banquise élargi » est sans doute à l'origine de certaines incertitudes qui règnent quand à son devenir (voir section 3 du chapitre d'introduction).

Les objectifs de ce travail de thèse vont donc être de double nature. D'une part, proposer à notre communauté scientifique un panel des processus physiques qui s'opèrent s'opère au sein de la banquise Arctique et établir leurs caractéristiques fondamentales, dans le but de pouvoir les prendre en compte dans les développements de modèles futurs. D'autre part, montrer que la banquise peut être considéré comme un objet géophysique modèle pouvant servir de support à de nombreuses communautés de la géophysique, voire de la physique.

Ce mémoire de thèse s'articulera de la manière suivante :

- (i) préciser le rôle que peuvent jouer les propriétés intrinsèques du matériau glace, à savoir son comportement fragile vis à vis des efforts qui lui sont appliqués, sur le déclin spectaculaire observé ces dernières décennies (Chapitre I)
- (ii) caractériser les propriétés de diffusion (i.e. des vitesses de dérive) de la banquise et tenter de mieux comprendre les mécanismes qui en sont à l'origine (Chapitre II)
- (iii) caractériser les propriétés de dispersion (qui peut être reliée au taux de déformation) des bouées dérivantes de l'IABP, discuter des mécanismes sous-jacents qui en sont les causes et de leurs implications en terme de rhéologie de la banquise (Chapitre III)

Un dernier chapitre sera consacré à la discussion des résultats obtenus ainsi qu'aux perspectives qu'ils ouvrent en terme (i) de pistes d'amélioration des modèles de banquise actuels, (ii) d'explication du processus qui peut être à l'origine de la cinématique de la banquise telle que nous l'aurons caractérisé dans les chapitres précédents (Chapitre IV).

Chapitre I :

Evolution récente de la vitesse de dérive et du taux de déformation de la banquise Arctique

D'après:

Rampal, P., J. Weiss and D. Marsan (2008) Positive trend in the mean speed and deformation rate of Arctic sea ice, 1979-2007, **accepted** by *Journal of Geophysical Research-Ocean*.

Abstract :

Using buoy data from the International Arctic buoy Program, we found that the sea ice mean speed has substantially increased over the last 29 years (+17% per decade for winter; +8.5% for summer). A strong seasonal dependence of the mean speed is also revealed, with a maximum in October and a minimum in April. The sea ice mean strain rate also increased significantly over the period (+51% per decade for winter; +52% for summer). We check that these increases in both sea ice mean speed and deformation rate are unlikely a consequence of a stronger atmospheric forcing. Instead, they suggest that sea ice kinematics plays a fundamental role in the albedo feedback loop and sea ice decline: increasing deformation means stronger fracturing, hence more lead opening and therefore a decreasing albedo. This accelerates sea ice thinning in summer and delays refreezing in early winter, therefore decreasing the mechanical strength of the cover and allowing even more fracturing and larger drifting speed and deformation, and possibly a faster export of sea ice through the Fram Strait. The September minimum sea ice extent of 2007 might be a good illustration of this interplay between sea ice deformation and sea ice shrinking, as we found that for both winter 2007 and summer 2007, exceptionally large deformation rates affected the Arctic sea ice cover.

1. Introduction

The Arctic sea ice cover can be considered as a thin plate stressed mainly under the action of winds and ocean currents [*Thorndike and Colony*, 1982]. This leads to the fracturing and faulting of the sea ice cover, which accommodate most of its deformation [*Schulson*, 2004; *Weiss et al.*, 2007]. This process, along with thermodynamics, controls the amount of open water, the ice thickness distribution, and indirectly the drifting properties of the sea ice cover. Consequently, sea ice kinematics is important for understanding the momentum, mass, and energy balance in the Arctic and more generally its influence on the Earth's climate [*Moritz et al.*, 2002]. For example, an increase of the drifting speed would suggest a larger amount of perennial sea ice exported through Fram Strait [*Zhang et al.*, 2000; *Kwok and Rothrock*, 1999], then a relative increase of first year sea ice in the basin, and consequently a thinning of the sea ice cover. Excepting the Fram, Banks and Nares straits, and the Barents Sea, the Arctic sea ice cover is essentially enclosed in a confined basin. Therefore, an increase of the mean drifting speed would suggest an increase of the strain-rate, i.e. a stronger fracturing/faulting. This implies more lead opening, as well as an higher variability of the ice thickness, causing a decrease in the albedo and allowing more shortwave absorption by the ocean, thereby shrinking the cover during summer, reducing its strength, and increasing again the fracturing and faulting [*Zhang et al.*, 2000; *Moritz et al.*, 2002; *Kwok*, 2006]. Fracturing during winter enhances the thermodynamically driven production of new ice and consequently modifies the heat and salinity budget in the Arctic Ocean [*Maykut*, 1982; *Alam and Curry*, 1997; *Lupkes et al.*, 2007]. These complex processes are highly non-linear and need to be investigated in more details to understand their role in the Arctic sea ice decline and more generally on climate change. Thirty years ago, the Arctic sea ice cover extended during winter over about 14 million km² in winter and 7 million km² in summer. There is now consensus towards a significant shrinking during the last decades, both in terms of spatial extension and average thickness [*Lemke et al.*, 2007], supposedly mainly under the action of thermodynamic processes, although recent works suggested that the flushing of thick, multi-year ice out through Fram Strait could be a significant cause of sea ice mass loss [*Lindsay and Zhang*, 2005]. A spectacular illustration was recently given during the 2007 melt season, as the perennial sea ice further plummeted to the lowest levels since satellite measurements began in 1979. The average sea ice extent for September 2007 was 4.28 million km², the lowest on record, shattering the previous record, set in 2005, by 23%. September 2007 sea ice was 39% below the long-term average from 1979 to 2000. The September rate of sea ice decline since 1979 is now approximately 10% per

decade, or 72000 km² per year, a rate systematically underestimated by climate models [Stroeve *et al.*, 2007; Serreze *et al.*, 2007].

On the other hand, the 2007 IPCC report [Lemke *et al.*, 2007] concluded that “*There is no indication of long-term trend*” in either ice motion, or ice export out of the Arctic basin. The results reported here reveal a different picture. As a revealing example, the drifting speed underwent in 2006-2007 by the polar schooner Tara was twice as large as the mean drifting speed of the Fram ship 115 years ago [Gascard *et al.*, 2008]. Tara drifted along the transpolar drift and reached the open ocean through Fram strait in late January 2008, i.e. one year earlier than expected by scientists. This motivates a statistical study of the Arctic sea ice drifting speed and deformation rate evolutions over the last decades to evaluate a possible role of dynamic processes [Zhang *et al.*, 2000] to reduce sea ice extent and thickness and accelerate its decline as observed in recent years.

Our paper is organized as follow: First, we study the time evolution of the mean speed of the drifting buoys issued from the International Arctic Buoy Program (IABP) dataset (detailed in section 2) from 1979 to 2007 (section 3). Then, we check that the linear trends obtained are statistically representative of a similar evolution of the whole Arctic sea ice motion (section 4). Secondly we study the time evolution of the sea ice cover deformation rates over the same period (section 5). Possible causes for the observed trends are then discussed in section 6.

2. Dataset

We use the IABP dataset that consists, from December 1978 to December 2001, of 3-hourly buoy positions, and from January 2002 to December 2007, of 12-hourly positions. These buoys are fixed on the ice and drift according to the ice motion. Buoy tracking was obtained from GPS receivers or Argos transmitters with a position uncertainty of the order of 100 m and 300 m, respectively [Thorndike and Colony, 1982; Heil *et al.*, 2002]. Figure I-1 shows all the buoys tracks and the delimited regions noted “Central Arctic”, “Coasts” and “Fram” (see below for more details).

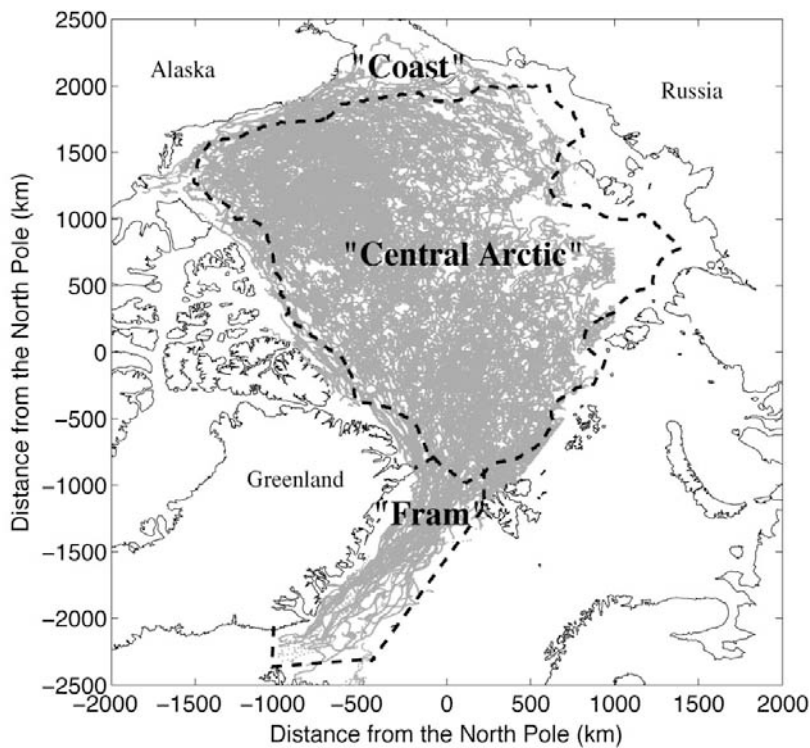


Figure I-1. Map of the Arctic basin showing the buoys trajectories of the IABP dataset, combining the 3-hourly dataset of 1979-2001 and the 12-hourly dataset of 2002-2007. The tracks have been recorded between January 1979 and December 2007. Only the Laptev Sea is poorly covered by this dataset.

The reference coordinate system used in this study is a Cartesian coordinate system centered on the North Pole with the y-axis following the Greenwich meridian. Each latitude-longitude buoy position is defined in the orthogonal base $(\mathbf{e}_1, \mathbf{e}_2)$ of this coordinate system as $\mathbf{x}_{(lat,lon)} = x\mathbf{e}_1 + y\mathbf{e}_2$ using a polar stereographic projection. In order to analyze a homogeneous dataset, we work on 12-hour displacements: For any given buoy position (x,y) , we compute the speeds

$u_x(\tilde{x}, \tilde{t}) = (x(t+12h) - x(t))/12h$ (along the x-axis) and $u_y(\tilde{y}, \tilde{t}) = (y(t+12h) - y(t))/12h$ (along the y-axis) at all available times t , i.e., such that these exist recorded positions both at times t and $t+12h$. Here, \tilde{x} , \tilde{y} , and \tilde{t} are defined as the means $\tilde{x} = (x(t+12h) + x(t))/2$, $\tilde{y} = (y(t+12h) + y(t))/2$ and $\tilde{t} = ((t+12h) + t)/2$. Given an error on position ranging between 100m and 300m, the uncertainty on the 12-hour speeds ranges from 0.3 to 1.0 cm/s. The statistics on speed are sensitive to the scale over which the speed is computed, here set to 12 hours. However, the Lagrangian correlation time for sea ice diffusion is typically of the order of a few days (5 days according to *Colony and Thorndike* [1984]; see also *Thorndike* [1986a, figure 6]). For all time scales below this Lagrangian time, a Lagrangian speed can be defined unambiguously [*Taylor*, 1921]. Table I-1 recapitulates the number of buoys, and the number of speed values per year, distinguishing winter from summer. For each season, the number of trajectories that were used in our analysis is also given. Figure I-2 displays the probability density function (pdf) of the speed u defined as $u = (u_x^2 + u_y^2)^{(1/2)}$, for the entire dataset.

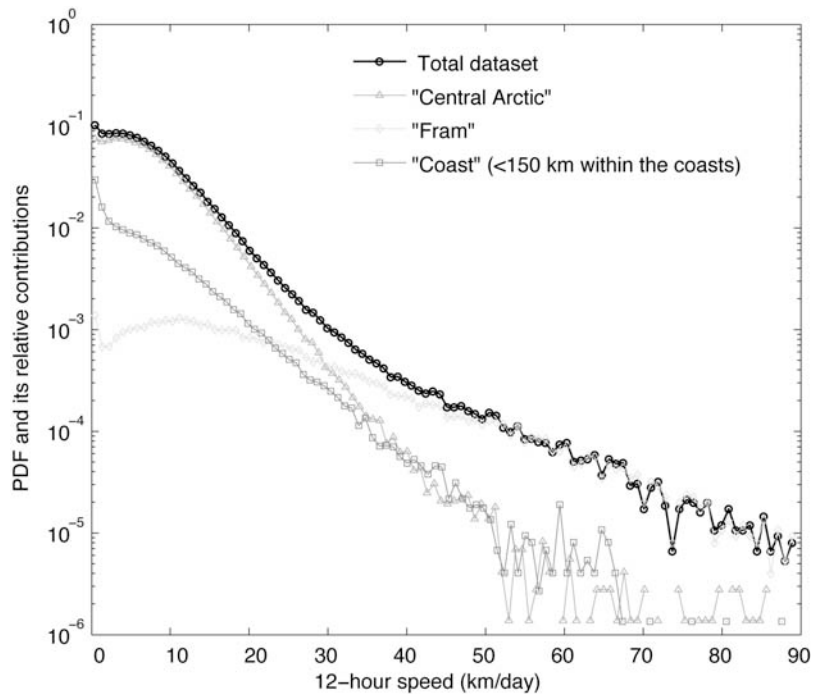


Figure I-2. Probability density function of the 12-hour speeds computed from the total IABP dataset, and its contributions coming from the “Central Arctic”, the “Fram” and the “Coast” regions.

The contribution of the Fram Strait (noted as “Fram” on the map of figure I-1), which is characterized by a strong southward advection of sea ice, is singled out. Almost all the speed values

stronger than 50 km/day are recorded in the Fram Strait. Similarly, we single out the contribution of the buoy positions that lie within 150 km of a coast (noted as “Coast” on the map of figure 1). These speeds are on average less than those of the central Arctic (the “Central Arctic” zone of the map of figure I-1). We therefore decided to perform our analysis only on the Central Arctic dataset. By doing so, we avoid biasing our statistics by the low speed values of fast-ice. The Fram Strait region is also of particular interest, but the amount of data from the IABP dataset does not allow us to perform an analysis with significant results for this region. In order to study this zone, we used the satellite derived velocity estimates provided by the Jet Propulsion Laboratory [*Polar remote sensing group*] (see section 5).

Year	# buoys	# tracks	# speed values	
			Total	Seasonal
1979	11	winter: 10 summer: 10	12595	winter: 5876 summer: 6719
1980	24	23 15	15346	6403 8943
1981	24	16 18	13736	5147 8589
1982	19	15 12	13846	7256 6590
1983	17	12 9	9146	4926 4220
1984	11	6 8	9962	6994 2968
1985	17	10 15	12056	6835 5221
1986	25	18 19	23885	13648 10237
1987	34	18 29	28141	15570 12571
1988	35	23 29	27659	13018 14641
1989	22	21 10	15398	10320 5078
1990	19	18 16	13673	7988 5685
1991	32	24 26	27060	15404 11656
1992	37	32 27	31283	16140 15143
1993	35	27 25	30791	20996 9795
1994	21	16 13	21748	15477 6271
1995	10	10 2	9461	9092 369
1996	11	11 9	15769	11040 4729
1997	10	10 6	10756	7115 3641
1998	14	13 6	13725	11409 2316
1999	8	7 5	5936	3378 2558
2000	12	11 7	7664	4851 2813
2001	35	28 31	34030	21224 12806
2002	49	46 35	14074	10308 3766
2003	54	39 38	9315	5651 3664
2004	52	40 37	10771	6347 4424
2005	50	35 35	7422	4078 3344
2006	53	30 47	10303	5821 4482
2007	114	83 101	24240	12468 11772

Table I-1. IABP buoys dataset

3. Analysis of the time variation of buoy speed

3.1 Monthly averages of buoy speed

We here analyze whether the mean speed of the IABP buoys has changed over the last 3 decades. We will study in section 4 how these changes in buoy speed can potentially reflect underlying speed changes of sea ice, by examining spatial and temporal sampling issues inherent to buoy measurements. The mean speed, denoted \bar{u} , is here defined as the speed averaged over a calendar month by

$$\bar{u}_{month} = (1/N_{month}) \sum_{t \in month} u(t) \quad (I-1)$$

where N_{month} is the number of speed values for the month under study. We chose this monthly time scale because it is short enough to document intra-annual variations, as well as long enough to contain enough speed values for a statistically significant estimate of the mean. Because there exist time and spatial correlations in the velocity field [Thorndike, 1986] (Rampal *et al.*, **in prep.**, 2008), the uncertainty on the estimate of the monthly speed \bar{u} cannot be obtained directly from the central limit theorem and the number N_{month} of samples in the distribution, as those N_{month} samples are not independent of each other. Instead, we estimate these errors using a bootstrap method. In order to empirically find how the error $\Delta\bar{u}/\bar{u}$ depends on N_{month} , we consider separately each month and we randomly picked q times ($q \geq 10$) n speed values (n ranging from 5 to 150) for this month, taking care not to pick the same value twice, with the condition that $q \times n \approx 0.75N_{month}$ (i.e. we overall pick about 75% of the set). For a given n , we therefore obtain q distributions of speed values for which we calculate their means. The standard deviation $\Delta\bar{u}$ on the \bar{u} -values is then computed. Figure I-3a displays the results for a particular month, i.e. September 1987. Doing so for all the months between January 1979 and December 2007, we obtain that $\Delta\bar{u}$ decreases with n as follows:

$$\Delta\bar{u}_{bootstrap} = \frac{A \times \bar{u}_{bootstrap}}{n^\lambda} \quad (I-2)$$

where $\bar{u}_{bootstrap}$ is the value of the mean found for a particular distribution (see figure I-3b). The exponent λ is approximately equal to 0.3, and A is equal to 0.6. In our analysis we use relation (I-2), replacing n by N_{month} , to estimate the uncertainty of \bar{u} . We note that relation (I-2) differs

from the error estimate given by the central limit theorem for which $A = 1$ and $\lambda = 0.5$: the actual error is thus larger than the one given by the central limit theorem (as long as $n \geq 13$, as expected in the presence of correlations).

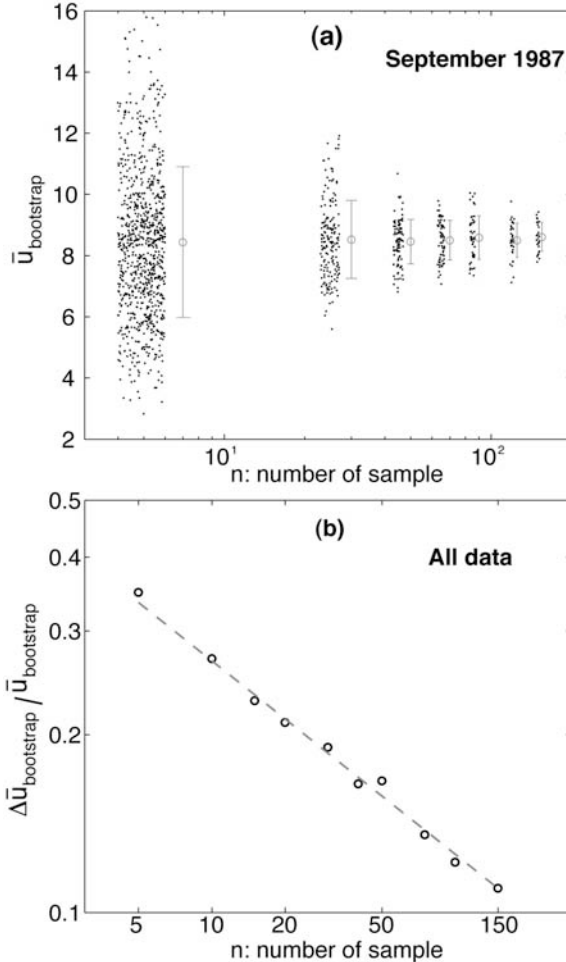


Figure I-3. (a) Estimation of the monthly mean speed uncertainty using a bootstrap method, for the month of September 1987. A number q of random sets of n values are picked, and theirs associated means $\bar{u}_{\text{bootstrap}}$ are computed (black dots). For clarity, we drew each dot at abscise x defined as $x = n + \rho$ where ρ is a random value between -2 and 2. The dispersion $\Delta\bar{u}_{\text{bootstrap}}$ (standard deviation) of the q means $\bar{u}_{\text{bootstrap}}$ is computed, and shown as vertical bars. (b) Dependence of $\Delta\bar{u}_{\text{bootstrap}} / \bar{u}_{\text{bootstrap}}$ on the number of samples n . A general trend $\Delta\bar{u}_{\text{bootstrap}} = A \times \bar{u}_{\text{bootstrap}} n^{-\lambda}$ is obtained, with $A = 0.6$ and $\lambda = 0.3$ obtained by least mean squares.

Figure I-4 shows the monthly mean speed between January 1979 and December 2007 for the Central Arctic dataset. A Fourier transform of the signal reveals a peak at the twelve-month period and thus a strong annual cycle (see inset plot of figure I-4). The maximum mean speed always occurs around October whereas the minimum occurs around April. Thus, this strong seasonal variability is out of phase, lagging by about 6 months, with respect to the sea ice extent seasonal variability. This plot also shows the 12-month running mean. A linear fit to the data (in the least-squares sense, weighted by the error bars) gives an increasing trend with a slope of $5.6 (\pm 1.1) \times 10^{-2}$ km/day per year. The error on the slope is estimated by a chi-2 test.

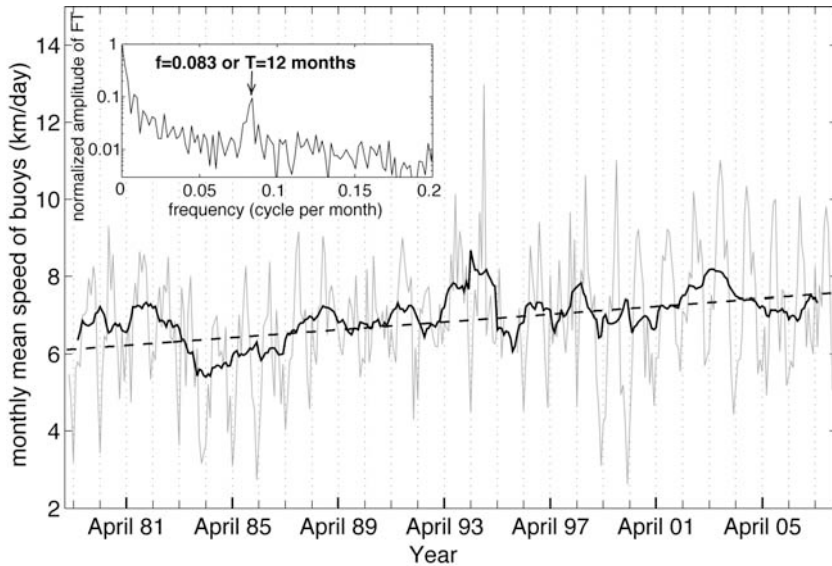


Figure I-4. Monthly mean speed for IABP buoys from January 1979 to December 2007. The monthly means are computed from the 12-hourly speeds dataset and plotted as the light grey line. The 12-month running mean of the signal is plotted as the bold dark line. The least squared fit (weighted by the uncertainty) of the data is plotted as the dashed dark line and gives a slope of $5.6 (\pm 1.1) \times 10^2$ km/day per year. The error on the slope is estimated from a chi-2 test. The inset graph shows the Fourier Transform of the monthly signal with a peak at $T=12$ months.

3.2 Seasonal averages of buoy speed

We calculate the mean speed for winter and summer seasons separately (Figure I-5). Winter and summer means are computed between the 1st of December and the 15th of May of the following year, and between the 15th of June and the 30th of September, respectively. The error bars are computed using equation (I-2), which is likely to over-estimate the uncertainty at the seasonal scale. Linear fits computed by least squares using the errors as weights give significant positive trends of $6.4 (\pm 1.7) \times 10^{-2}$ km/day per year (i.e. 17% ($\pm 5.7\%$) increase per decade) for winter and $5.1 (\pm 1.2) \times 10^{-2}$ km/day per year (i.e. 8.5% ($\pm 2\%$) increase per decade) for summer.

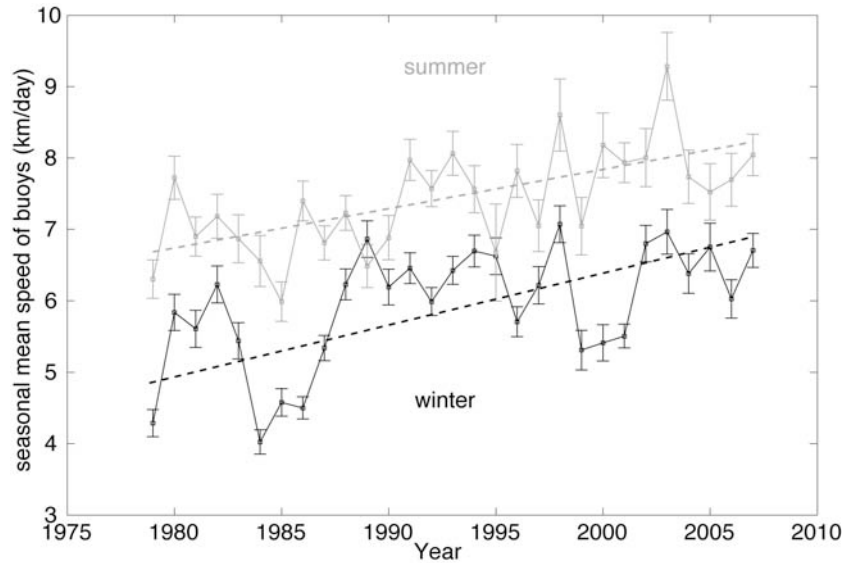


Figure I-5. Buoy mean speed for the winters and summers of 1979-2007. Winter means are plotted in black and summer means in grey. The error bars are estimated following equation (I-1). The weighted linear fits of the data are plotted as dashed lines for winter and summer. The trends are $6.4 (\pm 1.7) \times 10^{-2}$ km/day per year (i.e. 17% increase per decade) for winter and $5.1 (\pm 1.2) \times 10^{-2}$ km/day per year (i.e. 8.5% increase per decade) for summer.

4. Are the mean IABP buoy speeds representative of the mean Arctic sea ice speeds?

So far, we have analyzed the IABP buoy speeds, showing there exists a significant increase of the monthly and seasonal means over the last 29 years. The question arises as to whether this increase is a direct signature of a similar increase of the overall Arctic sea ice speed, i.e., averaged over the whole sea ice extent. This leads us to examine spatial and temporal sampling issues, since the IABP buoy trajectories do not equally sample the Arctic.

We formulate the following null hypothesis: The Arctic sea ice motion is characterized by a monthly averaged speed that is annually constant. In other words, the monthly averaged speed for a given calendar month, e.g. January 2000, is drawn from a distribution that is the same for all the months of January between 1979 and 2007. We thus allow for a seasonal, i.e. intra-annual, variability, but hypothesizes that there is no inter-annual changes (12-month periodic stationary). The question is then to check whether the observed increase of buoy speeds over the 29 years (see section 3) could be due solely to a change in spatial sampling from one year to the other, i.e., if IABP buoys tend to sample fast-moving regions more often in the later years compared to early years. To address this, we will construct a mean speed field over the whole Arctic for each month (hence 12 velocity fields) (see subsection 3.1). Then, we estimate what would have been the buoy monthly mean speeds, as sampled by the actual IABP trajectories, if the underlying speed fields were indeed stationary and we conclude (see subsection 3.2).

4.1 Constructing the mean speed fields

For each of the 12 months, January-December, we generate a mean speed field from the IABP dataset, say that we do not consider the mean drifting directions. Namely, we compute the 12-hour interpolated speed \bar{u} at all positions \mathbf{x}_N reached by buoys and for any given month as:

$$\bar{u}(\mathbf{x}_N) = \frac{1}{\sum_i w_i(\mathbf{x}_i)} \sum_i w_i(\mathbf{x}_i) u_i(\mathbf{x}_i) \quad (\text{I-3})$$

where the summation is performed over all the buoy positions \mathbf{x}_i selected in the following way: the positions \mathbf{x}_i are recorded during the same given month (e.g. all the buoys positions recorded for all the 29 months of January), and contained in the disk centered on \mathbf{x}_N with a radius of $L=200$ km (if the given month is a winter's month) or $L=100$ km (if it is a summer's month) (*Rampal et al., in prep.*, 2008). We define the weight $w_i(\mathbf{x}_i)$ as:

$$w_i(\mathbf{x}_i) = e^{-r^2/2l^2} f(r) \quad (\text{I-4})$$

where $r = \|\mathbf{x} - \mathbf{x}_i\|$, l is the smoothing length defined as $l=L$, and $f(r)$ is a correction term that accounts for the spatial heterogeneity of buoys positions. Ideally, the sample positions \mathbf{x}_i would equally cover the L -radius disk; this is unfortunately not the case, as they follow buoy trajectories. Instead of following a $N(<r) \sim r^2$ law, the number of pairs of distances $\|\mathbf{x}_i - \mathbf{x}_j\| < r$ in general grows initially slower with r , and therefore do not equally sample the disk. Not correcting for this effect would imply having effective resolution lengths varying with \mathbf{x} , that would generally be less than l . We therefore homogenize the smoothing by introducing the correction $f(r) = r^2 / N(\|\mathbf{x} - \mathbf{x}_i\| < r)$. Note that $f(r)$ is defined up to a multiplicative constant, which disappears with the normalization in equation (I-3). To illustrate this correction, we show on figure I-6a (left) an example of the spatial heterogeneity of the velocity measurements around the position of buoy #66739 on the 13th of January 2007, by plotting all the 4630 buoy positions within 400 km for all the months of January between 1979 and 2007. This has to be compared to an equivalent of 4630 positions synthetically computed following a Poissonian repartition (Figure I-6a, right).

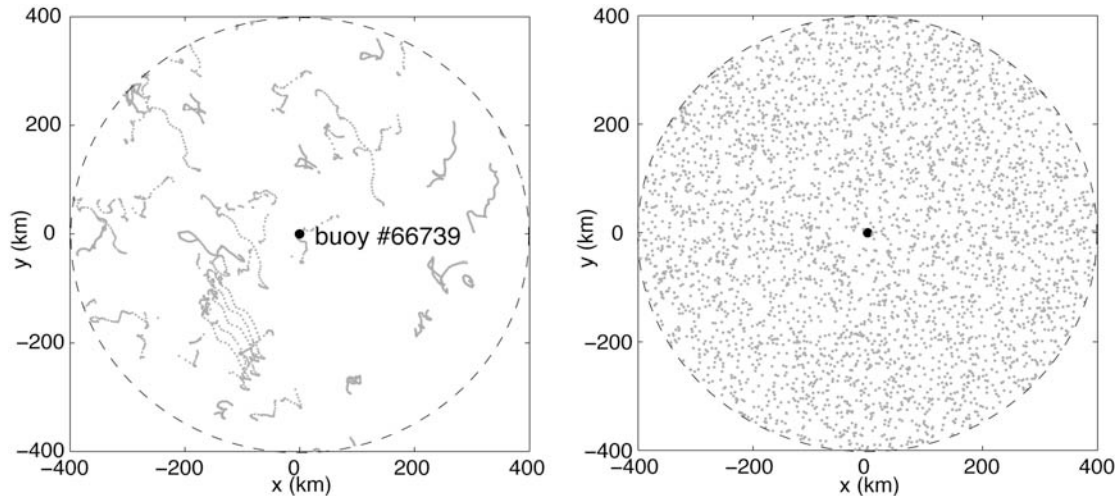


Figure I-6a. Illustration of the spatial heterogeneity of the buoy positions available during any calendar month of January between 1979 and 2007. Here, the position of the buoy #66739 recorded on the 13th of January 2007 is set as the reference position. We plot the 4630 buoy positions found in the January months of 1979-2007 within 400 km of the reference position (left). This can be compared to a set of 4630 synthetic positions computed following a Poissonian repartition (right).

Figure I-6b displays the corresponding number $N(\|\mathbf{x} - \mathbf{x}_i\| < r)$ of distances to the reference point function of r , for the two previous cases, showing clearly the effect of the spatial heterogeneity of the data.

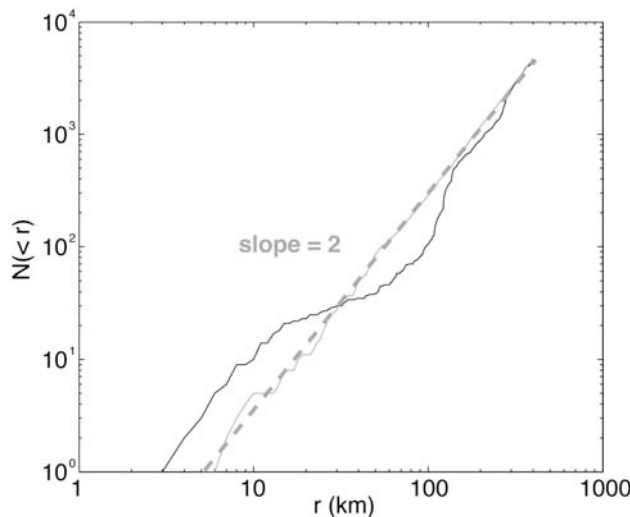


Figure I-6b. Number $N(< r)$ of positions contained in the disk of radius r centered on $(0,0)$ for actual buoy positions (dark line) and synthetic positions (grey line). $N(< r)$ follows a r^2 law (grey dashed line) for the Poisson distribution. For IABP buoys, $N(< r)$ deviates from this law. The term $f(r)$ in equation (I-4) is introduced to correct for this effect.

4.2 Monthly mean speeds estimated from the interpolated speed fields

Using the interpolated speed fields, we compute the monthly means \bar{u}_\circ obtained when sampling these fields with the actual IABP buoy positions of that month. Figure I-7 shows the monthly mean speed time series obtained under our null hypothesis, compared to the actual monthly means of figure I-4. The 12-month cycle is still present in the signal. On the other hand, a linear fit to the data (in the least squares sense) weighted by errors as computed following equation (I-2), gives a quasi-null trend of $6.8 (\pm 3.2) \times 10^{-5}$ km/day per year, i.e. only 0.1% of the actual trend directly estimated from the IABP buoy speeds.

Similarly, the seasonal mean speed signals computed under our null hypothesis give trends of $6.6 (\pm 3.1) \times 10^{-5}$ and $6.9 (\pm 2.7) \times 10^{-2}$ km/day per year, for winter and summer respectively, i.e. 0.1% and 0.14% of the actual trends estimated from the IABP buoy's speeds.

We therefore conclude that the bias introduced by the spatial sampling of the buoys trajectories cannot explain the observed increase of buoy speeds over the 29 years, and consequently that the observed acceleration of buoy motion is significant and representative of an overall acceleration of the sea ice motion over the Arctic basin.

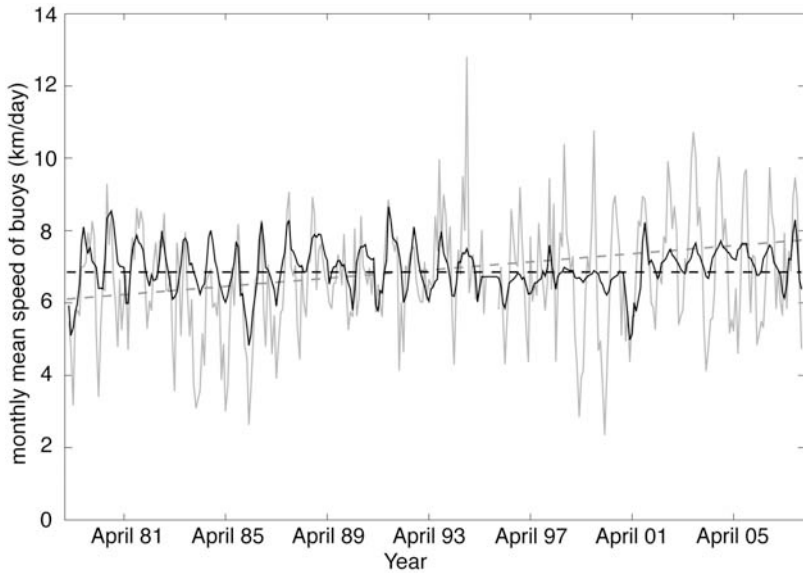


Figure I-7. Monthly mean speed time series $\bar{u}(t)$ (grey line) and $\bar{u}_\circ(t)$ (black line), obtained for the actual IABP buoys and for the IABP buoys under our null hypothesis, respectively. The dark dashed line is the linear fit of $\bar{u}_\circ(t)$ (weighted by the error bars). This later gives a quasi-null trend of $6.8 (\pm 3.2) \times 10^{-5}$ km/day per year, i.e. only 0.1% of the actual trend computed for $\bar{u}(t)$ (dashed grey line).

5. Increase of the mean deformation rate of the sea ice cover over the last 29 years

Excepting the Fram Strait and the Barents Sea, one can consider the Arctic sea ice cover as moving in a confined basin, with velocities vanishing to zero as one get closer to the coasts. Consequently, given the strong increase of the sea ice mean speed during the last three decades, we expect an acceleration of sea ice mean deformation rate (see subsection 4.1). As a first order approximation, we consider that the relative increase of sea ice speed is the same everywhere in the Arctic basin. Then, considering (i) sea ice drifting speed $u=0$ at the coasts and maximum in the centre of the basin, i.e. at about $L=1000$ km from the coasts, and (ii) that velocity gradients and strain-rate tensor are linearly linked as $\dot{\epsilon} = (\nabla \mathbf{u} + \nabla \mathbf{u}^T)/2$, i.e. the norm of the strain-rate tensor $\dot{\epsilon}$ equals $\|\nabla \mathbf{u}\|$ one can estimate the averaged rate of increase of the strain-rate as follows:

$$\frac{\overline{\Delta \|\dot{\epsilon}\|}}{\Delta t} = \frac{\overline{\Delta \|\nabla \mathbf{u}\|}}{\Delta t} = \frac{1}{L} \frac{\overline{\Delta u}}{\Delta t} \quad (I-5)$$

Using equation (I-5) and the rates of increase of sea ice drifting speed determined in section I-3 (6.4×10^{-2} km/day per year for winter and 5.1×10^{-2} km/day per year for summer), we obtain that the deformation rates would have increased by 6.4×10^{-5} day $^{-1}$ per year for winter and 5.1×10^{-5} day $^{-1}$ per year for summer.

In what follows, we check (i) whether the positive trends in sea ice drifting speed found for winter and summer indeed imply positive trends in sea ice deformation rate for both seasons, and (ii) to what extent our first order estimates of these trends are correct. To do so, we estimate the sea ice strain-rate for the period 1979-2007 from the dispersion of pairs of buoys. We present in subsection 4.1 a methodology that allows relating dispersion and deformation. The results of our analysis are given in subsection 4.2, and discussed in section 5.

5.1 Relation between dispersion of buoys and sea ice deformation

The dispersion of pairs of buoys can be linked to sea ice cover deformation [Rampal *et al.*, 2008] using an approach based on the methodology developed by Richardson for turbulent flows [Richardson and Stommel, 1949; Martin and Thorndike, 1985]. We study how the dispersion of pairs of buoys depends on both (i) their initial separation L , and (ii) the time τ during which they disperse. In Figure I-8, two buoys numbered 1 and 2 with absolute positions \mathbf{x}_1 and \mathbf{x}_2 , respectively, and with separation $\mathbf{y} = \mathbf{x}_2 - \mathbf{x}_1$, are considered. If these two buoys initially separated by $L = \|\mathbf{y}(0)\|$ are observed after a time τ , a change in separation is observed. Our notations are: $\mathbf{y}(0)$ has magnitude L and $\mathbf{y}(\tau)$ has magnitude $l(\tau)$. We define the change in separation Δr as $\Delta r(\tau) = \|\mathbf{y}(\tau)\| - \|\mathbf{y}(0)\| = l(\tau) - L$.

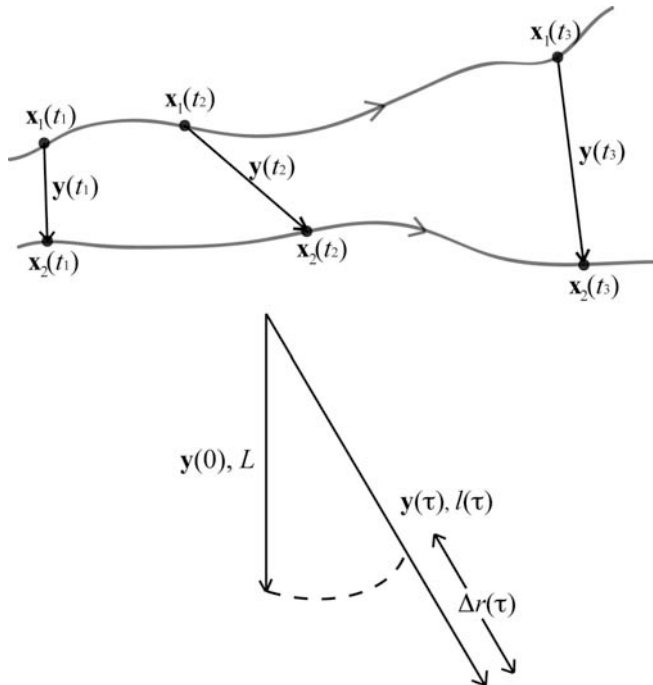


Figure I-8. For a pair of buoys located at $\mathbf{x}_1, \mathbf{x}_2$, and separated by $\mathbf{y} = \mathbf{x}_2 - \mathbf{x}_1$, the change in separation at time τ is denoted $\Delta r(\tau) = \|\mathbf{y}(\tau)\| - \|\mathbf{y}(0)\|$.

In fluid mechanics, the dispersion process is characterized by the mean square change in separation $\langle \Delta r^2 \rangle$. From a solid mechanics perspective, it appears more pertinent to consider the rate $\dot{D} = \Delta r / L\tau$ instead of the change in separation Δr . \dot{D} is analogous to a deformation rate, measured in day⁻¹. Neither Δr nor \dot{D} are sensitive to solid rotations. They only quantify the

deformation due to divergence, convergence, and/or shear. However, this methodology does not allow distinguishing divergence/convergence from shear, as at least triplets of buoys should be used to compute the full strain tensor. When analyzing the whole Arctic basin, we made a distinction between winter (from the beginning of December to mid-May) and summer (from mid-June to the end of September). Separately for both seasons, and for each year of the period, we computed the distributions of \dot{D} . *Rampal et al.* [2008] studied how \dot{D} depends on the scales L and τ . In order to examine how the deformation changed in 29 years, and to minimize sampling issues due to this scale dependence, we considered the statistics of \dot{D} for L between 50 and 500 km and τ between 3 hours and 1 day, hence only a decade in scale range. For each year, the associated distributions for winter and summer are characterized by their standard deviation $\sigma_{\dot{D}}$. In this way, we measure how a cluster of passive tracers of initial size L typically disperses after a time τ or, in other words, how the associated region containing these tracers deforms. The choice of the standard deviation of \dot{D} rather than its mean is partly motivated by the fact that in the limit of small deformation rates (i.e. for large time and spatial scales), only the standard deviation allows to characterize the deformation process. In the work of *Rampal et al.* [2008], we showed that $\sigma_{\dot{D}}$, i.e. the standard deviation of $D = \Delta r/L$, is correlated to the total deformation ε_{tot} . For two particular cases, namely the SHEBA and SIMI experiments, we calculated the strain tensor and the total deformation ε_{tot} from multiplets of buoys. We found that our strain proxy $\sigma_{\dot{D}}$ is proportional to ε_{tot} with a factor of about 4. We concluded that the total strain-rate $\sigma_{\dot{D}}$ can be viewed as a good proxy of the total deformation rate $\dot{\varepsilon}_{tot}$.

5.2 Results

Figure I-9 shows that, despite large uncertainties on the estimates (see Appendix I-1 for details on uncertainty estimation), the strain-rate increases significantly over the 29 years, at a rate of $2.4 (\pm 0.4) \times 10^{-4} \text{ day}^{-1}$ per year (i.e. $51\% \pm 8.5\%$ increase per decade) for winter and $2.6 (\pm 0.6) \times 10^{-4} \text{ day}^{-1}$ per year (i.e. $52\% \pm 12\%$ increase per decade) for summer. The trends obtained from our analysis are one order of magnitude greater than the first order estimates previously obtained with the hypothesis of an homogeneous increase of sea ice speed (in %) over the Arctic basin, and so of an homogeneous increase of the deformation rate. As sea ice strain rate is highly heterogeneous [Marsan *et al.*, 2004; Rampal *et al.*, 2008], this first order approximation strongly underestimates the rates of increase of sea ice deformation rates. Furthermore, as shear dominates the total strain-rate within the Arctic basin [Stern and Moritz, 2002], these trends also suggests that shear deformation, and therefore the associated Coulombic faulting [Schulson, 2004; Weiss *et al.*, 2007], significantly increased during the last 29 years.

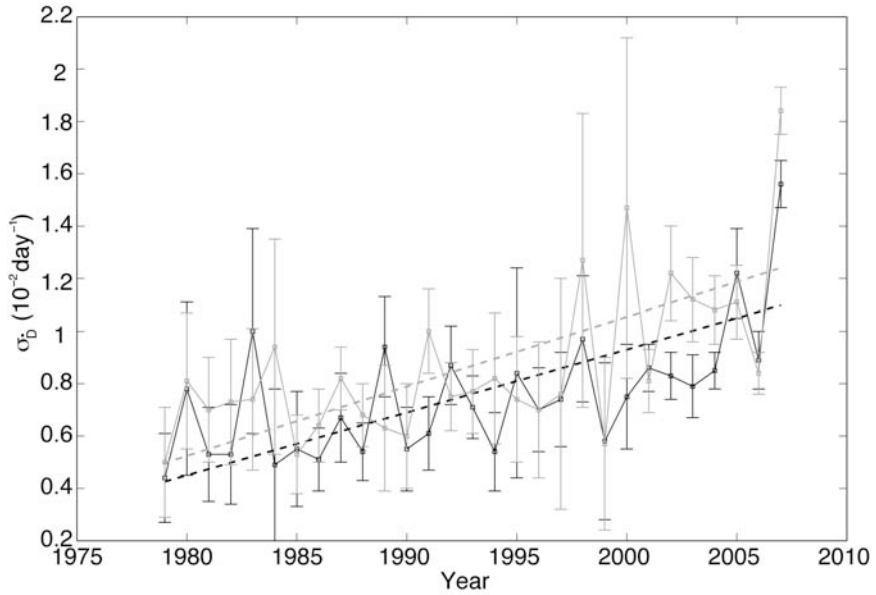


Figure I-9. Sea ice mean strain-rate proxy of the winters and summers of 1979-2007. This proxy is calculated for time scales shorter than 1 day and spatial scales ranging from 50 km to 500 km (see text). Winter mean series are drawn in black while summer mean series are in grey. Associated error bars are estimated from a bootstrap method (see Appendix I-1). The weighted linear fits of the data are plotted as dashed lines and give trends of $2.4 (\pm 0.4) \times 10^{-4} \text{ day}^{-1}$ per year (i.e. $51\% \pm 8.5\%$ increase per decade) for winter and $2.6 (\pm 0.6) \times 10^{-4} \text{ day}^{-1}$ per year (i.e. $52\% \pm 12\%$ increase per decade) for summer.

6. Discussion

We found that both Arctic sea ice speeds and deformation rates significantly increased over the past 29 years. The question is now: why did these increases occur? Two main hypotheses can be formulated:

- (i) The intensity of the external forcing increased, i.e. the oceanic currents and/or winds strengthened over the period.
- (ii) These increases are the consequence of the thinning of the sea ice cover that implies a decreasing mechanical strength, hence an easier fracturing and deformation. This would in turn facilitate melting and export out of the Arctic basin, thus reinforcing the albedo feedback loop and possibly the polar amplification.

6.1 External forcing

Winds and, to a lesser extent ocean currents, are considered to be the two main forcing terms for sea ice drift and deformation. It is not possible to check from the sparse available data a hypothetic trend on ocean current velocity magnitudes over the whole Arctic basin for the period 1979-2007. On the other hand, for the atmosphere, the Arctic Oscillation (AO) index [Thompson and Wallace, 1998] furnishes an indication of the strength of the circulation over the Arctic: During anticyclonic (negative AO) circulation regimes, atmospheric pressure is higher, wind speed is lower, and supposedly sea ice is thicker and its extension larger [Richter-Menge *et al.*, 2006; Rigor *et al.*, 2002]. During positive AO phases, wind speed is larger, wind divergence produces more sea ice opening, and export of sea ice out of the basin is facilitated [Richter-Menge *et al.*, 2006; Rigor *et al.*, 2002]. Since 1979, the annually averaged AO index [National Weather Service] was particularly high from 1989 to 1994, but then fluctuated between negative and positive values, without positive trend. In addition, we did not observe any significant correlation between the seasonally averaged (winter and summer) AO index and our seasonally averaged sea ice mean speeds or deformation rates ($R^2 < 0.2$ in all cases). This suggests that the trends reported here are unlikely a consequence of a stronger wind forcing. To further test this point, we used the ERA-40 reanalysis dataset provided by the ECMWF [European Centre for Medium-Range Weather Forecasts] that gives the two components \bar{u}_x^{wind} and \bar{u}_y^{wind} of the monthly mean wind velocity vector $\bar{\mathbf{u}}^{wind}$ at 10 meters height above the surface on a regular grid of 2.5° by 2.5° and for the period 1979-1999. From this dataset, we firstly computed the monthly mean wind speed at each grid points as follows:

$$\bar{u}^{wind} = \left(\bar{u}_x^{wind 2} + \bar{u}_y^{wind 2} \right)^{(1/2)} \quad (I-6)$$

At high latitude, a 2.5° by 2.5° grid do not cover the Arctic basin homogeneously as numerous grid points lie in the vicinity of the North Pole. Consequently, before computing a mean wind speed value for the Arctic basin, we interpolated the previous mean speeds on a regular grid of 200 km by 200 km using a linear method (i.e. linear weighting of the three nearest speed values). Finally, we computed the monthly mean wind speed $\bar{u}^{wind}(t)$ for the whole Arctic basin and for each month of 1979-2000 by averaging the speeds of the monthly mean field that lie in the "Central Arctic" region (see figure I-1). Figure I-10 displays $\bar{u}^{wind}(t)$ between January 1979 and December 1999. A linear fit (in the least square sense) of the data gives a trend of $1.2 (\pm 0.8) \times 10^{-3}$ m/s per year, i.e. an increase of 0.4% per decade. We thus conclude that there is no significant increase (in terms of wind speed) of the atmospheric forcing over the period 1979-

2000. This does not rule out a possible role of atmospheric circulation *patterns* onto e.g. sea ice export through Fram Strait [Kwok and Rothrock, 1999, Kwok *et al.*, 2004].

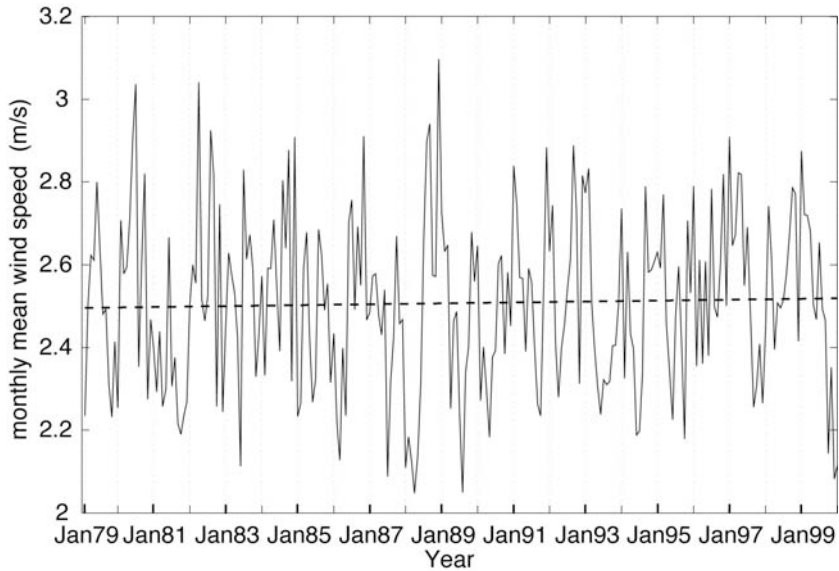


Figure I-10. Monthly mean wind speed $\bar{u}^{\text{wind}}(t)$ between January 1979 and December 1999. The means are computed from the two velocity components of the estimated wind velocity vector of the ERA-40 reanalysis dataset. A linear fit (in the least square sense) of the data gives a trend of $1.2 (\pm 0.8) \times 10^{-3}$ m/s per year (i.e. an increase of 0.4% per decade) and is drawn as a dashed black line.

6.2 Sea ice deformation, thinning and export

Arctic sea ice thinning over the last decades is now clearly identified: the annual mean ice draft determined from submarine sonars declined from about 3.4 m in 1980 to about 2.3 m in 2000, corresponding to an average decrease of 1.2 m in thickness [Rothrock *et al.*, 2008]. This decline most likely participates to a decrease of the sea ice mechanical strength, and then favors an increase of sea ice deformation rates and associated fracturing during the period. As a fragmented ice cover is easier to drag, this may also participate to the actual increase of sea ice mean speed observed in the Central Arctic region and could possibly facilitate sea ice export through Fram Strait. *Kwok and Rothrock* [1999] and *Kwok et al.* [2004] examined the sea ice area flux through Fram Strait from passive microwave ice motion data, and found a small positive trend over the period 1978-2002.

Here, we consider the sea ice mean speed along the Greenland coast (The “Fram” region of figure I-1). We note that the sea ice area flux estimated in the previous works cited above depends on both magnitude and direction of velocity vectors that crossed the Fram Strait line, whereas here we only consider a scalar. From the actual sea ice mean speed increase in the Central Arctic, one could hypothesize that, over the period of interest, the sea ice mean speed in the “Fram” region also increased. Positive trend of 13×10^{-2} km/day per year were recently reported for the Fram Strait and the northern part of the Barents Sea for the period 1979-2005 from a combined analysis of satellite and buoys data [*Pavlov and Pavlova*, 2007]. These trends are twice larger than our trends reported in section I-3 for the “Central Arctic”. As the buoy trajectories are too sparse in the “Fram” region, we analyzed the satellite-derived velocity estimates provided by the Jet Propulsion Laboratory [*Polar remote sensing group*]. The sea ice velocities are computed for winters between 1979 and 2004 with a sampling of two days and their uncertainties are about 10% [*Kwok and Rothrock*, 1999]. From this dataset, we selected the velocities in a region along Greenland and below approximately 82°N of latitude (The “Fram” region of figure I-1). For the period 1979-2004, we calculated the mean winter-speeds, averaged over 5 ½ months, i.e. between December and the following 15th of May (figure I-11). A weighted linear fit of the data gives a positive trend of $5.6 (\pm 2.0) \times 10^{-2}$ km/day per year (i.e. 7% \pm 2.5% increase per decade). However, this trend is less significant than those observed for the Arctic basin, as the result of large uncertainties on mean drift estimates partly due to rather large uncertainties on the satellite-derived velocities. Nevertheless, we may interpret this positive trend as (i) a response to the change in the Arctic basin kinematics presented above, this later favored by a thinning of the sea ice cover in the “Central Arctic”, and/or (ii) as a direct effect of thinner ice on sea ice kinematics in the “Fram” region.

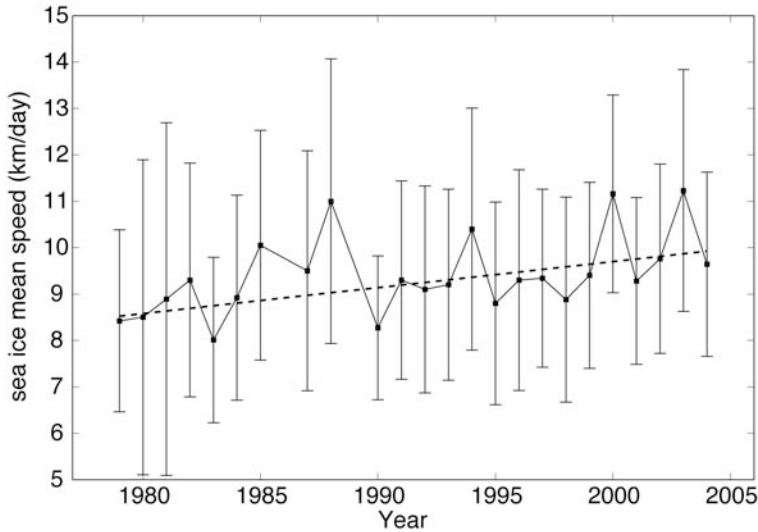


Figure I-11. Sea ice mean drift along the Greenland coast during winter, from 1979 to 2004. The means are computed from a SSM/I-derived velocity dataset, and averaged from the 1st of December and the 15th of the following May. The error bars are estimated from the bootstrap method presented in section 3. A weighted linear fit is shown (dashed line), and gives a trend of $5.6 (\pm 2.0) \times 10^{-2}$ km/day per year (i.e. 7.5% increase per decade).

Although a significant correlation ($R^2 \approx 0.4$) was found between the sea ice area flux through Fram Strait and the NAO index from 1978 to 2002 [Kwok *et al.*, 2004], we did not find here any significant correlation ($R^2 < 0.1$) between the winter's AO index and our winter mean *speed* in the “Fram” region.

If sea ice fracturing and deformation are facilitated by thinning, the reverse might be true, as a more fractured/fragmented sea ice cover means (i) more lead opening, stronger melting during summer and a delayed refreezing in early winter, and (ii) possibly an easier export of ice out of the Arctic basin. This coupling between sea ice deformation and fracturing in one hand, and sea ice extent and thickness on the other hand can easily explain that the sea ice drift record is out of phase with the sea ice extent and thickness [Rothrock *et al.*, 2008] record (see figure I-4). Consequently, sea ice kinematics and fracturing could strengthen the albedo feedback loop, the polar amplification and the associated decline of the Arctic sea ice cover.

6.3 Year 2007

The year 2007 might be a good illustration of such positive feedbacks between deformation and sea ice decline.

Exceptionally large mean deformation rates are recorded both in winter and summer 2007 (see figure I-9). Moreover, their associated error bars are small, as the result of a great amount of pairs of buoys available during this year. Computing the linear trends of the deformation rate increases over the period 1979-2006 (i.e. excluding 2007), one obtains $1.0 (\pm 0.4) \times 10^{-4} \text{ day}^{-1}$ per year for winter and $2.0 (\pm 0.5) \times 10^{-4} \text{ day}^{-1}$ per year for summer, i.e. respectively 50% and 25% lower than the trends estimated over the period 1979-2007. The σ_d -values predicted for 2007 following the 1979-2006 trends, noted $\sigma_d^{2007(\text{predict})}$, would be $0.9 (\pm 0.1) \times 10^{-2} \text{ day}^{-1}$ in winter and $1.1 (\pm 0.2) \times 10^{-2} \text{ day}^{-1}$ in summer (here, the bracketed values are the standard deviations $\Delta\sigma_d^{2007(\text{predict})}$ of the predicted values). The values of deformation rate recorded in 2007 and noted $\sigma_d^{2007(\text{record})}$ are equal to $\sigma_d^{2007(\text{predict})} + 6 \times \Delta\sigma_d^{2007(\text{predict})}$ and $\sigma_d^{2007(\text{predict})} + 3.5 \times \Delta\sigma_d^{2007(\text{predict})}$ for winter and summer respectively. This indicates that these 2007 values are indeed exceptionally large compared to the 29-years linear trends, just as the 2007 September sea ice extent was exceptional compared to the 29-years average decline of sea ice minimum extent [Stroeve *et al.*, 2008].

Now, the question is: why do the records of 2007 deviate so strongly from the 1979-2006 positive trend, and is this related somehow to the 2007 sea ice minimum extent? The role of the mechanical behavior of sea ice and its deformation on the ice-albedo feedback loop, and thus on sea ice thinning, is induced by the fracturing/faulting of the cover, which result from its elasto-brittle rheology [Weiss *et al.*, 2007; Rampal *et al.*, 2008]. Brittle behavior is by nature a highly non-linear, threshold mechanics. The exceptional 2007 deformation rates may suggest that the mean sea ice thickness, and so its mechanical strength, has passed a threshold over a large part of the Arctic below which its fracturing and collapse is highly facilitated, leading to an abrupt change in its mechanical response to the various forcing.

Perovich *et al.* [2008] showed that the solar heating of the upper ocean was the primary source of heat that led to an extreme sea ice melting during the summer 2007 in the Beaufort Sea region. They argued for an increase in area of open water as the cause of the upper ocean heating and asked for the process that triggered this increase. A stronger fracturing, favored by the thinning of sea ice, is a possible cause of such increase in area of open water. This is in agreement with Lindsay *et al.* [2008] who recently concluded that the unusual retreat of the sea ice in 2007 was pre-conditioned by decades of gradually warming temperatures and the replacement of older

ice by younger ice, resulting in a thinner ice pack. This preconditioning may have lead the 2007 sea ice cover to pass a threshold in terms of mechanical strength, which would have in turn (i) implied a strong melting/thinning of sea ice in some regions of the Arctic during summer 2007 [Perovich *et al.*, 2008] and (ii) facilitated its advection from the Pacific sector to the Atlantic sector of the Arctic basin in response to the persistent southerly winds recorded in summer 2007 [Lindsay *et al.*, 2007], and then finally participated to the 2007 sea ice shrinking.

7. Conclusion

In both winter and summer, Arctic sea ice decline is accompanied, and most probably strengthened, by increases at significant rates of sea ice speed and deformation rate (sections 3 & 5). This evolution of sea ice kinematics probably strengthens positive feedbacks in sea ice evolution through an intensification of fracturing-induced deformation of the sea ice cover, implying an increase of lead opening and therefore a decrease of the surface albedo, and possibly an increase of sea ice export (section 6). Classical sea ice models, based on a continuum mechanics, fluid-like framework with a viscous-plastic or an elastic-viscous-plastic rheology, are not able, by nature, to correctly represent the brittle fracturing/faulting of sea ice [Coon *et al.*, 2007; Rampal *et al.*, 2008; Schulson, 2004; Weiss *et al.*, 2007], as well as the induced strain-rate fields [Thomas, 1999] (Girard *et al.*, **in prep.**, 2008). One can therefore wonder about their ability to properly model the role of fracturing/faulting into the albedo feedback loop. This might explain partly why climate models underestimate sea ice decline [Stroeve *et al.*, 2007; Serreze *et al.*, 2007].

Acknowledgements We thank I. Rigor from the Polar Science Centre of Seattle for the compilation and the distribution on the web of the IABP dataset. We also thank the ECMWF and the JPL for the compilation and the distribution of the ERA-40 dataset and the SSM/I dataset respectively. Thank also to the National Weather Service of the NOAA for the distribution of the AO index time series. A special thank to the DAMOCLES European program and the Tara expedition who motivated this analysis.

Appendix I-1: Estimating uncertainties on $\sigma_{\dot{D}}$, the standard deviation of \dot{D} .

Time correlations (memory effects) are present in ice velocity records [Thorndike, 1986] (Rampal *et al.*, **in prep.**, 2008), and can also be found in time series of ice deformation rates as approximated by the dispersion of pairs of buoys. An autocorrelation analysis reveals a correlation time of about 10 hours for an initial separation of $L=300$ km [Rampal *et al.*, 2008]. This correlation time becomes smaller for small L . In addition, strong spatial correlations are present in the deformation field [Marsan *et al.*, 2004]. Consequently, the errors on the estimation of $\sigma_{\dot{D}}$ cannot be obtained directly from the central limit theorem and the number N of samples. Instead, we estimate these errors from the same bootstrap method than in section 3.1, with the difference that the number of pairs of buoys N_p taken into account in each distribution, rather than the number of samples N , should be used as the number of independent variables. In each “annual” distribution, we randomly picked q times ($q \geq 10$), all the \dot{D} -values coming from n independent pairs of buoys, taking care not to pick the same pair twice, with the condition $q \times n \approx 0.75N_p$. Then, we obtain q distributions of \dot{D} -values for which we calculate their standard deviation $\sigma_{\dot{D}}^{bootstrap}$. The dispersion of the $\sigma_{\dot{D}}^{bootstrap}$ -values, i.e. their standard deviation noted $\Delta\sigma_{\dot{D}}^{bootstrap}$, is computed for each given n . Finally, we obtain that $\Delta\sigma_{\dot{D}}^{bootstrap}$ decreases with n as $\Delta\sigma_{\dot{D}}^{bootstrap} = (A \times \sigma_{\dot{D}}^{bootstrap}) / n^\lambda$ where A is about 0.9, and λ is approximately equal to 0.4. We note that this expression is similar to the error estimate given by the central limit theorem, with the important difference that the number of pairs of buoys N_p is considered instead of the number of samples N . Also, the values of A and λ differ slightly from $A=1$ and $\lambda=0.5$ as would be expected if the central limit theorem would apply.

Chapitre II :

Champ de vitesse

de la banquise Arctique

D'après:

Rampal, P., J. Weiss, D. Marsan and M. Bourgoin (2008), Arctic sea ice velocity field: general circulation and turbulent-like fluctuations, **submitted** to *Journal of Geophysical Research-Ocean*

Abstract :

Using buoys trajectories of the IABP dataset, we analyze the Arctic sea ice velocity field in terms of a mean part, and its fluctuations. We show that the fluctuations have to be computed by subtracted from the total velocity field a mean field estimated for appropriate spatial and temporal averaging scales, depending on the season considered. These appropriate averaging scales are 400 km and 5 ½ months for winter (i.e. approximately all the polar winter duration), and 200 km and 2 ½ months for summer (i.e. approximately all the polar summer duration). Computing at these scales, the mean velocity field of sea ice show a strong intra-annual (between winter and the following summer) as well as interannual variability. The fluctuations, i.e. the remained part of the velocity field after removing the mean field, are analyzed in terms of diffusion properties. Although the Arctic sea ice cover is a solid, we show that these follows the same diffusion regimes than the ones predicted for turbulent flows by the theory of Taylor (1921), as observed in many geophysical fluids like the ocean or the atmosphere. We found that the integral time and the diffusivity of sea ice are in the same ranges than those estimated for the ocean, i.e. 1.5 days in winter and 1.3 days in summer, and 0.44×10^3 m²/s for winter and 0.45×10^3 in summer, respectively. However, the statistics of the sea ice fluctuating velocity deviate from the Taylor's theory, as they show exponential distributions. A deeper analyzes of these distributions reveals the intermittency of sea ice velocity and acceleration, both characterized by a multifractal scaling. This is interpreted in terms of dynamic forcing of sea ice: The oceanic and atmospheric dynamic forcing cannot explain solely the statistical properties of sea ice kinematics and dynamics. We argue that sea ice dynamic is significantly influenced by the interplay of multiple fractures that are activated intermittently within the ice pack.

1. Introduction

“The motion of a particle of sea ice can be partitioned into a predictable component, associated with the long-term average wind and ocean currents, and a random part associated with the short-term fluctuations in the wind and current” [Thorndike, 1986a]. This citation suggests (i) the existence of a general circulation in the Arctic, and (ii) that the random part simply results from ocean and atmosphere turbulence. Coming back on this problem, we ask here the following questions: (i) At which averaging scales (temporal & spatial) can we define unambiguously a general circulation of Arctic sea ice? (ii) What are the statistical properties of the fluctuating part of its motion ? To what extent can we qualify the sea ice motion as turbulent-like ?

In order to investigate this problem, we use a strong analogy with the approach used to study fluid turbulence and its associated diffusion properties. In fluid studies, the fluctuating part of the motion is commonly attributed to turbulence, and is distinguished from a predictable (in a deterministic sense) part, also called “mean flow”. In other words, the Lagrangian or Eulerian velocities of parcels of a turbulent fluid are commonly decomposed into a mean velocity and its fluctuations (the so-called *Reynolds decomposition*) in order to characterize various turbulent properties of the fluid. Here, we do the same for the Arctic sea ice velocities from a dataset of buoys trajectories. Indeed, drifting buoys fixed to the sea ice cover were installed in the Arctic basin every year since 1978. These buoys can be considered as passive tracers (i.e. Lagrangian particles) of sea ice, like parcels would be for a fluid. The positions of the buoys that drifted according to sea ice motion, sometimes during more than one year, were recorded and made available by the International Arctic Buoy Program (IABP) (see section 2 for more details). A qualitative look at a map of buoy’s trajectories leads anybody to think about a “spaghetti” plot (see figure 1). Similar patterns were observed for fluid parcels [Bourgois et al., 2006], ocean surface drifters [Haynes, 199; Martins, 2002] or isopycnal floats [Zhang et al., 2001], passively moving on in turbulent fluids. Like in all these cases, the motion of buoys appears to be forced by complex underlying processes.

The possible analogy between sea ice motion and the motion of fluid parcels in a turbulent flow was remarkably introduced by *Thorndike and Colony* [1986b], who proposed a model to reproduce the mixing properties of the fluctuating velocity field. In another paper, *Colony and Thorndike* [1984] attempted to define the “Arctic mean general circulation” (AMGC). To do so, they estimated the mean field of sea ice motion using arbitrary spatial and temporal averaging scales of about 200 km and 90 years, from an interpolation (based on an optimal linear method [Gandin, 1963]) of about 100 trajectories recorded between 1893 and 1983. These averaging

scales may not be appropriate in the following sense: If the mean field of sea ice motion is estimated at too large spatial and/or temporal averaging scales, homogenization would be too strong and details of the mean circulation would be lost. On the contrary, if the mean field is estimated at too small averaging scales, it would include a stochastic component coming from the fluctuating part of the motion and then biases the analysis of the velocity fluctuations as well as their causes (e.g. the forcing terms and their associated physical processes that are responsible for these fluctuations).

So, let us come back now to the complex paths followed by the drifting buoys in the Arctic. The complexity of buoy trajectories suggests that sea ice velocities locally deviate from the mean velocity field (i.e. associated to the AMGC) as they show sudden changes in direction and magnitudes. One expects these velocity fluctuations to result from different forcing terms. In summer, the sea ice velocity fluctuations estimated by *Thorndike and Colony* [1982] seem to be highly correlated with fluctuations in the geostrophic wind in the central Arctic region. On the other hand, a large part of the velocity fluctuations in winter and near the coasts (i.e. within about 400 km from the coasts, according to these authors) seem to be unexplained by wind and/or current fluctuations [*Thorndike and Colony*, 1982]. This suggests that the unexplained motion could be also the fingerprint of sudden displacements due to the activation of fractures and faults in the sea ice pack that is associated to the intermittent sea ice cover deformation [*Rampal et al.*, 2008].

In this paper, we propose an original approach inspired from the study of fluid turbulence that allows us to define objectively (i.e. by an absolute manner) the sea ice motion as a superposition of a mean motion and fluctuations. In section 2, we present briefly the dataset that we used in this study. In section 3, we estimate the appropriate spatial and temporal averaging scales to extract the mean pattern of sea ice motion, say the AMGC. Then, for both polar seasons, we discuss about the primary statistics of the mean velocity field of sea ice corresponding to the estimated AMGC. In section 4, we characterize the properties of the fluctuating part of the motion and we discussed these properties in terms of turbulent-like signature. We conclude in section 5.

2. Dataset: Lagrangian trajectories of buoys

The drifting buoys dataset is provided by the International Arctic Buoy Program (IABP) and is available on the web (<http://www.iabp.apl.washington.edu>). We selected approximately 450 drifters deployed between 1979 and 2001 over the entire Arctic basin (see figure II-1). The selection of the buoys is based on two criterions. The first was the quality of the data, i.e. in terms of duration and sampling regularity. The second criterion was based on the distance of the trajectories from the nearest coast: the positions recorded at a minimum distance of 100 km from the coasts were selected. From the selected trajectories, we separated the positions recorded in winter (i.e. from the beginning of November to the middle of May of the following year) from those recorded in summer (from the middle of June to the middle of September). The buoy positions distributed by the IABP differ slightly from the true positions sampled by the buoys: The actual buoy's tracks were irregularly sampled through time, with a mean time interval of 1 hour. Errors on these positions range from 100m to 300m, depending on the type of the positioning system embarked on the buoy [Thomas, 1999]. In order to obtain a more regular sampling, a cubic interpolation of the raw positions was first performed, before re-sampling these at 3-hour time interval. In other words, the IABP data are the gathering of the filtered buoy trajectories. The reference coordinate system used in this study is a Cartesian coordinate system centered on the North Pole with the vertical axis (i.e. the y-axis) following the Greenwich meridian. Each latitude-longitude buoy position is expressed in the orthogonal base $(\mathbf{e}_1, \mathbf{e}_2)$ of this coordinate system as $\mathbf{x}_{(lat,long)} = x\mathbf{e}_1 + y\mathbf{e}_2$ using a polar stereographic projection. From the positions we computed the two components (i.e. along x-axis and y-axis) of the 3-hourly velocity vectors \mathbf{u} as:

$$u_x(\tilde{x}, \tilde{t}) = (x(t+3h) - x(t)) / 3h \quad (\text{II-1})$$

$$u_y(\tilde{y}, \tilde{t}) = (y(t+3h) - y(t)) / 3h \quad (\text{II-2})$$

where $\tilde{x} = (x(t+3h) + x(t))/2$, $\tilde{y} = (y(t+3h) + y(t))/2$ and $\tilde{t} = ((t+3h) + t)/2$. Positions uncertainties give errors on the speed estimates ranging from 1.3 to 3 cm/s.

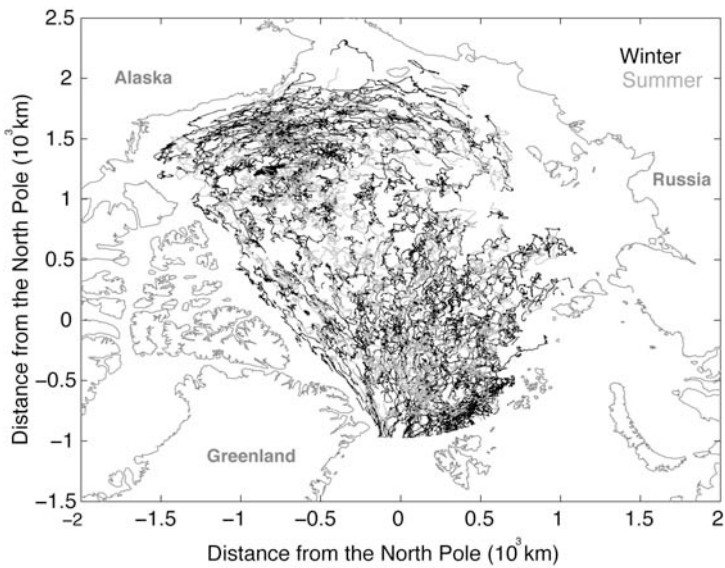


Figure II-1. Map of the Arctic basin showing 450 buoy tracks from the IABP dataset. These trajectories were recorded between December 1978 and December 2001.

3. Estimating the mean velocity field $\langle \mathbf{u}(\mathbf{x},t) \rangle$ of the Arctic sea ice

ice

In this section, we will first remind how we commonly study the diffusion properties of a turbulent fluid (subsection 3.1), and more particularly, how we define and compute a mean velocity field $\langle \mathbf{u}(\mathbf{x},t) \rangle$ and its respective fluctuations $\mathbf{u}'(\mathbf{x},t)$ (the so-called Reynolds decomposition) from Lagrangian velocities $\mathbf{u}(\mathbf{x}(t),t)$ records (subsection 3.2). Classically, such decomposition of a flow into a mean part and fluctuations can be used to study the turbulent transport of the given flow. To do so, one computes the Lagrangian statistics of the fluctuating velocity field. These statistics are dependent on the partitioning of the velocity field, i.e. depend strongly on the spatial and temporal averaging scales chosen to estimate the mean field $\langle \mathbf{u}(\mathbf{x},t) \rangle$ [Bauer *et al.*, 1998; Zhang *et al.*, 2001]. To determine the spatial and temporal averaging scales at which the partitioning should be performed, one has to consider the stability of the Lagrangian statistics, i.e. the correlation properties of the fluctuating field (see subsection 3.2).

Using an original approach based on an analogy between the motion of buoys fixed to the sea ice cover (i.e. a fractured solid plate) and the motion of fluid parcels in a turbulent flow, we explore the influence of the choice of the spatial and temporal averaging scales on the Lagrangian statistics for the Arctic sea ice (see subsection 3.3). The results are presented in subsection 3.4. Using appropriate averaging scales deduced from this investigation, we compute examples of such mean velocity fields and we discuss their properties (see subsection 3.5).

3.1 Classical approach: the turbulent diffusion theory (Taylor, 1921)

Taylor [1921] showed that in case of steady and homogeneous turbulence without mean flow, single-particle dispersion through time (i.e. the variance of the distance from its origin) $\langle r'^2(t) \rangle$ is related to the normalized turbulent autocorrelation function $C(\tau)$ as follows:

$$\langle r'^2(t) \rangle \sim 2\langle u'^2 \rangle \int_0^t C(\tau) d\tau \quad (\text{II-3})$$

where $\langle u'^2 \rangle$ is the fluctuating speed variance. \mathbf{u}' is the fluctuating velocity defined as $\mathbf{u}' = \mathbf{u} - \langle \mathbf{u} \rangle$.

The turbulent autocorrelation function $C(\tau)$ is defined as follows:

$$C(\tau) = \frac{1}{\langle u'^2 \rangle} \int_0^{T_{\max}} \mathbf{u}'(t) \mathbf{u}'(t + \tau) dt \quad (\text{II-4})$$

where T_{\max} is the maximum time of data coverage. Theoretically, $C(\tau)$ decreases with increasing time lag (e.g. following an exponential decay) as particles lose the memory of their previous displacements, and a characteristic memory time Γ (also called integral time) for $C(\tau)$ does exist [*Taylor*, 1921]. In other words, this implies that $C(\tau)$ tends to zero in a finite time and that one can define the memory time Γ , i.e. “integral time scale”, as follows:

$$\Gamma = \int_0^\infty C(\tau) d\tau \quad (\text{II-5})$$

From equation (II-3) and (II-5), we deduce that particle dispersion $\langle r'^2(t) \rangle$ has two asymptotic regimes. For $t \ll \Gamma$, one obtains:

$$\langle r'^2(t) \rangle \sim \langle u'^2 \rangle t^2 \quad (\text{II-6})$$

that is, the variance of the turbulent displacement grows with t^2 . This is the so-called “ballistic” regime or “initial growth” stage. For $t \gg \Gamma$, one obtains:

$$\langle r'^2(t) \rangle \sim 2\langle u'^2 \rangle \Gamma t \quad (\text{II-7})$$

that is, the variance of the turbulent displacement grows with t , i.e. like single-particle dispersion for molecular diffusion. In fact, this regime is the direct consequence of (i) the Gaussian statistics of the turbulent speed and (ii) the fact that, at $t \gg \Gamma$, the velocity correlations vanish. On the other hand, the Lagrangian turbulent diffusivity K provides a measure of the rate of spreading of a particle from its initial position, which gives the rate of change of the root mean square particle position relative to the mean trajectory of the particle. K is defined as:

$$K = \frac{1}{2} \frac{d\langle r'^2(t) \rangle}{dt} \quad (\text{II-8})$$

From (II-7) & (II-8), one obtains that for $t \ll \Gamma$,

$$K = \langle u'^2 \rangle t \quad (\text{II-9})$$

and for $t \gg \Gamma$,

$$K = \langle u'^2 \rangle \Gamma \quad (\text{II-10})$$

3.2 Definition of the mean velocity $\langle \mathbf{u} \rangle$

In his theory, *Taylor* (1921) considers the turbulent velocity \mathbf{u}' of a flow. The turbulent velocity is deduced by subtracting the mean velocity $\langle \mathbf{u} \rangle$ from the velocity \mathbf{u} . The question is: How do we compute the mean?

When Lagrangian observers (mainly drifters and floats) were first used in ocean observations, they were used in such limited numbers that it was necessary to estimate and use a constant mean velocity over the whole observational domain [*Freeland et al.*, 1975; *Riser et al.*, 1983; *Colin de Verdière et al.*, 1983; *Sundermeyer et al.*, 1998]. As the number of observations increased, it was possible to resolve, to a limited extent, the spatial variations of the mean flow, say by binning observational data in large boxes [*Krauss et al.*, 1987; *Spall et al.*, 1993; *Poulain et al.*, 1996]. This is an improvement over the uniform mean flow, but in strong current regions the data density is not high enough to extract details of the highly structured mean flow.

More generally, $\langle \mathbf{u}(\mathbf{x},t) \rangle$ can be considered as the Eulerian velocity field smoothed at spatial and temporal scales L and T , and denoted $\langle \mathbf{u}(\mathbf{x},t) \rangle_{L,T}$. The general expression for $\langle \mathbf{u}(\mathbf{x},t) \rangle_{L,T}$ is

$$\langle \mathbf{u}(\mathbf{x},t) \rangle_{L,T} = \int_x \int_t \Phi_{L,T}(\mathbf{x} - \mathbf{x}', t - t') \mathbf{u}(\mathbf{x}', t') dt' d\mathbf{x}' \quad (11)$$

where $\Phi_{L,T}(\mathbf{x},t)$ is a smoothing kernel with the two characteristic scales L and T . Here, the mean $\langle \mathbf{u} \rangle_{L,T}$, and consequently its associated fluctuation \mathbf{u}' , depend on the choice of the averaging scales L and T .

Zhang et al. [2001] and *Bauer et al.* [1998] studied the influence of L on the Lagrangian statistics of flows in oceanic regions (the North Atlantic Current region and the tropical Pacific Ocean, respectively) from float datasets. For example, taking the largest temporal window allowed by their dataset for T (i.e. 2 years) and L (i.e. the length of box side) ranging from 0.3° to 4° , *Zhang et al.* [2001] found a strong dependence of (i) the turbulent velocity variance, (ii) the integral time of correlation Γ , (iii) the integral length of correlation Λ (see below for a definition) and (iv) the turbulent diffusivity K , on the spatial averaging scale L used. Nevertheless, above a threshold value $\tilde{L}=0.5^\circ$, they observed that these statistics remained constant. In the works of *Zhang et al.* [2001] and *Bauer et al.* [1998], such saturation in the Lagrangian statistics is interpreted as the fact that an averaging of Lagrangian velocities at the scale \tilde{L} allows to correctly

resolve the spatial structure of the mean flow, i.e. avoid to embed in the residual turbulent field the unresolved mean velocity structure.

To further illustrate this point, and introduce in the same time our following analysis, let us consider a set of about 30 trajectories from the IABP dataset. We compiled this set by selecting all the positions of 30 buoys recorded during the winter 1992-93, i.e. between the beginning of December 1992 and the 15th of May 1993. From their 3-hourly Lagrangian velocities $\mathbf{u}(\mathbf{x}(t), t)$, we estimated at each position \mathbf{x} of all the 30 buoys the mean velocity noted $\langle \mathbf{u}(\mathbf{x}) \rangle_{L,T}$ by averaging their velocities over different couples of spatial and temporal scales (L, T) (see subsection 3.3 for a complete description of the mean estimation methodology). Then, we calculated the local fluctuating velocity as:

$$\mathbf{u}'(\mathbf{x}(t), t) = \mathbf{u}(\mathbf{x}(t), t) - \langle \mathbf{u}(\mathbf{x}) \rangle_{L,T} \quad (\text{II-12})$$

Figure II-2 displays the displacements $r'(t)$ of each buoy due to the local fluctuating velocity $\mathbf{u}'(\mathbf{x}, t)$ computed following (II-12) for the different couples (L, T) . The initial positions of the fluctuating trajectories (i.e. $\mathbf{x}'(t=0)$) as well as of each trajectories (i.e. $\mathbf{x}(t=0)$) of the 30-buoys dataset have been set to $(0,0)$. Looking at the size of the region containing the displacements $r'(t)$, we can, at least graphically, estimate the integral length Λ . Λ is defined as the translation in the spatial domain of the integral time Γ , and is commonly estimated as $\Lambda = \langle u'^2 \rangle^{1/2} \Gamma$ [Frisch, 1995]. This corresponds to a characteristic length scale, e.g. a characteristic size of structure in case of turbulent flows. We can deduce from the figure 2 that Λ (and thus Γ) increases with L and T until a maximum reached for \tilde{L} and \tilde{T} of about 400 km and 160 days (i.e. 5 ½ months) approximately. Thus, by averaging at these scales, no spatial and/or temporal correlations inherent to the fluctuating velocity field remain in the mean field. In other words, the mean velocity field can be considered as homogeneous and stationary [Figueroa and Olson, 1994], i.e. the diffusion follows the theory of *Taylor* [1921]. We conclude that these scales are appropriate to estimate the mean as well as the fluctuating velocity fields. Another interesting remark is that in despite of asymmetric total trajectories, the fluctuating trajectories are well symmetric, i.e. the fluctuating displacements are isotropic around the reference point $(0,0)$.

Hereafter, we study the influence of the choice of the averaging scales on the integral time Γ defined in (II-5) for the entire IABP dataset. The goal of this study is to find the smallest

averaging scales (i.e. the highest resolution for the Eulerian mean field) above which Γ remains essentially unchanged.

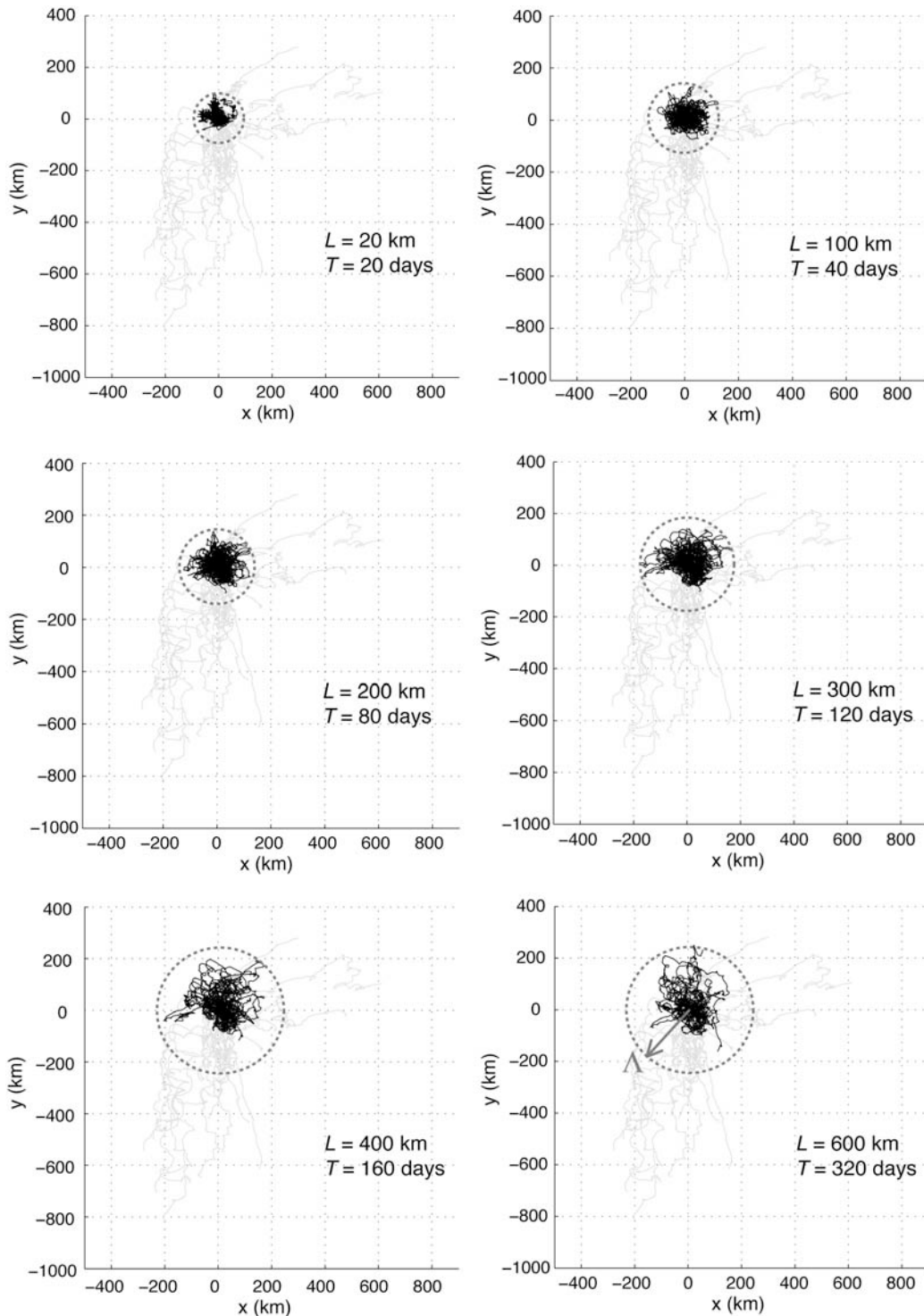


Figure II-2. Displacements fluctuations $r'(t)$ (in black) of buoys that worked during the winter 1992-93 (i.e. 30 trajectories). These displacements are linked to the fluctuating velocity field deduced from mean velocity fields estimated for different couple (L, T) . The actual displacements $r(t)$ of the buoys are drawn in grey. The initial positions of the fluctuating (i.e. $x'(t = 0)$) as well as the actual trajectories (i.e. $x(t = 0)$) of each buoy have been set to $(0,0)$. Looking at the size of the region containing the displacements $r'(t)$ (marked as the dashed grey circles), we can see the dependence of the integral length Λ on the spatial and temporal averaging scales.

3.3 Methodology

Let us index by q the buoys of our dataset ($1 < q < N$). N is the total number of the selected buoys trajectories, i.e. approximately 350 in winter and 230 in summer. The quality and the density of the drifting buoys observations allow us to estimate for each position \mathbf{x}_{ref} reached at time t_{ref} by the drifting buoy q , an associated mean velocity $\langle \mathbf{u}(\mathbf{x}_{ref}, t_{ref})_q \rangle_{L,T}$ viewed by the drifter q as the mean flow. To do this, for each location $(\mathbf{x}_{ref}, t_{ref})$ we pick out from our dataset the n velocity vectors \mathbf{u}_k ($1 < k < n$) situated in a circle of diameter L centered on \mathbf{x}_{ref} and in a temporal window of duration T centered on t_{ref} .

At this stage, we can do the following remark: Let us sort the n vectors in ascending order as a function of their separation r_k from \mathbf{x}_{ref} . Now, the vectors and their separation from \mathbf{x}_{ref} are indexed by their rank i and noted \mathbf{u}_i and r_i respectively ($1 < i < n$). If these n vectors were densely spaced around \mathbf{x}_{ref} , the cumulative number of velocity vectors noted $N(< r)$ situated within the circle of radius r centered on \mathbf{x}_{ref} would increase as r^2 . Looking at the evolution of the rank i as a function of r_i , we checked that $i \sim r_i^d$ with $d < 2$ and that d decreases with L decreasing, i.e. the dense repartition hypothesis is less and less true as one decreases the spatial scale of observation. This can be understood as the result of a spatial heterogeneity of the data due to the fact that (i) a significant part of the n -vectors belongs to the same buoy q considered, and (ii) some sets of buoys were launched at the same time in the vicinity of each others (i.e. “bunch” launches). The mean velocity computed from the n vectors matching a spatial window of scale L would then be biased if we use a uniform weighting, as we would apply too much importance to the velocity vectors situated in the vicinity of \mathbf{x}_{ref} . So we take into account for this effect in the weights calculation by computing a correcting term w_i^c associated to each velocity vector \mathbf{u}_i and corresponding to the deviation of $N(< r_i)$ from r_i^2 as $w_i^c = r_i^2 / i$.

Let us go back now to the mean calculation. For each velocity \mathbf{u}_k , we compute the weighting coefficient w_k depending on (i) the separation $r_k = \|\mathbf{x}_{ref} - \mathbf{x}_k\|$, (ii) the time lag $\tau_k = |t_{ref} - t_k|$ and (iii) the bias due to spatial heterogeneity w_i^c as follows:

$$w_k = w_i^c e^{\left(-\frac{r_k^2}{2L^2} - \frac{\tau_k^2}{2T^2} \right)} \quad (\text{II-13})$$

We note here that we consider in our weight calculation Gaussian kernels in time and space, i.e. the function $\Phi_{L,T}$ of equation (II-11) is taken as Gaussian. We compute the mean velocity associated to the buoy q at location $(\mathbf{x}_{ref}, t_{ref})$ for the averaging scales L and T as:

$$\langle \mathbf{u}_q(\mathbf{x}_{ref}, t_{ref}) \rangle_{L,T} = \frac{1}{\sum_k w_k} \sum_k w_k \mathbf{u}_k \quad (\text{II-14})$$

We deduce from the mean $\langle \mathbf{u}_q(\mathbf{x}_{ref}, t_{ref}) \rangle_{L,T}$ the fluctuating velocity of the buoy q as $\mathbf{u}'_q(\mathbf{x}_{ref}, t_{ref}) = \mathbf{u}_q(\mathbf{x}_{ref}, t_{ref}) - \langle \mathbf{u}_q(\mathbf{x}_{ref}, t_{ref}) \rangle_{L,T}$. Then, we compute the normalized autocorrelation functions $C_q^{L,T}(\tau)$ of \mathbf{u}'_q following (II-4) for L and T varying from 20 to 600 km and from 10 to 240 days respectively, and for τ ranging from 0 to 20 days by steps of 3 hours. We compute the normalized and weighted mean autocorrelation function $\chi^{L,T}(\tau)$ by averaging over all the trajectories available as:

$$\chi^{L,T}(\tau) = \langle C_q^{L,T}(\tau) \rangle = \frac{1}{\sum_q T_{\max}^q} \sum_q T_{\max}^q C_q^{L,T}(\tau) \quad (\text{II-15})$$

We note here that the weights are equal to T_{\max}^q , and therefore depend on the duration of the trajectory. We checked that our functions $\chi^{L,T}(\tau)$ tends to zero in a finite time and that we can define the integral time scale $\Gamma^{L,T}$ (see subsection 4.1 for further details). However, the finite length of the time series of buoy's positions leads to problems when determining such integral time scale $\Gamma^{L,T}$ by (II-5) since we cannot integrate to infinity. The usual practice integrates $\chi(\tau)$ from zero to the time of the first zero crossing also called "time of integration". This corresponds to the first maximum of the integral scale and the result obtained can be regarded as an upper bound to the true scale [Poulain and Niiler, 1989]. Consequently, we estimate the integral time scale $\Gamma^{L,T}$ associated to each correlation function $\chi^{L,T}(\tau)$ following (II-5) as

$$\Gamma^{L,T} = \int_0^{t_0} \chi^{L,T}(\tau) d\tau \quad (\text{II-16})$$

where t_0 is the time of integration. Finally, we search for the lower bound space-time window (\tilde{L}, \tilde{T}) of averaging above which $\Gamma(L, T)$ remains quasi constant, i.e. within less than 1% of change.

3.4 Results and conclusions

Figure II-3 shows the autocorrelation functions $\chi_{win}^{L,T}(\tau)$ computed for the winter dataset and for three different cases: when no mean field is removed, when the mean field calculated for $L=50$ km and $T=40$ days is removed, and when the mean field calculated for $L=400$ km and $T=160$ days is removed. When no mean field is removed from the original signal, the autocorrelation function never crosses zero and stabilizes around 0.05, i.e. a residual correlation persists after 20 days. This is the mark of the predictable character, in the deterministic sense, of the mean circulation. For spatial and temporal averaging scales below 400 km and 160 days respectively, the autocorrelation function shows negative values until approximately 20 days. This is due to the fact that for these averaging scales we artificially include in the computed mean field some spatial and temporal variability that is not deterministic, i.e. a random part of the motion. Doing so, we remove this variability from the fluctuating velocity field and then we bias the associated autocorrelation function. For spatial and temporal averaging scales larger than 400 km and 160 days, the autocorrelation function stabilizes, as expected. However, using such averaging scales, one would loose information about the details of the mean circulation.

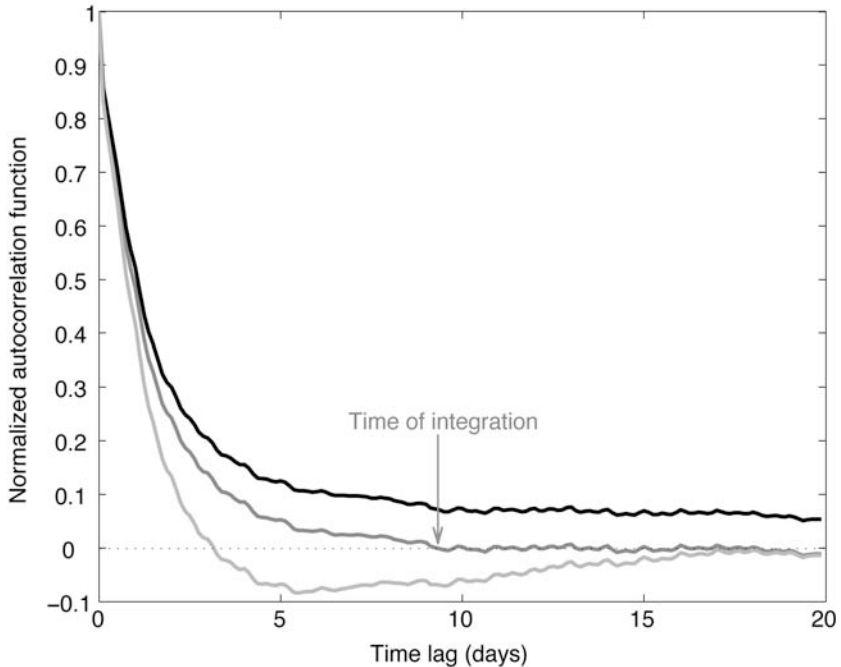


Figure II-3. Normalized autocorrelation functions of fluctuating velocity. The fluctuating velocities are calculated after the remove of a mean velocity field estimated for different averaging spatial and temporal scales: no mean flow is removed (in dark), the removed mean velocity field is computed for $L=50$ km and $T=40$ days (in light grey), and for $L=400$ km and $T=160$ days (in dark grey). We can define the time of integration for the two last cases as the time of the first zero crossing.

We show on figure II-4 the Γ -values deduced from the autocorrelation functions $\chi_{win}^{L,T}(\tau)$. For scales under 400 km and 160 days, the Γ -value increases strongly (i.e. from 0.6 to 1.4) with increasing averaging scales. Above these lower bounds, the function $\Gamma_{win}(L,T)$ reaches a plateau around 1.5 days (the relative variation of Γ is lower than 1%). This is the confirmation of what we deduced from the analysis of the autocorrelation functions.

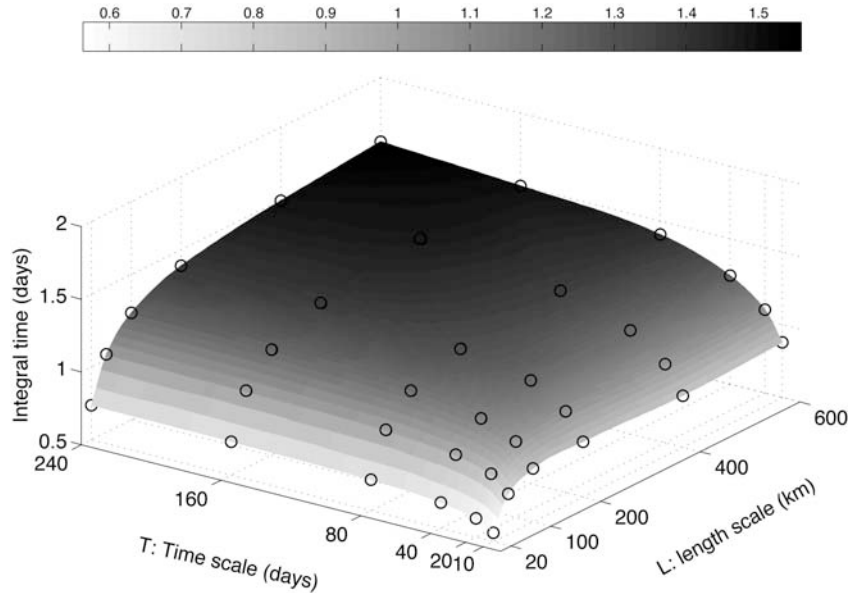


Figure II-4. Integral time scale (i.e. Lagrangian time of correlation) for sea ice in winter versus the spatial and temporal scales for which the removed mean flow is estimated. These results are for the winter dataset. The integral time is estimated from the Lagrangian autocorrelation functions by integrating them between $t=0$ and the time of integration t_0 . The estimated integral times are drawn as light grey circles. The filled surface is the interpolated surface of the data. We can note that this surface shows a plateau for scales larger than 400 km and 160 days. At these scales the integral time is about 1.5 days. At larger scales, the estimated integral times remain stable.

Thus, we conclude that the appropriate averaging scales to compute the AMGC are $\tilde{L}_{win}=400$ km and $\tilde{T}_{win}=160$ days, i.e. approximately one winter in the polar season. For summer, we find that (i) the function $\Gamma_{sum}(L,T)$ reaches a plateau around 1.3 days and (ii) the appropriate averaging scales are $\tilde{L}_{sum}=200$ km and $\tilde{T}_{sum}=80$ days, i.e. approximately one summer in the polar season. As a comparison, *Colony and Thorndike* [1984] and *Thorndike* [1986a] estimated the integral time scale of sea ice motion from 28 trajectories of buoys that drifted in the Arctic basin during winter and/or summer, computing the time autocorrelation function for x and y components of the total velocity (i.e. without any mean removed), and they found a value around 5 days. This much larger value than the one we found illustrates the bias on the Lagrangian

statistics that is obtained if no mean velocity is removed before the analysis, i.e. if the predictable part of the motion is kept. This points out the fact that it is crucial to (i) estimate unambiguously and (ii) remove the mean velocity field in order to estimate correctly the properties of the fluctuation velocity field.

3.5 Discussion

To illustrate what such mean fields look like, we compute the mean velocity fields for the winters 1992/93 and 2000/01 and the following summers (i.e. the summers 1993 and 2001 respectively). These mean fields are interpolated on a regular grid of 400km and 200km respectively, following the appropriate averaging scales (see figure II-5). We computed the errors $\Delta\bar{u}$ on the mean speed estimates \bar{u} using the central limit theorem, considering independent speed values. Two speed values are independent if (i) they are recorded by two different buoys separated by a distance $l \geq \Lambda$ (i.e. the integral length), or (ii) if they are recorded by the same buoy with a time lag larger than Γ (i.e. the integral time). These errors range from 4 to 25% for winter, and from 6 to 33% for summer. We can note here that despite the apparent large scales of average, these mean fields contain exhaustive information on the predictable part of sea ice motion. On the winter 1992-93 mean field map (Figure II-5a), we can identify the Beaufort Gyre and the Transpolar Current, i.e. the same structures that *Colony and Thorndike* [1984] found by averaging over 90 years. However, an average over 90 years induces a loss of information about the inter-annual variability of the AMGC. This is confirmed by a look on the winter 2000-01 mean field map (Figure II-5b), where the mean field shows a different pattern: the centre of the gyre is shifted though the West and the Transpolar Current appears less clearly. This inter-annual variability is illustrated on figure II-5c on which the difference between both winter mean fields is plotted. This plot shows that the difference in the velocity magnitudes can reach 4 cm/s in the Transpolar Current region, i.e. a value of the same order than typical velocity magnitudes observed for each winter. The mean speeds reached up to 6.8 cm/s in the Fram Strait for the winter 1992-93 while these never exceed 5 cm/s for the winter 2000-01. Almost null values are observed in the centre of the Beaufort Gyre for both winters. On the summer 1993 mean field map (Figure II-5d), the circulation draws a quite different picture compared to the previous winter (i.e. winter 1992-93). Along with the Transpolar Drift, two independent gyres are revealed: the first one is a clockwise gyre centered on the north of the Beaufort basin and the second is an anti-clockwise gyre centered on the Laptev Sea. During this particular summer, the mean speeds reached up to 7.5 cm/s. Like for winters, the mean field of summer 2001 shows a different pattern than the one of 1993: The direction of rotation of the gyre changed to anti-clockwise. Its centre is shifted to the West, and is now located near the Transpolar Current region. The strong inter-annual variability of the velocity mean field for summer is illustrated on figure II-5f. Very strong differences in the velocity magnitudes are observed and range up to 7.8 cm/s. We also checked that the only perennial structure in the AMGC from one year to another is the Transpolar Drift.

Thus, we can say that the strong seasonal and interannual variability of the mean velocity field of sea ice is well illustrated by the example presented above. One could associate this variability to a change in the forcing, as atmospheric and/or oceanic conditions are known to change significantly from winter to summer, and from one year to another [Thorndike and Colony, 1982; Hurrel, 1995; Thompson and Wallace, 1998; Rigor et al., 2000; Overland et al., 2004; Deser and Teng, 2008]. It is worth noting here that this interannual variability has nothing to do with the stochastic fluctuations of the remaining part of the sea ice motion.

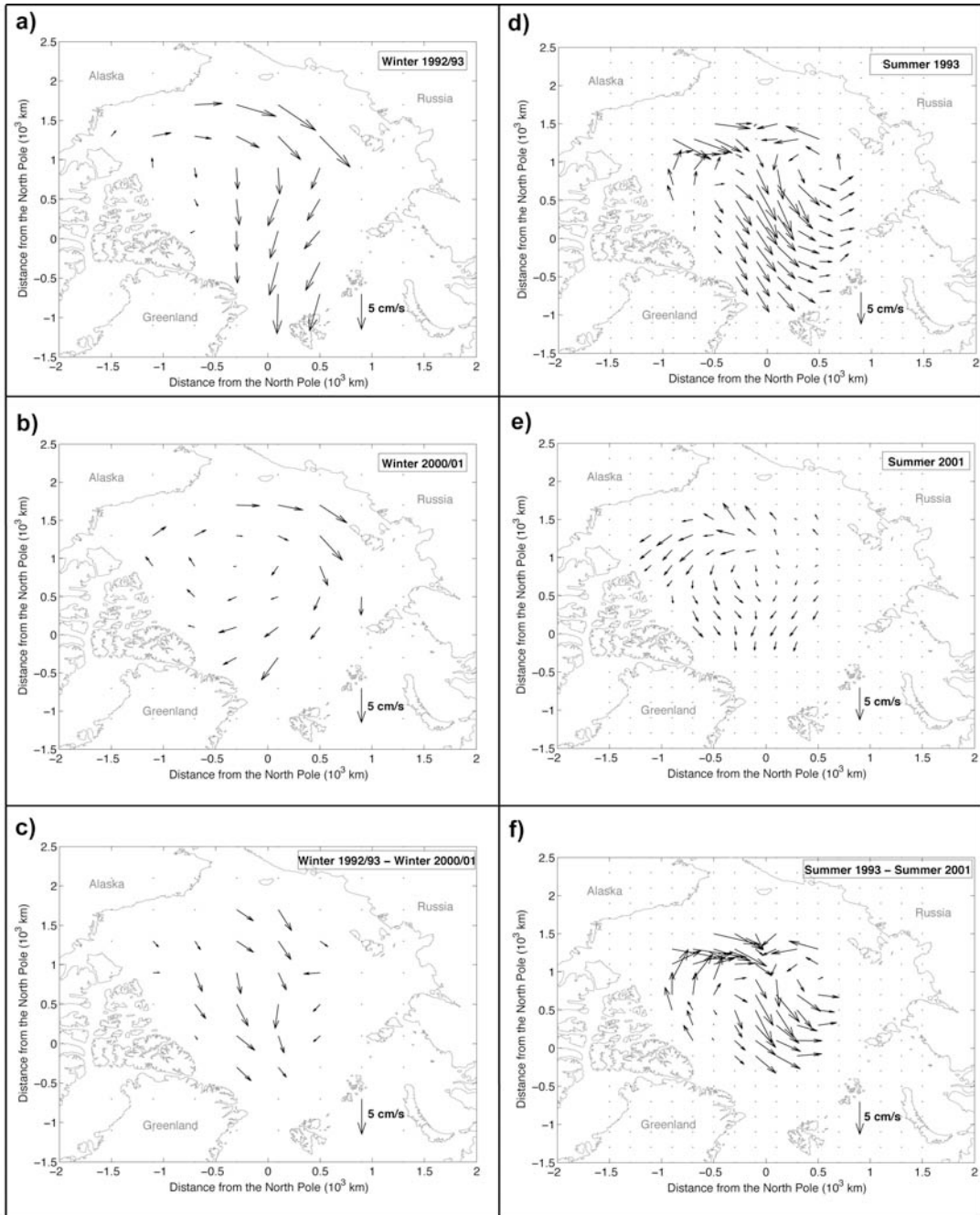


Figure II-5. : Interpolated mean velocity field for winter 1992-93 (a), winter 2000-01 (b), the difference between both winters (c), summer 1993 (d), summer 2001 (e), and the difference between both summers (f). The mean fields are calculated for averaging scales of 400 km and 160 days for winters, and for averaging scales of 200 km and 80 days for summers. These maps illustrate the seasonal and inter-annual variability of the AMGC. The maps (c) and (f) point out the fact that these variations are of the same order of magnitude than the speeds of the calculated mean velocities.

4. Analyzing the fluctuating velocity field of Arctic sea ice

Once a correct estimation of the mean velocity field of the Arctic sea ice is obtained, an analysis of the fluctuations can be performed. In what follows, we will discuss about the fluctuations of sea ice velocity estimated at the appropriate scales \tilde{L} and \tilde{T} established in section 3 (i.e. 400 km and 160 days for winter, and 200 km and 80 days for summer). In addition to the primary results of section II-3, we investigate here other statistical properties of the sea ice velocity fluctuations and we compare them with those predicted by the turbulent diffusion theory of *Taylor* [1921].

In subsection 4.1, we perform a spectral analysis of the fluctuating velocity \mathbf{u}' . In subsection 4.2, we compare the statistics of the fluctuating speed u' with those predicted by the turbulent diffusion theory of *Taylor* (1921) for a steady and homogeneous turbulent flow. In subsection 4.3, we analyze the distributions of the velocity increments. The subsection 4.4 presents the diffusion regimes of sea ice. We discuss these results in subsection 4.5.

4.1 Spectral analysis

Let us come back first on the autocorrelation function $\tilde{\chi}(\tau)$ defined as (II-15), focusing first on the winter season. We checked that it decreases as an exponential $\rho(\tau) \sim e^{-\tau/\tilde{\Gamma}}$, with $\tilde{\Gamma} \approx 1.5$ days (see figure II-6). The exponential reproduces extremely well the variation of the autocorrelation function, from the smallest time scales explored in our analysis (i.e. 3 hours) to $5 \tilde{\Gamma}$ (see inset of figure II-6).

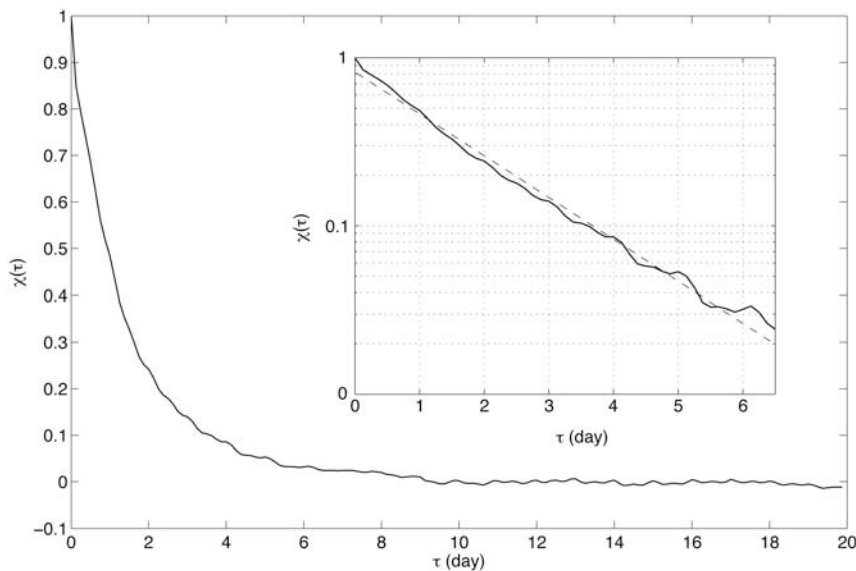


Figure II-6. Averaged autocorrelation function of the sea ice fluctuating velocity for winter. The inset plot shows the range where the autocorrelation function can be modeled by an exponential decay.

Note that, as the variance of the autocorrelation function must be defined [Voth *et al.*, 1998], there has to be some lower cut-off to this behavior at time $\tau_n \ll 3$ hours [Sawford, 1991]. τ_n would be then for the sea ice motion a kind of turbulent-like dissipative scale. This point would be a subject for future investigations, requiring sea ice velocity measurements with much better spatial as well as temporal accuracy.

We then turn to the Lagrangian spectrum, i.e. the power spectrum in time of the sea ice velocity fluctuations. By computing the Fourier transform of the exponential decay of the autocorrelation function, one gets:

$$P(k) \sim \frac{\tilde{\Gamma}}{1 + (k\tilde{\Gamma})^2} \quad (\text{II-17})$$

where $P(k)$ is the power spectral density function. $P(k)$ is computed as follows:

$$P(k) = \frac{\left| \sum_{n=0}^{N-1} w(n) \tilde{\chi}(n) e^{-i 2\pi k n} \right|^2}{\sum_{n=0}^{N-1} (w(n))^2} \quad (\text{II-18})$$

where $w(n)$ is the rectangular function defined as $w(n)=1$ for $0 \leq n \leq N-1$ and $w(n)=0$ otherwise. $P(k)$ is shown on figure II-7. For both winter and summer we observe a clear range of power law scaling $P(k) \sim k^{-2}$. Departure from the k^{-2} scaling is observed at low frequencies in agreement with the exponential decay of the auto-correlation. At high frequencies, the spectrum deviates from the k^{-2} scaling as the consequence of aliasing effects.

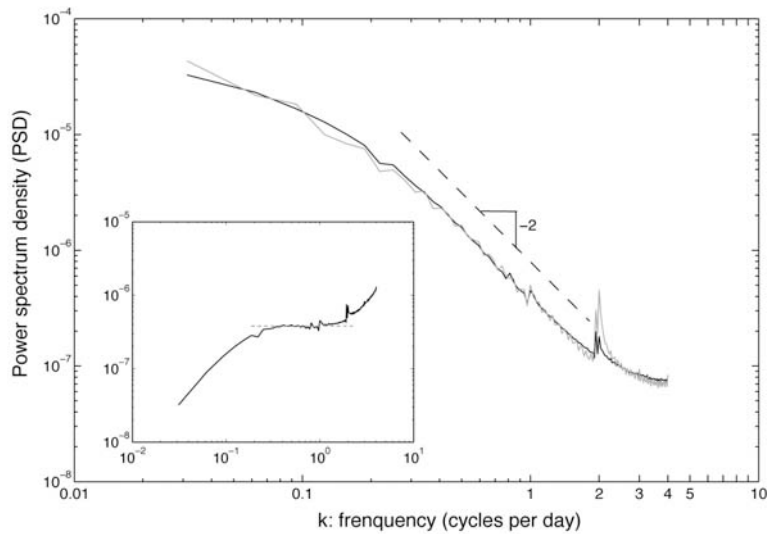


Figure II-7. Power spectrum of the velocity fluctuations for winter (in black) and summer (in grey) in a log-log scale. The dashed line is for reference only and corresponds to the regime expected for a turbulent fluid by the K41 theory in the inertial subrange (i.e. for fully developed turbulence). The inset shows the power spectrum of winter compensated by a k^{-2} scaling: the plateau corresponds to the region of

As a comparison with fluid turbulence, we note that such k^{-2} scaling coincides for example with the Kolmogorov K41 theoretical picture in which the spectral density at a frequency k is a dimensional function of k and of the dissipative rate of kinetic energy ε as $P(k) \propto \varepsilon k^{-2}$. Such k^{-2} scaling was reported for oceanic turbulence [Lien et al., 1998] and atmospheric turbulence [Gifford, 1955; Hay and Pasquill, 1959; Hanna, 1980] in the Lagrangian framework. We also

note that the k^{-2} scaling is the translation of the $k^{-5/3}$ scaling that holds for fluid turbulence in the Eulerian framework.

We can also observe on figure II-7 that a characteristic frequency of about 2 cycles per day (i.e. a time period of 12 hours) is clearly marked by a peak in the power spectrums of both seasons. This peak was observed from similar analysis of the total sea ice velocity signal and was viewed as inertial oscillations of period $T = 1/(2\omega \sin(\lambda))$ where λ is the latitude [Hunkins, 1967; McPhee, 1989; Colony and Thorndike, 1980; Thorndike, 1986a; Heil et al., 2002]. These inertial motions are related to the surface currents of the Arctic Ocean [McPhee, 1978]. Unlike the others signatures discussed in this section, this inertial motion does not have to be included in the random part of the sea ice motion. In other words, the sea ice motion resulting from the oceanic inertial oscillations is predictable in a deterministic sense. Figure II-7 shows that the peak is stronger in summer than in winter. This difference at the inertial frequency could be explained by the greater percentage of open water during the summer. In summer, the motion of the less-consolidated sea ice cover is closer to the free drift hypothesis and therefore better follows the motion of the underlying ocean. We note however that in both cases (winter and summer), this inertial motion is not strong enough to be detectable directly from the autocorrelation function (Figure II-2).

4.2 Distributions of fluctuating velocity

We plotted for both seasons the probability density functions (PDFs) of x and y components of the fluctuating velocity \mathbf{u}' , noted u_x' and u_y' respectively (see figure II-8). The distributions of u_x' and u_y' are symmetric and centered on zero. The symmetry and the superposition of both components reflect the isotropic character of the fluctuating velocity field (see figure II-2 and subsection 3.2). No strong differences are observed between winter and summer. Maximum fluctuating speeds are approximately 1 m/s, i.e. two orders of magnitude larger than the speeds of the AMGC. We also checked that the distributions of u_x and u_y are neither symmetric nor centered on zero: we can interpret this as the fingerprint of the AMGC (e.g. the Transpolar Current can explain the negative mean-value of the distributions of u_y). Thus, the symmetry of the PDFs of u_x' and u_y' confirms that the AGCM is correctly removed by averaging at the scales \tilde{L} and \tilde{T} . It is also in agreement with that we would obtain for fluctuating velocities in a pure turbulent flow [Taylor, 1921].

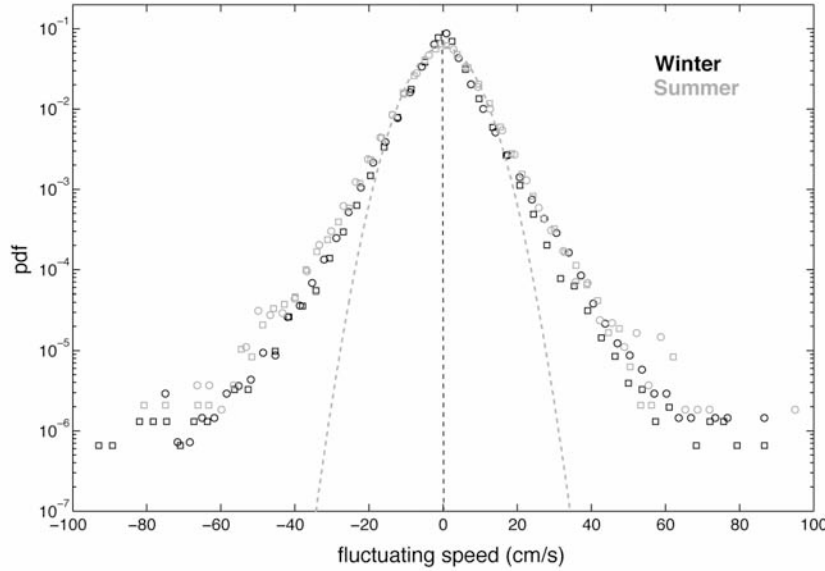


Figure II-8. Probability density functions for the x and y components u_x' (circles) and u_y' (squares) of the fluctuating velocity vector \mathbf{u}' , and obtained after removing the mean flow estimated at scales of 400 km and 160 days for winter (in dark) and at scales of 200 km and 80 days for summer (in grey). The means of the distributions are -0.05 cm/s (u_x') and 0.01 cm/s (u_y') for winter, and are -0.01 cm/s (u_x') and 0.09 cm/s (u_y') for summer. The shapes of the PDFs are symmetrical and the symmetry axis is drawn as a dashed line. The Gaussian distribution corresponding to the winter's data (i.e. with mean and standard deviation equals to those of the distributions of u_x' and u_y' merged) is plotted as the grey dashed line.

However, our statistics deviate from this theory in the following way: We show on figure II-9 the PDF of the norm of \mathbf{u}' defined as $u' = (u_x'^2 + u_y'^2)^{1/2}$, merging the winter and summer speed-values. The data follow an exponential distribution instead of the Gaussian distribution expected in fully developed turbulence [Batchelor, 1960; Frisch, 1995] and observed in different turbulent fluids [Van Atta and Chen, 1970; Zhang et al., 2001], i.e. authorizes much larger fluctuating speeds. We also checked that the distributions of both components of the total velocity \mathbf{u} are exponential as well (not shown here), and interpreted as the fingerprint of the fluctuations statistics. A great challenge would be to understand the origin of this difference from turbulent flows statistics. We will discuss further this point in section 5.

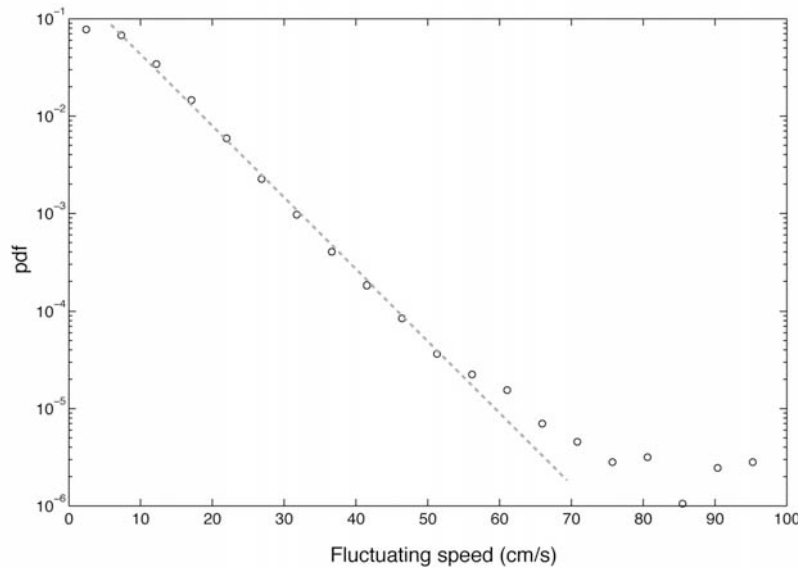


Figure II-9. Pdf of the fluctuating speed $u' = (u_x'^2 + u_y'^2)^{1/2}$ for the winter and summer datasets merged. The best exponential fit of the data is drawn as the grey dashed line. The slope of the exponential function allows us to estimate a characteristic speed of about 7.4 cm/s, i.e. very closed to the mean-value of the distribution that is about 7.8 cm/s. The few outliers above 60 cm/s can explain this small difference.

In conclusion, we show that the fluctuating part of sea ice velocity is characterized by zero means, symmetrical exponential distributions.

4.3 Intermittency and scaling

In order to further characterize the statistics of the Lagrangian velocity fluctuations, one must turn to higher order statistics of the velocity increments $\Delta_\tau \mathbf{u}$, where τ is the time scale over which the increments are computed. Here, we focus our analysis on the winter season. Figure II-10 shows the PDFs of $\Delta_\tau u_x$ and $\Delta_\tau u_y$ of the winter velocities for different values of τ .

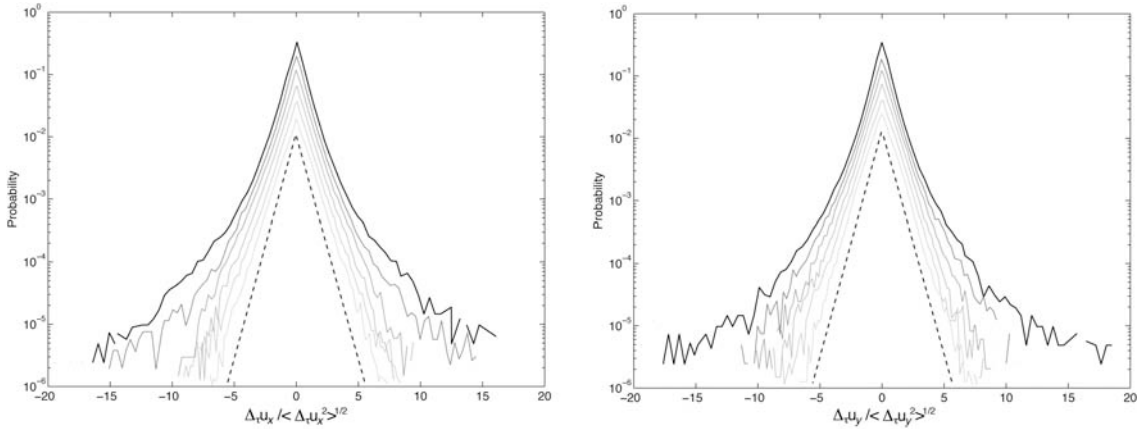


Figure II-10. PDFs of the normalized increment $\Delta_\tau u / \sigma_\tau$ for the two components of the velocity vector \mathbf{u} . The curves are shifted for clarity. From top to bottom: $\tau = [0.125, 0.25, 0.5, 1, 2, 5]$ days. The dashed lines show an exponential decay and are for reference only.

The PDFs are normalized to their unit variance in order to emphasize changes in the functional forms. We can see that the PDFs are symmetric about $\Delta u = 0$, in agreement with the local symmetries in the velocity field illustrated by the lack of skewness in the PDF of the lagrangian fluctuating velocity in winter (see figure II-8). At small τ (i.e. for $\tau = 3$ hours), the PDFs of both components show power law tails. These could be used to determine the PDF of the lagrangian acceleration, assumed to be approximately given by $(\Delta_\tau u / \tau)_{\tau \rightarrow 0}$ [Frisch, 1995]. At large τ (i.e. here for $\tau \geq 2$ days), the PDFs become exponential and stabilize. In between these extremes, the change is continuous. The time scale dependence of $\Delta_\tau u$ expresses the intermittency of the sea ice velocity signal.

In order to quantify this intermittency, we consider the variation of the PDFs of velocity increments with time scale in terms of the scaling of the velocity structure functions:

$$\langle |\Delta_\tau u|^q \rangle \sim \tau^{\xi(q)} \quad (\text{II-19})$$

In figure II-11, we plot the structure function $\langle |\Delta_\tau u_x|^q \rangle$ of u_x versus τ for $q=0.5$ to 3 by step of 0.5 along with the least squares dashed lines. A clear power law scaling (Equation II-19) is observed from $\tau = 3$ hours to $\tau \approx \tilde{\Gamma}$, i.e. the so-called inertial range for turbulent flows. This scaling does no longer hold for $\tau > \tilde{\Gamma}$, as expected [Mordant *et al.*, 2003]. We checked that similar results hold for u_y .

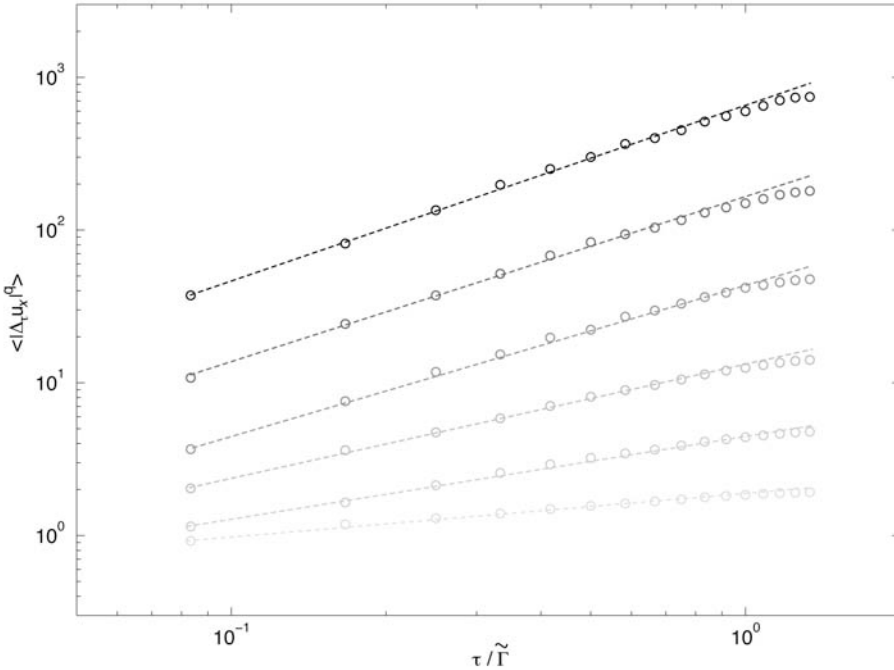


Figure II-11. Lagrangian structure functions of the x -component of the velocity for $q=0.5, 1, 1.5, 2, 2.5$ and 3 , for winter. The dashed lines are best linear fits with slope denoted $\zeta(q)$.

Then, the values of the slopes define the function $\zeta(q)$. From the k^{-2} scaling of the fluctuating velocity power spectrum (Figure II-7), we expect that the second order structure function scales as τ (see e.g. Mordant *et al.* [2003], Biferale *et al.*, [2006]). This is in agreement with our results since we obtain $\zeta(2)=0.95$. The function $\zeta(q)$ is shown on figure II-12. This later shows a curvature, indicating that the intermittent character of the sea ice velocity can be reproduced by the multifractal model. Indeed, $\zeta(q)$ is remarkably well approximated by a quadratic fit $f(q)=aq^2+bq$ with $a=-0.09$ and $b=0.65$. This indicates that the velocity fluctuations can be modeled by a log-normal multiplicative cascade process (see Yaglom [1966] for such a model in the case of 3D fully turbulence). While multifractality is a well-known property of turbulent flows

at high Reynolds numbers [Mordant *et al.*, 2003; Schmitt, 2006], it is observed here to also occurred for a solid, i.e. the Arctic sea ice.

$\Delta_\tau u / \tau$ can be interpreted as a rate of velocity change measured at time scale τ and has the dimension of an acceleration. The moments of this rate scale as

$$\left\langle \left(|\Delta_\tau u| / \tau \right)^q \right\rangle \sim \tau^{-(q-\zeta(q))} \sim \tau^{-\beta(q)} \quad (\text{II-20})$$

The function $\beta(q)$ is shown on figure II-12 along with its best quadratic fit. This indicates that the higher moments grow faster towards small time scales than for monofractal scaling, meaning that velocity changes are increasingly localized in time towards small scales.

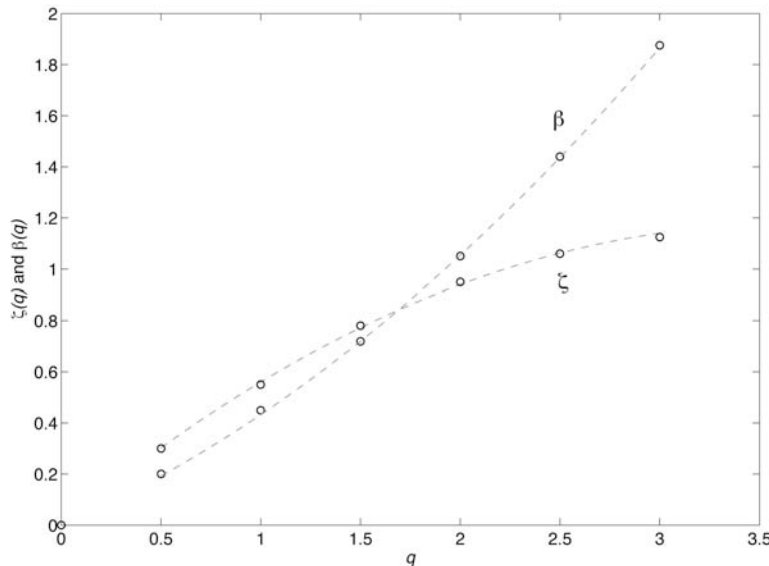


Figure II-12. Functions $\xi(q)$ and $\beta(q) = -(\xi(q) - q)$ versus moment order q (open circles) and the best-fit quadratic curves (dashed lines).

4.4 Diffusion regimes of sea ice

In subsection 3.1, we reminded that in the turbulent diffusion theory of *Taylor* (1921), the particle diffusion through time $\langle r'^2(t) \rangle$ has two asymptotic regimes (Equations II-6 & II-7). We check here whether these regimes remain for the Arctic sea ice. We computed the sea ice displacements r'_x and r'_y (along the x -axis and y -axis directions respectively) caused by the fluctuating velocity field of sea ice for winter and summer (see figure II-13).

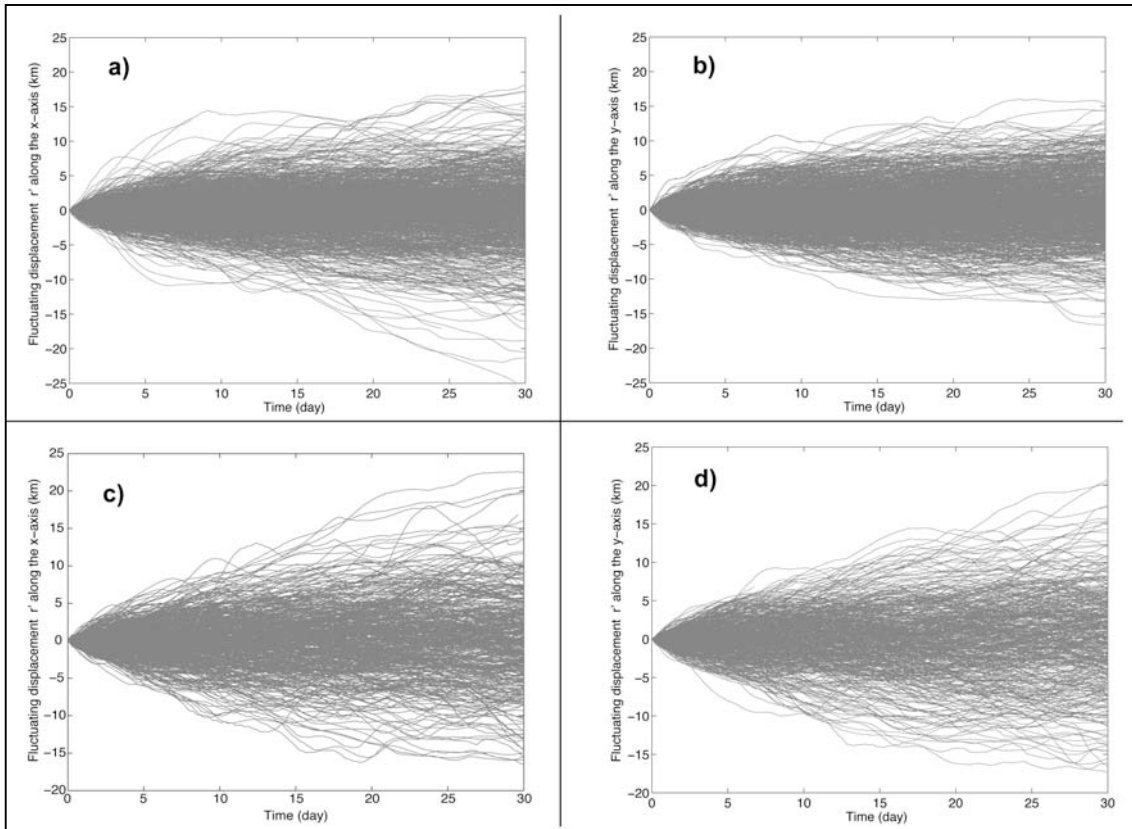


Figure II-13. Particle displacements r'_x (along x) and r'_y (along y) caused by the fluctuating velocity field for winter (a) and (b), and for summer (c) and (d). The fluctuating displacements are calculated from buoys tracks in which displacement associated with the mean flow is removed. After 30 days, fluctuating displacements are, on average, stronger in summer than in winter.

The symmetry about the zero line indicates once again the correct removal of the mean velocity structure; otherwise, they will be biased to one direction [Riser and Rossby, 1983]. The envelope of the drifter trajectories grows more quickly at the beginning and then slows down, qualitatively following the Taylor diffusion theory. To quantify this, we plot for winter and summer the variance of r' , defined as $\langle r'^2(t) \rangle = \langle r_x'^2(t) + r_y'^2(t) \rangle$, versus time on a log-log scale (see figure II-

14). We see that the fluctuating part of the sea ice motion follows the Taylor diffusion for both seasons and is consistent with our results presented in section 3 obtained by an analysis of the autocorrelation function: at time $t \ll \tilde{\Gamma}$ (around 1.5 and 1.3 days for winter and summer, respectively) the displacement variance grows with t^2 ; at $t \gg \tilde{\Gamma}$ (i.e. $t > 10$ days), it grows with t .

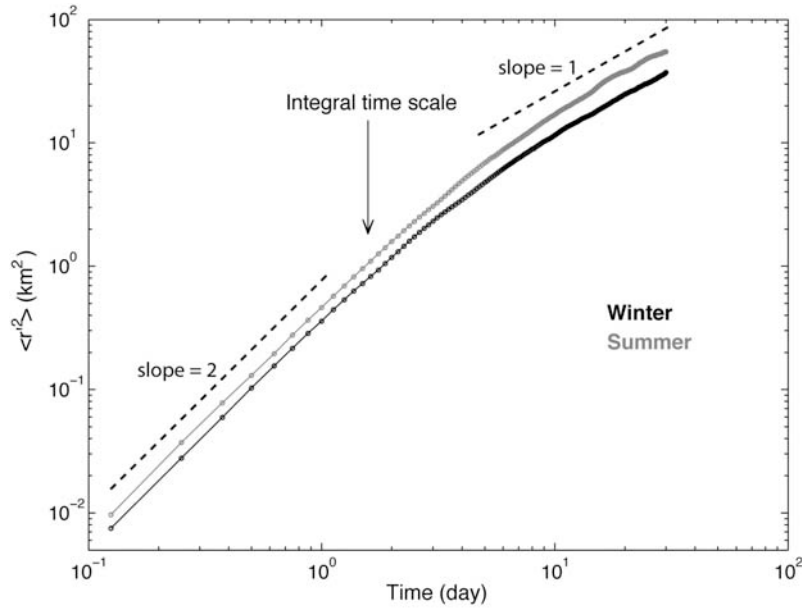


Figure II-14. Plot of the variance $\langle r'^2 \rangle$ of the fluctuating displacement r' versus time in log-log scale. The fluctuating displacement is defined as $r' = (r_x'^2 + r_y'^2)^{1/2}$. The dashed lines show the two regimes expected by the Taylor diffusion theory, i.e. for the initial ballistic regime ($t \ll \Gamma$) and long-time random walk ($t \gg \Gamma$). We also show in the plot the integral time value estimated previously from the lagrangian autocorrelation functions.

The regime where displacement variance grows with t was expected since we showed in subsection 4.2 that the distribution of the fluctuating speed of sea ice was exponential. Indeed, exponential distributions are in the Gaussian attractive basin (by addition of independent variables) [Bouchaud and Georges, 1990; Sornette, 2000] and then lead to the same diffusive regime for time larger than the integral time scale $\tilde{\Gamma}$.

We also computed a turbulent-like diffusivity of the Arctic sea ice following (II-10) for $t \gg \tau$. We found a diffusivity of about 0.44×10^3 m²/s for winter and about 0.45×10^3 m²/s for summer. These values lie in the range of diffusivities estimated for the surface of the open ocean (i.e. between 0.025 and 0.66×10^3 m²/s) [Colin de Verdière, 1983; Krauss and Böning, 1987; Poulain *et al.*, 1996].

We found in section 3 that the integral time Γ for sea ice is about 1.5 days in winter and 1.3 days in summer. For the ocean surface, Γ -values were reported by several studies in which analyzes of drifting buoys trajectories are performed [Colin de Verdière, 1983; Krauss and Käse, 1984; Davis, 1985; Krauss and Böning, 1987; Poulain and Niiler, 1989; Poulain et al., 1996]: Integral times range from 1 day to 4.5 days, depending on the location (i.e. near coasts, or in the open ocean), i.e. these estimates are of the same order of those obtained in this study. On the contrary, our estimates are five orders of magnitude larger than typical integral time estimated from Lagrangian velocities of neutral balloons moving in the boundary layer of the atmosphere at altitudes between 100 and 300 m [Hanna, 1980].

4.5 Discussion

In this section, we discuss the results of section 4 in terms of sea ice dynamics. The mechanic principle of Newton is commonly expressed for sea ice by the following simplified momentum equation:

$$m \frac{D\mathbf{u}_{ice}}{Dt} = \boldsymbol{\tau}_a + \boldsymbol{\tau}_w + \nabla \cdot \boldsymbol{\sigma} \quad (\text{II-21})$$

where D/Dt is the material derivate, $\boldsymbol{\tau}_a$ is the atmospheric drag defined as $\boldsymbol{\tau}_a = \rho_a C_a \mathbf{u}_a^2$, $\boldsymbol{\tau}_w$ is the oceanic drag defined as $\boldsymbol{\tau}_w = \rho_w C_w (\mathbf{u}_w - \mathbf{u}_{ice})^2$ and $\boldsymbol{\sigma}$ is the sea ice internal stress tensor. \mathbf{u}_a , \mathbf{u}_w and \mathbf{u}_{ice} are the velocities of wind, surface current and sea ice, respectively. In what follows, we discuss equation (II-21) from a statistical point of view, considering the distributions of scalar quantities, i.e. the two components of the velocity. The question is: which forcing term(s) can explain the statistical properties of the velocity field found in the previous sections of this paper.

The turbulent-like diffusion properties over sea ice show several similarities with ocean surface drifters:

- The inertial oscillation frequency appears in the velocity power spectrum
- The same diffusion regimes derived from the turbulent diffusion theory of *Taylor* [1921]
- Integral time and diffusivity of the same order of magnitude

This might suggest a free-drift, quasi-static regime as a rough but essentially correct approximation of sea ice drift (i.e. $\mathbf{u}_w = \mathbf{u}_{ice}$). However, we showed in subsection 4.2 that the distributions of sea ice speed are strongly different from those observed in the ocean, i.e. exponential instead of Gaussian. In other words, sea ice velocities are much more widely distributed than surface ocean velocities, thus invalidating this free-drift hypothesis, as intuitively expected at least for winter.

Sea ice motion is forced by winds and ocean currents, which exhibit themselves turbulent properties. One can therefore wonder to what extent the statistical properties of the ice velocity field are simply inherited from the forcing terms $\boldsymbol{\tau}_a$ and $\boldsymbol{\tau}_w$ of equation (II-21). This would mean to simply ignore in this later the internal stress term $\nabla \cdot \boldsymbol{\sigma}$. Like for ocean current velocities, the lagrangian statistics of wind velocities are Gaussian [*Van Atta and Chen*, 1970]. Therefore, \mathbf{u}_a^2 as well as the difference $(\mathbf{u}_w - \mathbf{u}_{ice})^2$ that are in the forcing terms are Lorentz distributions. On the other hand, we noted in section 4.3 that for $\tau \rightarrow 0$ the distributions of $\Delta_\tau u_x$ and $\Delta_\tau u_y$

approximate the distributions of both components of the sea ice acceleration (see figure II-10). So, we can say that the distributions of sea ice acceleration are characterized by power law tails. Consequently, the sea ice acceleration, i.e. the inertial term in the equation (II-21), cannot be explained solely by the summation of atmospheric and oceanic dynamic forcing.

In fact, the only term that underlies properties than can explain the sea ice velocity and acceleration statistics is the divergence of sea ice internal stress. As shown recently, most of the sea ice deformation is accommodated by a multiscale fracturing and faulting process [Weiss *et al.*, 2004, 2008b] leading to strong spatial heterogeneity and intermittency of strain rates [Marsan *et al.*, 2004; Rampal *et al.*, 2008] and stresses [Weiss *et Marsan*, 2004]. Intermittency of internal stress amplitudes [Weiss *et Marsan*, 2004] and principal stress directions [Weiss, 2008a] were revealed from multifractal analysis. The intermittency of principal stress directions within sea ice is much more pronounced than that of wind direction. The similarity between the intermittency of stress amplitudes in one hand, and sea ice acceleration in the other hand, suggests that the internal stress term plays a significant role in the statistical properties of sea ice kinematics and dynamics in winter.

5. Conclusions

The main conclusions of this study are:

- (i) The Arctic sea ice velocity field can be partitioned into a mean field and a fluctuating field using an original approach inspired from the study of fluid turbulence. In order to study the fluctuating velocity field, one has to consider separately the both seasons and subtract from the total velocity field a mean field estimated at averaging scales of about $L=400$ km and $T=5 \frac{1}{2}$ months in winter, or $L=200$ km and $T=2 \frac{1}{2}$ months in summer.
- (ii) Estimated at these scales, the seasonal mean field shows a strong interannual variability, excepting the Transpolar current that can be observed all years long.
- (iii) Once extracted from the total velocity field, the fluctuating field can be studied within the framework of the turbulent diffusion theory of *Taylor* [1921]. Performing an analysis of the fluctuating velocity field properties, we show that sea ice diffusion follows the same diffusive regimes than those of turbulent flows, and that the integral time and diffusivity of sea ice are of the same orders than those of the upper ocean.
- (iv) On the other hand, the fluctuating speed distributions of both velocity components differ from those of homogenous and isotropic turbulence as they show an exponential decay.
- (v) The analysis of sea ice velocity increments reveals a multifractal scaling, expressing the intermittency of sea ice velocity.
- (vi) The oceanic and atmospheric dynamic forcing cannot explain solely the statistical properties of sea ice kinematics and dynamics. We argue that sea ice dynamic is significantly influenced by the interplay of multiple fractures that are activated intermittently within the ice pack.

Acknowledgements We thank I. Rigor from the Polar Science Centre of Seattle and O. Persson from the Earth Observing Laboratory of the NCAR for the compilation and the distribution on the web of the IABP dataset and the wind speed dataset of SHEBA respectively.

Chapitre II

Champ de vitesse de la banquise Arctique

Chapitre III :

Champ de déformation de la banquise Arctique

D'après:

Ram pal, P., J. Weiss, D. Marsan, R. Lindsay and H. Stern (2008), Scaling properties of sea ice deformation from buoy dispersion analysis, *J. Geophys. Res.*, 113, C03002, doi:10.1029/2007JC004143.

Abstract:

A temporal and spatial scaling analysis of Arctic sea ice deformation is performed over time scales from 3 hours to 3 months and over spatial scales from 300 m to 300 km. The deformation is derived from the dispersion of pairs of drifting buoys, using the IABP (International Arctic Buoy Program) buoy data sets. This study characterizes the deformation of a very large solid plate -the Arctic sea ice cover- stressed by heterogeneous forcing terms like winds and ocean currents. It shows that the sea ice deformation rate depends on the scales of observation following specific space and time scaling laws. These scaling properties share similarities with those observed for turbulent fluids, especially for the ocean and the atmosphere. However, in our case, the time scaling exponent depends on the spatial scale, and the spatial exponent on the temporal scale, which implies a time/space coupling. An analysis of the exponent values shows that Arctic sea ice deformation is very heterogeneous and intermittent whatever the scales, i.e. it cannot be considered as viscous-like, even at very large time and/or spatial scales. Instead, it suggests a deformation accommodated by a multi-scale fracturing/faulting processes.

1. Introduction

The Arctic sea ice cover is a deforming solid, which extends during winter over about 14 million km, with an average thickness of a few meters. Consequently, it can be considered, from a mechanical point of view, as a two dimensional plate (plane stress conditions are fulfilled). This plate deforms under various stresses, mainly from winds and ocean currents [*Thorndike and Colony*, 1982]. This leads to the fracturing and faulting of the sea ice cover. The overall sea ice deformation, along with thermodynamics, controls the amount of open water as well as the ice thickness distribution: divergent deformation is associated with crack opening and new ice growth, whereas convergent deformation causes ice to pile up and ridges to form. Sea ice deformation is important for understanding the momentum, mass, and energy balance in the Arctic and more generally the influence of Arctic dynamics on the Earth's climate. Fracturing and divergence of the ice cover decreases the albedo and allows more shortwave absorption by the ocean, thereby shrinking the ice cover during summer, and possibly reducing its strength and increasing the fracturing [*Zhang*, 2000; *Moritz*, 2002] and the faulting [*Kwok*, 2001; *Kwok*, 2006]. On the other hand, fracturing during winter enhances the thermodynamically driven production of new ice and consequently modifies the heat and salinity budget in the Arctic Ocean [*Maykut*, 1982]. These complex processes are highly non-linear. As an example, in an ice cover fractured with 0.5% of open water leads, 50% of the thermal energy lost from the ocean occurs along these leads [*Heil*, 2002]. In what follows, we used the term "fracturing" in a generic sense. I.e., it refers to tensile fracturing (opening mode) as well as to shear faulting indifferently.

Sea ice dynamics models implemented in climate models are based on a continuum mechanics modeling framework initially developed by *Hibler* [1979], and share a common viscous-plastic (VP) or elastic-viscous-plastic (EVP [*Hunke and Dukowicz*, 1997]) rheology. This rheology implies that for stress states inside the plastic yield curve, sea ice behaves as a viscous fluid (with an additional linear elastic component for EVP rheology), while ice flows as a perfect plastic when the stress state reaches the envelope, without further increase of the stress. This viscous flow is considered to result from the average effect of many "plastic" events [*Hibler*, 1977], and as such relies on a hypothesis that the stress and strain are locally homogeneous or smoothly varying. This framework has been widely used, as it is suited for a numerical coupling with other fluid layers (ocean, atmosphere), and because of the development of efficient methods to solve the momentum equation employing this rheology [*Zhang*, 2000]. By construction, it homogenizes the sea ice properties at the discretization scale, and therefore ignores possible sub-grid scale variability.

Recent analyses of deformation and fracturing fields over the Arctic sea ice cover challenged this classical modeling framework in two ways: the viscous-plastic rheology assumption and the homogeneous stress and strain assumption. A detailed analysis of in-situ ice stresses and satellite-derived strain-rates showed that stress states are indeed confined in an envelope with Coulombic branches, but its size is rate- and scale-dependent [Weiss *et al.*, 2007]. Moreover, no correlation was observed between stress and strain-rate, in contradiction to a viscous behavior. A multifractal analysis of strain-rate fields obtained from RGPS (Radarsat Geophysical Processor System [Kwok, 1998]) demonstrated the highly heterogeneous, scale-free character of sea ice deformation [Marsan *et al.*, 2004], therefore raising doubts about the homogeneous assumption used in sea ice models. Similarly, in-situ ice stress records are highly intermittent and scale-invariant in time [Weiss *et al.*, 2004]. All these observations argue for an elasto-brittle behavior of the sea ice cover, as suggested by Nye [1973], with a deformation accommodated by multiple fractures and faults at various scales. However, these recent analyses had limitations: RGPS has a limited time resolution of about 3 days, and in-situ ice stress data are local and not necessarily representative of the large areas. A comprehensive scaling analysis of sea ice deformation, covering a wide range of both time and spatial scales is therefore needed.

In this paper, we describe the fracturing and faulting of the ice in terms of deformation. We show the time and spatial scale invariance properties of sea ice deformation, improving the time and spatial ranges of analysis compared to previous studies. The resulting scaling laws and associated exponents are guidelines for understanding the underlying physics of the mechanisms of sea ice deformation and dynamics.

The consequence of sea ice fracturing and faulting is that, like two particles in a gas or two people in a crowd, two nearby pieces of sea ice gradually move apart and disperse [Martin and Thorndike, 1985]. Thus, to study the dispersion of sea ice is a way to analyze its deformation. Considering two pieces of sea ice, each of them holding a buoy capable of reporting its position through time, we can analyze the dispersion of sea ice in terms of the changes in separation between this pair of buoys. This idea was first proposed and applied to Arctic sea ice by Martin and Thorndike [1985]. Their study revealed, in a statistical sense, similarities between the dispersion properties of sea ice and the dispersion of particles in turbulent fluids, even if we expect that the underlying physics is not the same. The dispersion process is a phenomenon that has been defined and studied for a long time for turbulent fluids. Rather than following buoys fixed to the sea ice, these studies of fluids followed colored tracers in gases or liquids, balloons in the atmosphere, or buoys at the surface of the ocean [Richardson, 1949; Batchelor, 1951; Okubo, 1977; Morel *et al.* 1974; Martins *et al.*, 2002; Zhang *et al.*, 2001; Jullien *et al.*, 1999]. In this paper, we follow the idea

initially proposed by *Martin and Thorndike* [1985], with a much larger data set, representative of the entire Arctic Ocean. To study sea ice deformation, we follow a methodology inspired from the analysis of fluid turbulence, and particularly the analysis of oceanic and atmospheric turbulence, which provide two main forcing terms of sea ice dynamics. Similarities and differences between sea ice dynamics and fluid turbulence are stressed to understand the coupling between the different layers of the system and the nature of sea ice deformation.

2. Dataset

The data set, provided by the International Arctic Buoy Program (<http://iabp.apl.washington.edu/data.html>), consists of trajectories of drifting buoys that were deployed in the Arctic between 1979 and 2001. A total of approximately 500 drifting buoys were installed over the entire Arctic basin during this period. The buoys are fixed on the ice and then drift according to the ice motion. Buoys trajectories plotted in figure III-1 clearly show that our dataset is representative of the whole Arctic basin Ocean. However the lifetime of each buoy is variable, from a few days to many months. We only kept the positions contained in the Arctic basin, above the bold arc drawn on figure III-1.

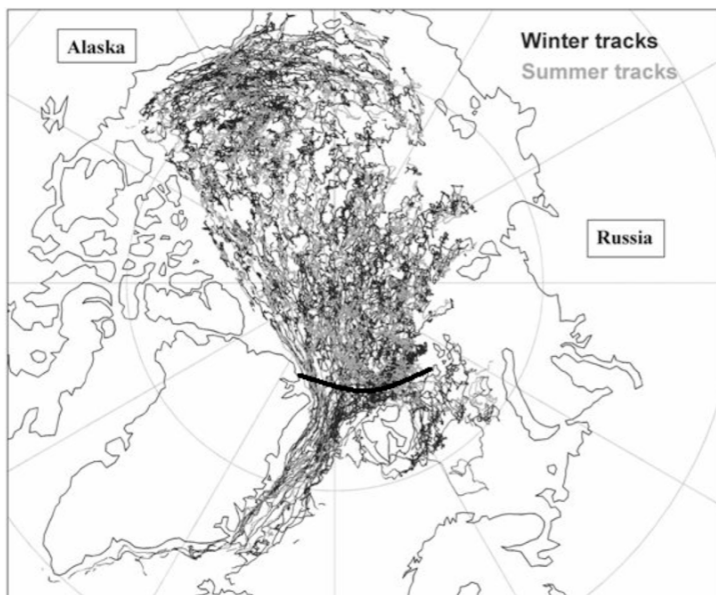


Figure III-1. Map of the Arctic basin showing approximately 500 buoy tracks from the IABP (International Arctic Buoy Program) dataset, recorded between 1979 and 2002. The bold arc represents the lower geographical limit of the data used in our analysis.

We worked more specifically on pairs of simultaneously active buoys, approximately 680 pairs, or 500000 3-hourly geographical positions obtained between 1979 and 2001: 70 % were recorded in winter (i.e. from mid-September to mid-June) and the remainder in summer. The average sampling rate of the raw data was 1 position per hour. The raw data were post-processed by the IABP by determining a cubic interpolation of the geographical positions and then re-sampling the interpolated trajectories at 3-hour intervals. Buoys that rely on the ARGOS system for position estimates have a position uncertainty of about 100 to 300 m (depending on the measurement quality), while those that use GPS have an uncertainty of about 100 m.

In their analysis of buoy dispersion, *Martin and Thorndike* [1985] used a similar, although much smaller, dataset. It consisted of two sets, each of about a dozen drifting buoys, which were launched in the Bering and Beaufort Seas in the winter, and which recorded their positions during several days with a sampling rate of 1 position per hour. They analyzed the dispersion within the scale ranges of 1 hour to 4 days, and from a few km to 60 km.

As another point of comparison, *Marsan et al.* [2004] used the RGPS data that is derived from synthetic aperture radar (SAR) images. These images are used to track the trajectories of about 40000 points over the entire Arctic for periods of up to 6 months. The points are initially spaced 10 km apart and are organized into four-cornered cells. From these trajectories, the strain-rates can be calculated over each cell, at an average sampling interval of 3 days. This allows analysis of the scaling of sea ice deformation from 10 km to 1000 km, at the time scale of 3 days. This time scale represents a limitation of the RGPS data set for scaling analyses [*Marsan et al.*, 2004].

Compared to these former analyses, our dataset presents (i) a much greater spatial coverage and statistical representation, as well as larger temporal and spatial ranges than the *Martin and Thorndike* [1985] data set and, (ii) a much better time resolution than the RGPS data set, allowing small time scales to be explored.

3. Methodology

The dispersion of pairs of buoys can be linked to sea ice cover deformation using an approach based on the methodology developed by Richardson for turbulent flows [Richardson and Stommel, 1949; Martin and Thorndike, 1985]. We study how the dispersion of pairs of buoys depends on both (i) their initial separation L , and (ii) the time τ during they dispersed. In figure III-2, two buoys A and B with absolute positions \mathbf{x}_1 and \mathbf{x}_2 respectively, and with separation $\mathbf{y} = \mathbf{x}_2 - \mathbf{x}_1$, are considered. If these two buoys initially separated by $L = \|\mathbf{y}(0)\|$ are observed after a time $t = \tau$, a change in separation is observed. Our notations are: $\mathbf{y}(0)$ has magnitude L and $\mathbf{y}(\tau)$ has magnitude $l(\tau)$. We define the change in separation Δr as:

$$\Delta r(\tau) = \|\mathbf{y}(\tau)\| - \|\mathbf{y}(0)\| = l(\tau) - L \quad (\text{III-1})$$

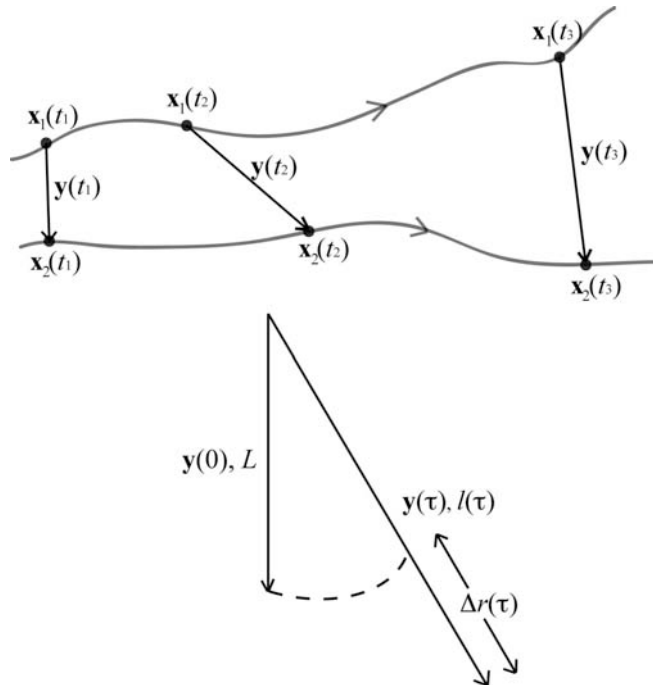


Figure III-2. Notations. For a pair of buoys located at $\mathbf{x}_1, \mathbf{x}_2$, the separation $\mathbf{y} = \mathbf{x}_2 - \mathbf{x}_1$ yields the dispersion $\Delta r = \|\mathbf{y}(\tau)\| - \|\mathbf{y}(0)\|$ at time τ .

In fluid mechanics, the dispersion process is characterized by the mean square change in separation $\langle \Delta r^2 \rangle$. Except for section III-4, this variable is not considered here. From a solid mechanics perspective, it appears more pertinent to consider the rate $\dot{D} = \Delta r / L\tau$ instead of the

change in separation Δr . \dot{D} is analogous to a deformation rate, measured in day⁻¹. Neither Δr nor \dot{D} are sensitive to solid rotations. They only quantify the deformation due to divergence, convergence, and/or shear. They only quantify the deformation due to divergence, convergence, and/or shear. However, this methodology does not allow distinguishing divergence from shear, as at least triplets of buoys should be used for this purpose. When analyzing the whole Arctic basin, we made a distinction between winter (from the beginning of December to mid-May) and summer (from mid-June to the end of September). Separately for both seasons, we computed the distributions of \dot{D} for various L and τ ranging from a few kilometers to 500 kilometers and from 3 hours to several months (one month for summer). For each space-time interval, the associated distribution is characterized by its standard deviation $\sigma_{\dot{D}}$, which is a function of L and τ . In this way, we measure how a cluster of passive tracers of initial size L typically disperses after a time τ or, in other words, how the associated region containing these tracers deforms (We will show in the next section two examples of how deformation and dispersion can be linked). The choice of the standard deviation of \dot{D} rather than its mean is partly motivated by the fact that in the limit of small deformation rate (i.e. for large time and spatial scales), only the standard deviation allows to characterize the deformation process. We checked this by calculating the two parameters for each computed distribution of \dot{D} (i.e. corresponding to each L - τ interval). We observed that the standard deviation of \dot{D} evolved over the entire L and τ ranges, whereas the mean remained insensitive to sea ice deformation at large spatial scales. In addition, the choice of the standard deviation was motivated by an analogy with the methodology used in fluid turbulence to characterize the dispersion of passive tracers.

The number N of measurements available in each L - τ interval for the distribution of \dot{D} is extremely variable, ranging from 920 to 812405 in winter, and from 6 to 257871 in summer. From these N measurements, many values can come from a single pair of buoys and thus are not independent. Indeed, the autocorrelation analysis of \dot{D} time records for an initial separation of $L \sim 300$ km shows a correlation time of approximately 10 hours. Thus, we only kept one \dot{D} -value in three provided by each pair of buoys. Moreover, the distributions of \dot{D} are clearly not Gaussian, with significantly slower decays towards large values (this aspect will be detailed in future work). All these observations suggest that we would under-estimate the errors on $\sigma_{\dot{D}}$ if we were to estimate it as $\Delta\sigma_{\dot{D}}/\sigma_{\dot{D}} = 1/\sqrt{N}$, i.e. using the central limit theorem. Instead, we estimated $\Delta\sigma_{\dot{D}}$ from a bootstrap method described in Appendix III-1, which led us to consider, instead of the number of samples, the number of pairs of buoys as an independent variable.

4. Introduction to the dispersion process: two examples of buoy dispersions

Most buoys are typically not clustered sufficiently well to determine the deformation as a cluster, although they can be easily grouped into pairs to estimate the dispersion (detailed in section III-3). However, two field projects (“SHEBA”, Surface Heat Budget of the Arctic Ocean, and “SIMI”, Sea Ice Mechanics Initiative) provide an opportunity to determine the relationship between two-point dispersion estimates of the deformation and multi-point (cluster) deformation estimates found by fitting a linear function of the velocity to the buoy positions. The buoys were deployed by the Cold Regions Research and Engineering Laboratory (the data sets are available on the web: www.crrel.usace.army.mil/sid/SeaIceDynamics/).

The experiments took place in the western Arctic close to the Alaskan coast (Figure III-3a) in winters 1997-1998 for SHEBA and 1993-1994 for SIMI. For each experiment, a set of N_b buoys is considered ($N_b = 6$ and 13 respectively), and we use the positions of the buoys over a period of approximately one month. At the beginning of this period the buoys form clusters of different initial sizes, $L^2 \sim 300 \text{ km}^2$ for SIMI and 8000 km^2 for SHEBA. Through time, these clusters deform. The two sets of trajectories are drawn on figures III-3b & III-3c with the positions of the clusters at the beginning and at the end of the period indicated. We illustrate here the link between the deformation of the underlying solid plate and the dispersion of buoys:

We follow a cluster of buoys between times t and $t + \Delta t$ ($\Delta t = 1$ hour) and estimate at various times t the strain tensor $\boldsymbol{\varepsilon}_{ij}(t)$ from each set of buoys. The actual deformation of the two sets of buoys shows spatial variability: it is not homogeneous over the whole region encompassed by the buoys. However, here we follow the deformation at the scale of those regions ($\sim 300 \text{ km}^2$ and $\sim 8000 \text{ km}^2$), and therefore assume a smooth, i.e. homogeneous, process for these observables. So we calculate the best coefficients of the matrix \mathbf{M}_{ij} that minimizes $\sum_k (\mathbf{r}_k - \mathbf{M}_{ij} \mathbf{x}_k)^2$, where \mathbf{r}_k is the displacement vector of the k^{th} buoy during Δt and \mathbf{x}_k its position at time t . \mathbf{M}_{ij} is the matrix of the displacement gradients. We compute the strain tensor $\boldsymbol{\varepsilon}_{ij}(t)$ from \mathbf{M}_{ij} as:

$$\boldsymbol{\varepsilon}_{ij} = \frac{1}{2} (\mathbf{M}_{ij} + \mathbf{M}_{ji}) \quad (\text{III-2})$$

Then we compute two invariants of the deformation, the divergence and the shear strain:

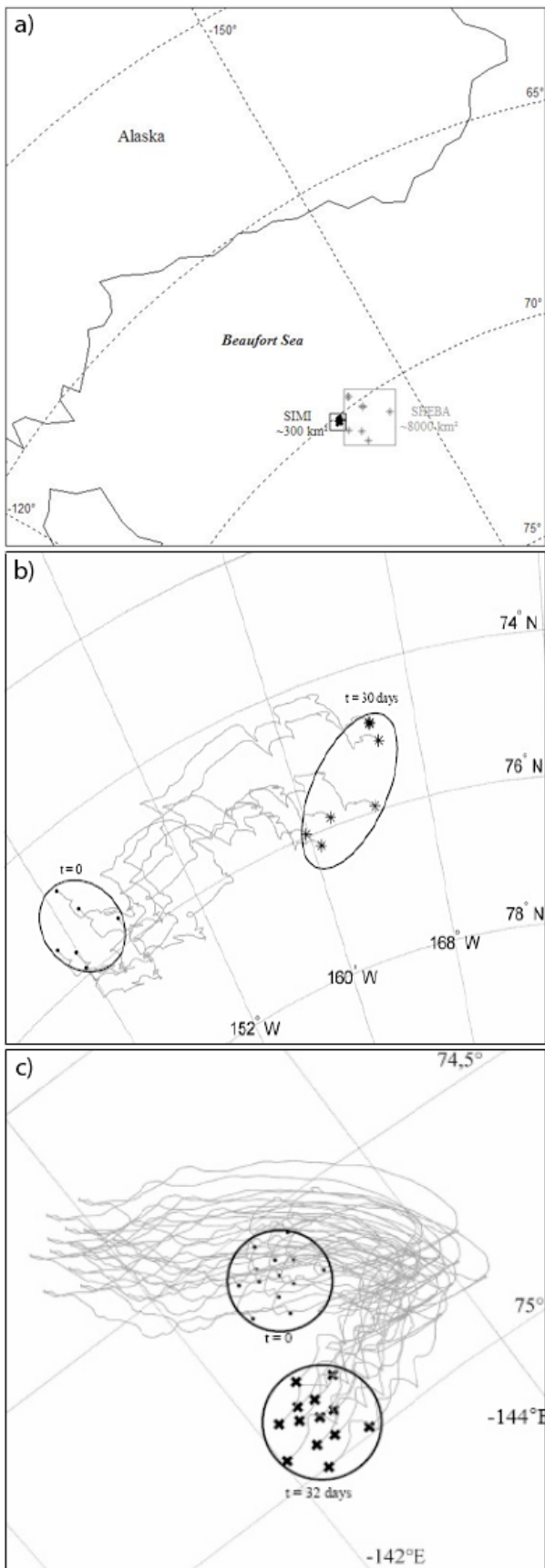


Figure III-3.

$$div = \operatorname{tr}(\boldsymbol{\varepsilon}_{ij}) \quad (\text{III-3})$$

$$shr = \left[(\varepsilon_{11} - \varepsilon_{22})^2 + (\varepsilon_{12} + \varepsilon_{21})^2 \right]^{1/2} \quad (\text{III-4})$$

Finally, we deduce the magnitude of the total deformation as:

$$\varepsilon_{tot} = \sqrt{div^2 + shr^2} \quad (\text{III-5})$$

Figure III-4 shows this deformation ε_{tot} along with the standard deviation σ_D of the deformation $D = \Delta r / L$ derived from the dispersion of the SHEBA buoys over a period of 100 days.

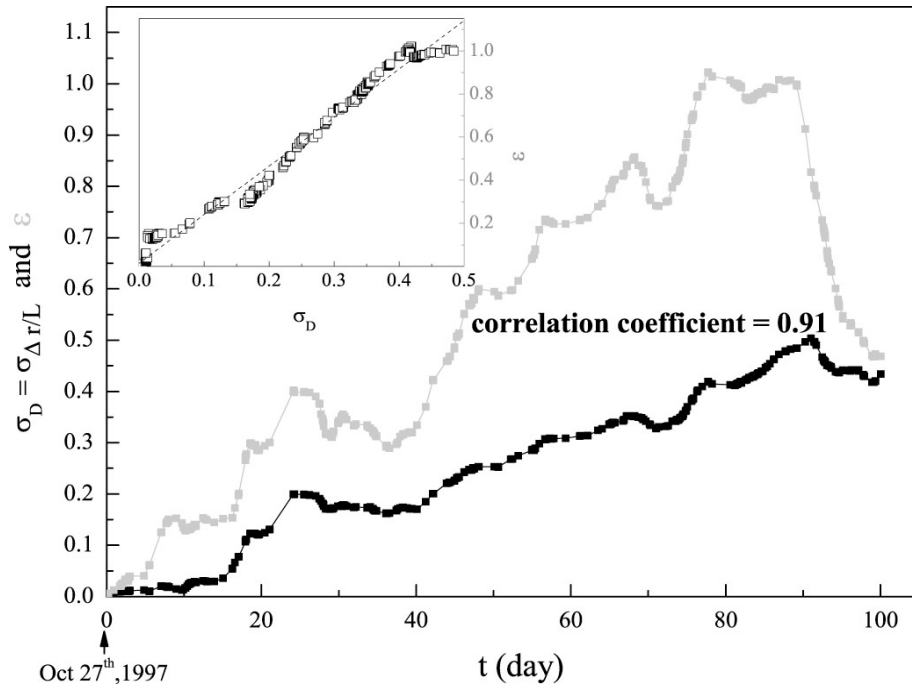


Figure III-4. Standard deviation σ_D of the deformation D (computed from the dispersion of pairs of buoys), and of the strain ε_{tot} versus time t , for the SHEBA experiment. The inset plot shows the proportionality between the both (the slope of the dashed line is about 2.25 ± 0.01).

We obtain a correlation coefficient of 0.91 between them, although σ_D is systematically smaller than ε_{tot} . It can be shown by simple Monte-Carlo simulations assuming homogeneous deformation that ε_{tot} is typically greater than σ_D by a factor of 4 on average with a standard deviation of about approximately 3. These simulations do not take into account the existing spatial correlations of the buoys trajectories. Therefore, this factor of proportionality is an upper bound estimate. For example, in a realistic case like SHEBA, the buoys trajectories are spatially correlated,

i.e. disperse less than one would expect for an equivalent cluster with uncorrelated trajectories, and this factor is less (i.e. approximately 2) (see the inset graph in figure III-4). We note also the large standard deviation associated with this ratio (i.e. 3). Consequently, the value of 2.25 obtained for SHEBA is not necessarily representative of the general case. In the case of SIMI, we look at the deformation of a "small" initial region (about 300 km²) compared to the SHEBA's one (about 8000 km²). Then, the dispersion is expected to be smaller too in magnitude (see details in the next paragraph), i.e. the relative displacements leading to this dispersion are smaller. This implies that the "signal over noise" (e.g. due to the position uncertainty) ratio is larger for SIMI than for SHEBA. Consequently, we found a less good correlation between ε_{tot} and σ_d for SIMI (e.g. ~ 0.65). In conclusion, this evidence shows that the sea ice deformation can be approximated by following the dispersion of pairs of passive tracers.

We also compute the mean square change in separation $\langle \Delta r^2 \rangle = \langle (r(t+\tau) - r(t))^2 \rangle$ as a function of τ (Figure III-5).

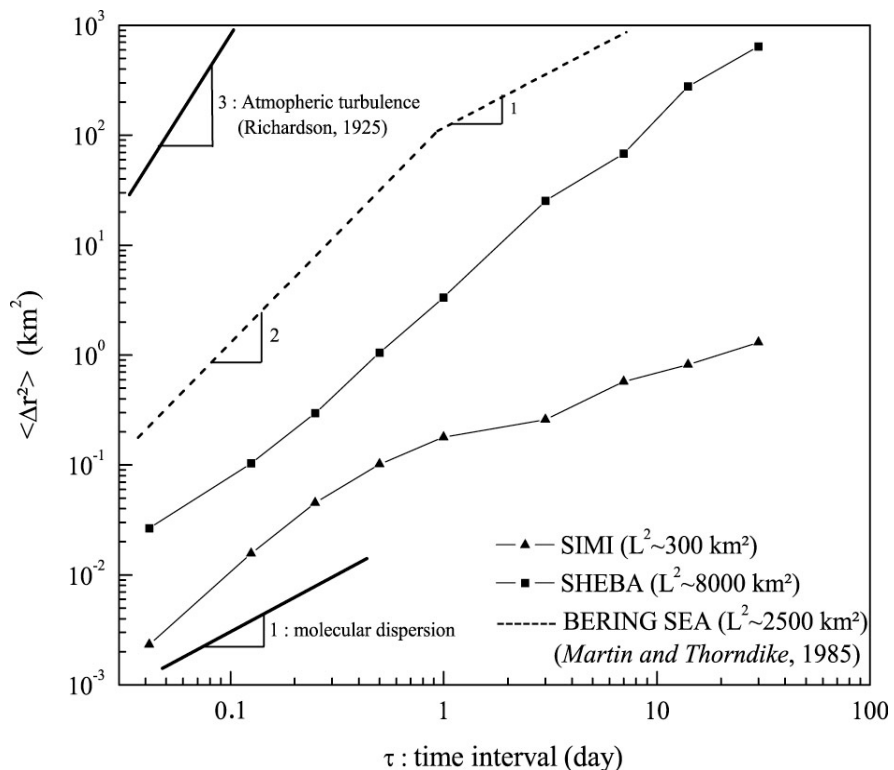


Figure III-5. $\langle \Delta r^2 \rangle$ versus the time interval τ for the SHEBA and SIMI clusters. The dashed line shows the results of *Martin and Thorndike* (1985) for their initial cluster of 2500 km². The lines with slope 1 and 3 are for reference only.

The number of values of Δr for each distribution ranged from 465 to 109122. $\langle \Delta r^2 \rangle$ is a quantity which characterizes the dispersion process [Richardson, 1926]. The magnitude of the dispersion is larger for SHEBA than for SIMI. However, *Martin and Thorndike* [1985] obtained, for an initial cluster of intermediate size ($\sim 2500 \text{ km}^2$), greater magnitudes than those for SHEBA and SIMI. We can reasonably imagine that stronger wind forcing and a thinner ice cover in the Bering Sea region (marginal sea of the Arctic basin) can lead to such large magnitudes of dispersion. The evolution of $\langle \Delta r^2 \rangle$ can be approximated by a power law scaling $\langle \Delta r^2 \rangle \sim \tau^\gamma$, with γ ranging between 1 and 3. We find that $\gamma \approx 1.6$ for SHEBA whereas, for SIMI, $\gamma \approx 1.6$ for $\tau < 1$ day, and $\gamma \approx 0.6$ for $\tau > 1$ day. We note here that molecular dispersion is characterized by $\langle \Delta r^2 \rangle \sim \tau$ [Einstein, 1905], whereas atmospheric turbulence is characterized by $\langle \Delta r^2 \rangle \sim \tau^3$ [Richardson, 1952]. In other words, sea ice deformation in these two regions is found to be characterized by a super-diffusive regime, although there is a hint for a sub-diffusive regime in the SIMI experiment for time scales greater than 1 day. The significant variation of γ from one experiment to another stresses the need to consider ensemble averages over the whole Arctic basin rather than particular regional experiments in order to obtain a global characterization of sea ice deformation. A comparison with the results of *Martin and Thorndike* [1985] illustrates this idea: they showed that for an area of about 2500 km^2 located in the Bering Sea $\langle \Delta r^2 \rangle \sim \tau^\gamma$ for $\tau < 1$ day, and $\langle \Delta r^2 \rangle \sim \tau$ for $\tau > 1$ day. The SIMI experiment is in relative agreement with this former study, whereas we obtained a different power law without any change in regime within the 3 hours-30 days interval for SHEBA.

A $\langle \Delta r^2 \rangle \sim \tau$ regime implies separation velocities increasing as $\Delta r / \tau \sim \Delta r^{-1}$ with decreasing Δr . Physically, this velocity cannot increase indefinitely toward small scales. So a change in regime, so that the velocity becomes constant (ballistic regime, with $\langle \Delta r^2 \rangle$ evolving as t^2), is expected to occur at short time scales [Taylor, 1921]. We did not observe this regime change with SHEBA, because the transition must occur at a characteristic time that is less than our resolution (i.e. for $\tau < 1$ hour).

Finally, we calculate the standard deviation σ_d of the deformation rate $\dot{D} = \Delta r / L\tau$, as well as the strain rate $\dot{\varepsilon}_{tot}$ (Figure III-6). Here, we consider the characteristic scale L instead of L^2 . The magnitude of σ_d is larger for the small cluster (i.e. SIMI) than for the large one (i.e. SHEBA), at short times τ , implying a stronger deformation rate at small spatial scales. In addition, σ_d reasonably fits a power law $\sigma_d \sim \tau^{-\alpha(L)}$. The exponent α is different for the two experiments, with

$\alpha = 0.7$ for small spatial scale (SIMI), and $\alpha = 0.2$ for the large spatial scale (SHEBA). These exponents are consistent with the exponents found for $\langle \Delta r^2 \rangle$ in the following way:

$$\sigma_{\dot{D}} \sim \tau^{-\alpha} \sim \dot{D} \sim r/\tau \sim \tau^{-1+\gamma/2} \quad (\text{III-6})$$

Hence $\alpha = 1 - \gamma/2$. For the SHEBA experiment, we can effectively check that: $\alpha = 1 - (1.6/2) = 0.2$. The systematic dependence of α with respect to L (or L^2) is discussed in section III-6. We also note that the two calculations of deformation rates, the first one from the strain rate tensor and the second one from the dispersion rate, lead to very similar power law trends. This confirms that one may use the dispersion of buoys to accurately estimate sea ice deformation rates, and the associated scaling laws.

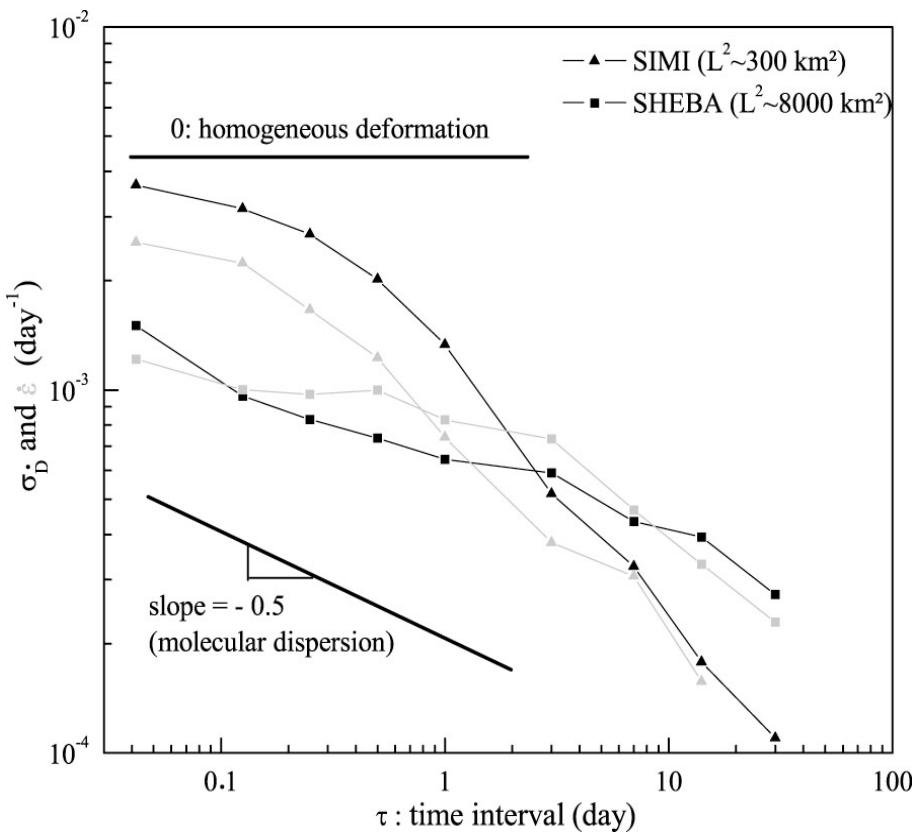


Figure III-6. Strain rate $\dot{\varepsilon}_{tot}$ and its proxy $\sigma_{\dot{D}}$ (standard deviation of \dot{D}) versus τ for the SHEBA and SIMI experiments. The horizontal line and the line with slope -0.5 are for reference only.

To summarize, this analysis of two clusters of buoys shows that:

(i) Arctic sea ice disperses as the result of deformation. Our two examples and the one of *Martin and Thorndike* [1985], which corresponds to different periods and regions of the Arctic, show similar qualitative trends but significantly different scaling exponents. This illustrates the strongly heterogeneous character of sea ice deformation, thus the need for ensemble averages to estimate robust scaling. Moreover, deformation rates decrease with the increasing time interval τ considered, highlighting the intermittency of this process.

(ii) The intensity of the dispersion and the magnitude of the deformation rates depend on both spatial and temporal scales.

(iii) Both dispersion and deformation rates scale with the time interval τ as power laws.

(iv) These exponents depend on the spatial scale L (or L^2). As L increases, the dispersion increases whereas the deformation decreases. This implies a non-trivial coupling between space and time in the dispersion/deformation process.

These two experiments only concern limited spatial and time scales, and specific regions of the Arctic basin. Thanks to the exceptional dataset provided by IABP, we can extend the analysis to the whole Arctic Ocean and up to a time scale of several months.

5. Sea ice dispersion and deformation over the whole Arctic Ocean: Results

We now consider the time and spatial scaling of sea ice deformation rate for the whole Arctic Ocean, based on the dispersion of pairs of buoy trajectories (Figure III-1).

5.1 Time scaling

Figures III-7a & III-7b show the standard deviation of the deformation rate σ_d versus the time interval of observation τ for winter and summer, respectively. Due to the small number of independent observations for some distributions, the errors on σ_d can be very large, as mentioned in section III-3. The estimation of these errors bars is detailed in Appendix III-1; they increase as the time scale increases and the spatial scale decreases. We observe a power law scaling, $\sigma_d \sim \tau^{-\alpha(L)}$, over 3 orders of magnitude.

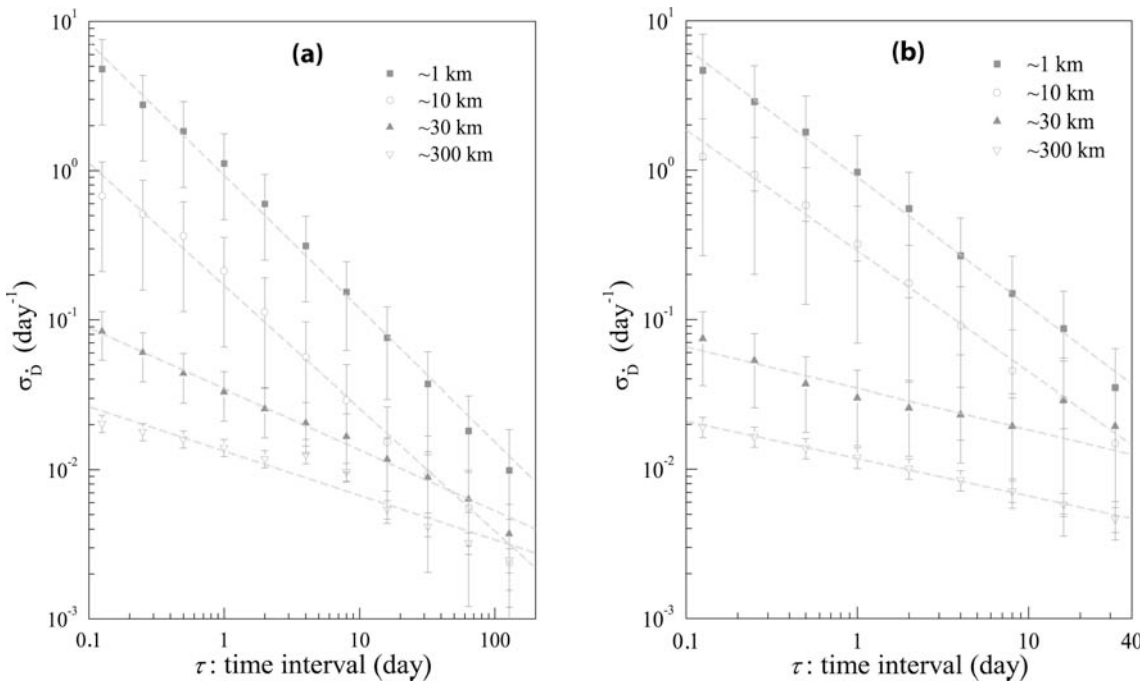


Figure III-7. (a) σ_d versus τ for $L = 1, 10, 30$ and 300 km, and the winter season. The L -values correspond to the spatial bins: $0.3\text{-}2$ km, $2\text{-}16$ km, $16\text{-}64$ km, and $64\text{-}512$ km respectively. Error bars are estimated by a bootstrap method (see appendix III-1). The gray dashed lines show the best power law fit (in the least squares sense) to the 4 data sets. (b) Same as figure III-7a, for summer.

The exponents α were determined using a weighted least squares algorithm (The weights depending on the error bars). The corresponding errors in the calculation of the slopes range from 7% to 25%. The exponents α increase with decreasing initial separation L , ranging from 0.89 for $L=1$ km to 0.30 for $L=300$ km in winter and from 0.87 for $L=1$ km to 0.25 for $L=300$ km in summer (Figure III-8). Thus, we note that the seasons cannot be distinguished in terms of scaling exponents.

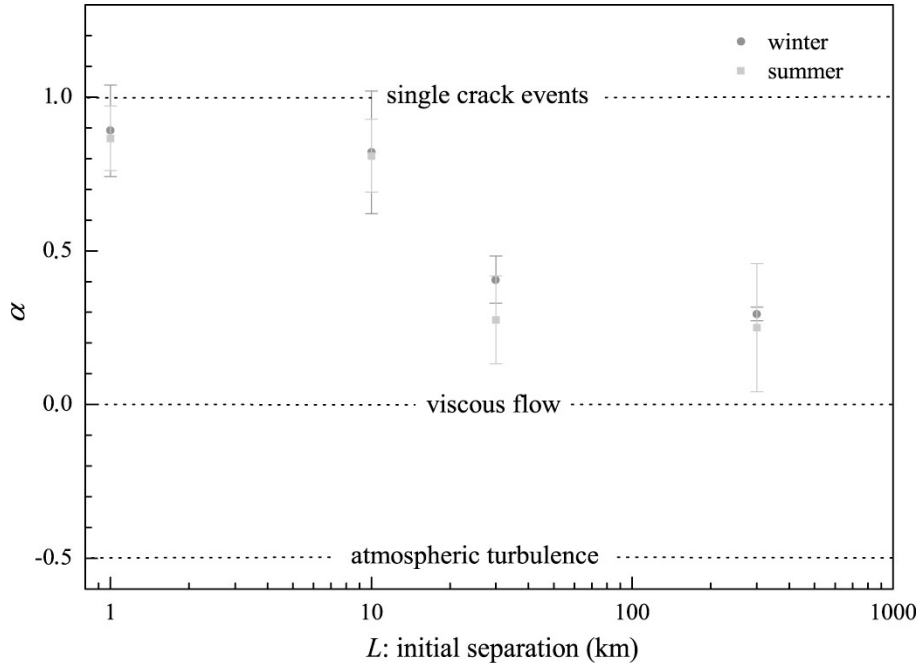


Figure III-8. Power law exponent α versus initial separation L for winter (circles) and summer (squares). Dashed lines represent the α -values corresponding to (i) an extremely intermittent deformation process (temporal fractal dimension equals to zero), (ii) a non-intermittent viscous flow, and (iii) atmospheric turbulence.

The apparent change of slope value between the power law for $L=10$ km the one for $L=30$ km, i.e. over a very short range of scales, is discussed in section III-6 through an analysis of the spatial scaling.

5.2 Spatial scaling

Figures III-9a & III-9b show σ_d versus the initial separation L , for winter and summer respectively.

Errors of σ_d are once again very large and increase as time scale increases and spatial scale decreases.

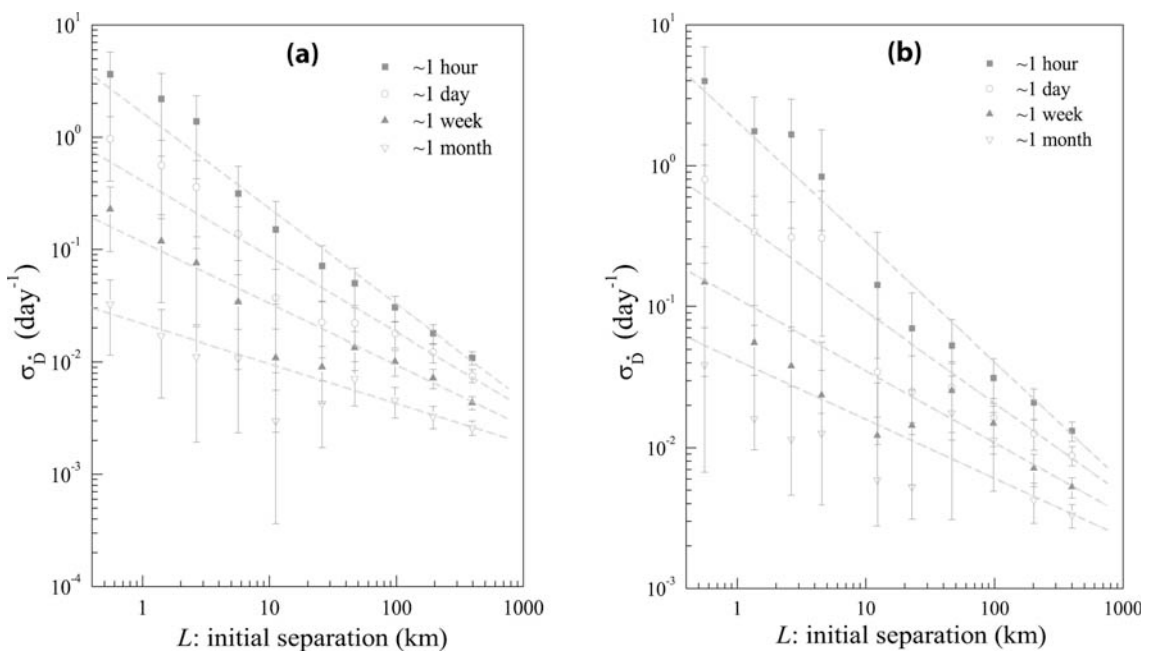


Figure III-9. (a) σ_d versus the initial separation L for $3 \leq \tau \leq 12$ hours, $1 \leq \tau \leq 4$ days, $8 \leq \tau \leq 16$ days, $32 \leq \tau \leq 128$ days, for the winter season. Error bars are estimated by the bootstrap method of appendix III-1. The gray dashed lines show the best power law fit (in the least squares sense) to the 4 data sets. (b) Same as figure III-9a, for summer. The time intervals are redefined as: $3 \leq \tau \leq 12$ hours, $1 \leq \tau \leq 4$ days, $8 \leq \tau \leq 16$ days, $32 \leq \tau \leq 64$ days.

Similarly to the dependence with time, we observe for both seasons a power law spatial scaling, $\sigma_d \sim L^{-\beta(\tau)}$, over 3 orders of magnitude although this scaling is far from being as well-defined as in the temporal case. In the temporal case, the pairs of buoys considered do not change as we consider different temporal scales, i.e. we look at approximately the same regions for two different τ . In contrast, as L changes, we sample different regions of the Arctic, as the pairs of buoys considered are not the same. So first, this could partly explain the noise seen in the spatial scaling.

Second, we expect inhomogeneous forcing at large time or space scales and the influence of the coasts to be possible causes for a bias on the σ_D -values. The inhomogeneous forcing arises from the large-scale variability in the mean wind and water stresses over the basin [Steele *et al.*, 1997].

The exponents β were determined using a weighted least squares algorithm. The corresponding uncertainty in β ranges from 15% to 80%. The exponent β increases with decreasing time scale τ , ranging from 0.85 for $\tau = 1$ hour to 0.35 for $\tau = 1$ month in winter and from 0.85 for $\tau = 1$ hour to 0.42 for $\tau = 1$ month in summer (Figure III-10). Once again, winter and summer cannot be distinguished on this basis.

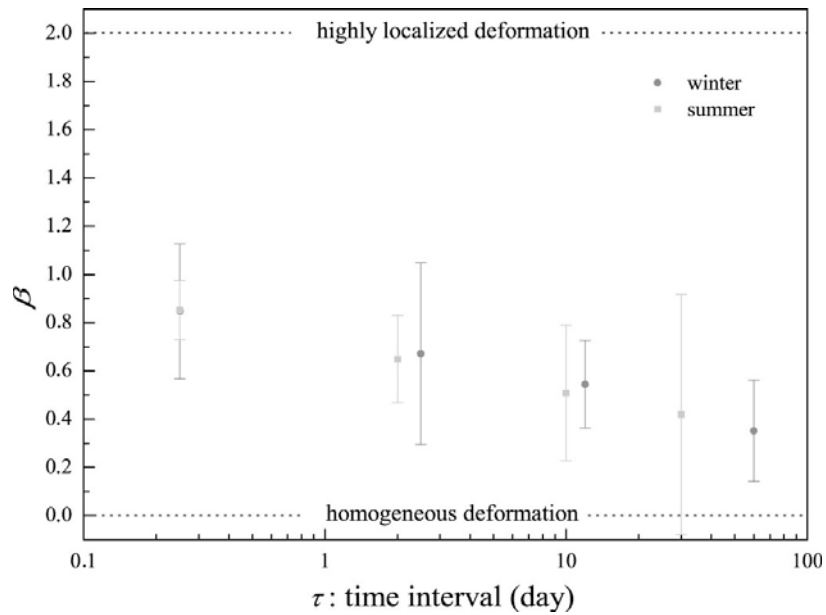


Figure III-10. Power law exponents β versus time interval τ for winter and summer. Dashed lines represent two characteristic deformation processes, from a homogeneous one to a highly localized one (spatial fractal dimension equals to zero).

6. Discussion

As a generalization of the examples studied in the section 3, the magnitudes of the deformation rates have been shown to depend on L and τ : Deformation rate increases as L and τ decrease. As a point of comparison, the deformation rate in winter for $L > 100$ km and $\tau = 3$ days is about 10^{-2} day $^{-1}$, which is in close agreement with the estimate of *Marsan et al.* [2004] from RGPS data.

6.1 Time scaling

Following expression (III-6), we estimate the exponents γ for the time scaling of the dispersion (i.e. for $\langle \Delta r^2 \rangle \sim \tau^\gamma$), from the exponents α observed for the time scaling of the deformation. We find $0.22 < \gamma < 1.44$, from small to large spatial scales L . The deformation of Arctic sea ice appears to follow different regimes, from sub-diffusive (at $L \leq 10$ km) to super-diffusive (at $L \geq 10$ km). However, for any particular scale L , we cannot define a characteristic time at which a change in regime occurs. This shows that the time scaling of the dispersion found by *Martin and Thorndike* [1985] and the one found in the SIMI case (see section III-4) cannot be considered, in a statistical sense, as representative of general sea ice dynamics. In other words, a variety of time scaling can be found locally, and depends on the spatial scale considered.

The evolution of the time scaling exponent α with increasing spatial scale L (Figure III-8) can be interpreted if one considers the deformation of sea ice to be accommodated by a multiscale fracturing process [*Marsan et al.*, 2004]. The exponent α is then a measure of the degree of intermittency of the deformation process: at small L , this process is highly intermittent, and α is close to the unit case $\alpha = 1$ corresponding to deformation accommodated “by a single fracturing event”. As L increases, the average effect of an increasing number of fractures causes the deformation to become “smoother” in time, i.e. α decreases. However, α is positive even at the largest spatial scale considered here ($L \sim 300$ km), i.e. sea ice deformation is always intermittent and does not mimic viscous flow. This shows that the hypothesis of viscous flow in sea ice models [*Hibler*, 1977] is not fulfilled, even at very large spatial scales. On the other hand, we are far from the case of atmospheric turbulent dispersion ($\alpha = -0.5$), corresponding to the “ t^3 law” [*Richardson*, 1925].

6.2 Spatial scaling

Just as the time scaling exponent α depends on L , the spatial scaling exponent β depends on the time scale τ (Figures III-9a & III-9b).

Turbulence theory predicts a characteristic time at which the regime of dispersion changes. *Batchelor* [1960] and *Kraichnan* [1966] showed that, for small τ , $\langle \Delta r^2 \rangle \sim L^{2/3}$, and for large τ , $\langle \Delta r^2 \rangle \sim L^{4/3}$. Translated in terms of deformation rate, this means that, for small τ , σ_d scales as $L^{-2/3}$, and for large τ , σ_d scales as $L^{-1/3}$. In our case, a characteristic time cannot be distinguished. The exponent β decreases continuously as τ increases (Figure III-10). This leads to the conclusion that time and space scales are strongly coupled and cannot be separated for Arctic sea ice deformation, or, in other words, that the scaling of σ_d does not reduce to $L^{-\beta}\tau^{-\alpha}$.

As α is a measure of the degree of temporal intermittency, β is a measure of the degree of spatial heterogeneity of sea ice deformation. The boundary value $\beta=2$ would correspond to a highly localized deformation process, e.g. a single fracture in an elastic medium, whereas $\beta=0$ indicates homogeneous deformation (e.g. elastic or viscous). Here, β is always far from the boundary value $\beta=2$ and decreases towards large time scale τ , as more and more fracturing events are taken into account. However, it never reaches the homogeneous case ($\beta=0$), even at large time scales ($\tau \sim 2$ months). Once again, the viscous flow hypothesis is not fulfilled.

Considering the role of oceanic driving, *Okubo* [1974] found from the analysis of buoy dispersion that $\langle \Delta r^2 \rangle \sim L^{1.1}$ for surface oceanic turbulence. This translates into $\beta=0.45$. This is close to the value obtained at large time scales (Figure III-10) for both winter and summer seasons. In other words, sea ice dispersion mimics a free drift, oceanic dispersion only at large time scales (i.e. > 1 month). At smaller scales (i.e. < 1 month), the elasto-brittle behaviour of Arctic sea ice results in a much more heterogeneous and localized deformation. This transition at ~ 1 month can therefore be viewed as an integral scale at which the sea ice deformation is driven by oceanic forcing.

As shown above, the results of figures III-9a & III-9b are compatible, within the large error bars, with a single spatial scaling. However, it is possible to differentiate two different regimes, separated by a transition scale of about 10 km (Figure III-11a). The evolution of the corresponding slopes $\beta_{<10km}$ and $\beta_{>10km}$ with increasing time scale τ is shown in figure III-11b. A possible interpretation of a change of dispersion regime is related to ocean dynamics. Indeed, this

10 km scale is known to be consistent with a class of dynamical structure in the ocean: an estimation of the internal Rossby radius at northern latitudes leads to the same order of spatial scale.

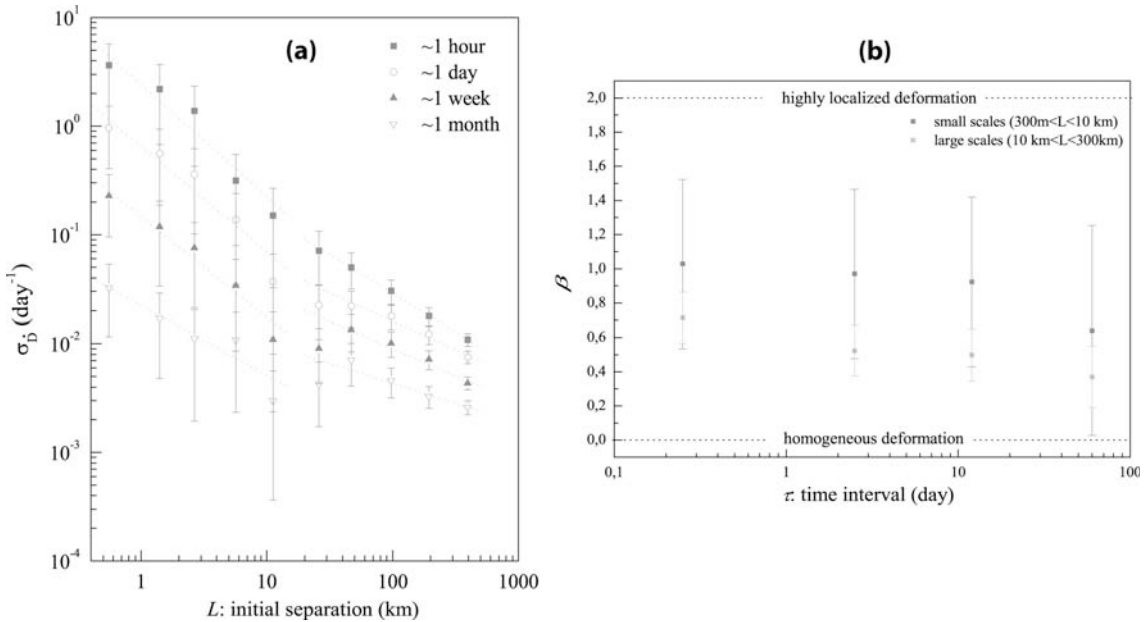


Figure III-11. (a) Same as figure III-9a, but with power law fits assuming a regime change at ~ 10 km. (b) Same as figure III-10, but separating the two space intervals $L < 10$ km and $L > 10$ km (see figure III-10)

Therefore, this possible regime change could indicate the role of oceanic dynamical structures such as eddies. However, owing to the fact that both interpretations (1 or 2 dispersion regimes) are compatible with our results and the associated uncertainties, further studies are needed to definitively answer this question.

6.3 Seasonal dynamics of sea ice

On the basis of the scaling properties summarized in figures III-8 & III-10, winter and summer sea ice dynamics cannot be differentiated. Whatever the time or spatial scales considered, the magnitudes of σ_b are very similar in winter and summer, from 10 day^{-1} for small time and spatial scales, to 10^{-3} day^{-1} for large scales. This might appear, at first glance, in contradiction with the expectation that a loose summer ice pack would disperse and deform according to a free drift regime. As shown above, this free drift regime is only recovered at large time scales in both winter and summer. Even if the loose assembly of ice floes characterizing the marginal ice zone bordering the perennial ice pack might behave differently, our results suggest that the perennial sea ice cover of the central Arctic basin (from which most of the buoy observations come; see figure III-1) behaves as a fractured solid plate, just as the winter ice cover does, and not as a free assembly of floes. This may have major implications in terms of global sea ice drift or sea ice mass balance.

6.4 Perspectives for future studies

We recall that for the homogeneous deformation of a typical solid (i.e. elastic deformation or viscous flow), the deformation rate does not depend on the time and spatial scales (i.e. $\alpha = 0$ and $\beta = 0$). The present observations argue for sea ice deformation characterized by both intermittency and heterogeneity, and by a strong space-time coupling. The next step would be to quantify this space-time coupling, searching for a general link between the distributions of strain rates at different space and time scales. Then it might be possible to completely characterize the scaling properties of the sea ice deformation and deduce, by downscaling or upscaling, useful information for modellers to use for model validation.

7. Conclusions

In summary, the primary conclusions of our analysis of buoy trajectories are:

- (i) The deformation of sea ice is the result of a highly intermittent and heterogeneous dispersion process.
- (ii) The deformation depends on both space and time scales. We showed that it follows a power law model that is scale invariant over several orders of magnitude in time and space.
- (iii) The values of the exponents of the power functions depend on both time and space scales. This leads us to conclude that time and space scales are coupled.
- (iv) Even for large time scales, i.e. several months, and for the Arctic basin scale, i.e. 1000 km, we showed that Arctic sea ice deformation does not mimic viscous flow, a contradiction to the classical sea ice modeling assumption.

Acknowledgments We thank I. Rigor from the Polar Science Center of Seattle for the compilation and the distribution on the web of the IABP dataset. We also thank J. Richter-Menge and C. Geiger from CRREL who kindly provided the SIMI and SHEBA data sets. The work of R.L. and H.S. was supported by grants from the National Science Foundation. Two anonymous reviewers are greatly thanked for their constructive reviews.

Appendix III-1: Estimating uncertainties on $\sigma_{\dot{D}}$, the standard deviation of \dot{D} .

Time correlations (memory effects) are present in ice velocity records [Thorndike, 1986a, 1986b], and can also be found in time series of ice deformation rates as measured by the dispersion of pairs of buoys. An autocorrelation reveals a decorrelation time of about 10 hours for an initial separation of $L \sim 300$ km. This decorrelation time becomes smaller for small L . In addition, strong spatial correlations are present in the deformation field [Marsan et al., 2004]. Consequently, the errors on the estimation of $\sigma_{\dot{D}}$ cannot be obtained directly from the central limit theorem and the number N of samples, as it is usually assumed that those N samples are independent of each other. Instead, we estimate these errors from a bootstrap method. It can be shown that the number of pairs of buoys N_p taken into account in each distribution, rather than the number of samples N , should be used as the number of independent variables. N_p ranges from 3 to 686 for winter, and from 1 to 463 for summer. In order to empirically find how the error $\Delta\sigma_{\dot{D}}/\sigma_{\dot{D}}$ depends on N_p , we selected those distributions that contain $N_p \geq 100$ pairs. Then, we randomly picked q times ($q \geq 10$), all the $\sigma_{\dot{D}}$ -values coming from n independent pairs of buoys, taking care not to pick the same pair twice, with the condition $q \times n \approx 0.75N_p$. Then, we obtain, for each couple (L, τ) , q distributions of $\sigma_{\dot{D}}$ -values for which we calculate their standard deviation S . In other words, the S -values correspond to the dispersion of $\sigma_{\dot{D}}$ around its mean, for a given n . Fig.A1 shows the results of this method for 3 different distributions corresponding to 3 different couples of scales (L, τ) . Finally, we obtain that S decreases with n as:

$$S = \Delta\sigma_{\dot{D}} = f(\sigma_{\dot{D}}, n) = (A \times \sigma_{\dot{D}})/n^{\lambda} \quad (\text{III-A1})$$

where $\sigma_{\dot{D}}$ is the value of the standard deviation found for a particular distribution, A is about 0.9, and λ is approximately equal to 0.4. In our analysis, we use this relation to estimate the uncertainty in $\sigma_{\dot{D}}$.

We note that this expression is similar to the error estimate given by the central limit theorem, with the important difference that the number of pairs of buoys N_p is considered instead of the number of samples N . Also, the values of A and λ differ slightly from $A=1$ and $\lambda=0.5$ as would be expected if the central limit theorem would apply.

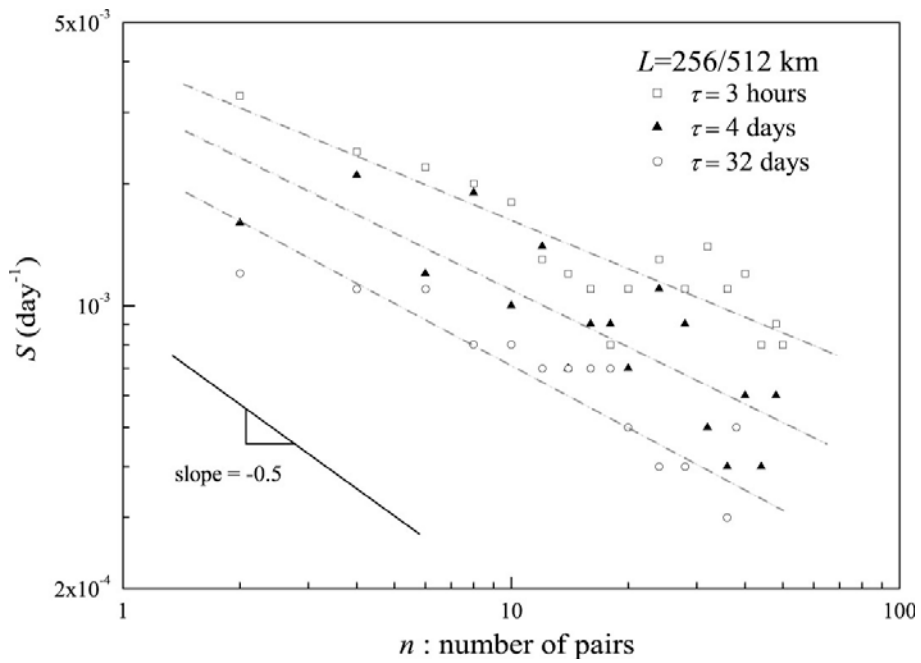


Figure III-A1. Standard deviation S of σ_d versus the number of pairs n , for the spatial bin 256-512 km and three different time intervals τ . The dashed lines are the best power law fit to the data. The black line with slope -0.5 shows $S(n)$ if the central limit theorem would apply.

Chapitre IV :

Conclusions et

Perspectives

1. Conclusions

Les conclusions que nous pouvons faire à la suite de ce travail de thèse sont les suivantes :

- (i) Les vitesses de dérive et de déformation de la banquise Arctique ont sensiblement augmenté durant les 30 dernières années, phénomène probablement lié à son amincissement tel qu'il est observé sur cette même période.
- (ii) Une importante déformation allant de pair avec une fracturation plus intense, cette dernière a pu jouer un rôle non négligeable dans la disparition progressive de la banquise via un renforcement de la boucle de rétroaction de l'albédo (voir ci dessous, sous-section 2.1 et figure IV-1). Elle peut également expliquer l'augmentation de la vitesse de dérive moyenne de la banquise citée ci-dessus, qui du fait de sa fracturation croissante, est de plus en plus fragmentée et sensible aux forçages atmosphérique et océanique.
- (iii) Le champ de vitesse de la banquise Arctique peut être décomposé en un champ moyen et un champ fluctuant. Pour cela, le champ moyen doit être calculé à des échelles de temps et d'espace que nous avons établi dans le chapitre II de cette thèse.
- (iv) Le champ fluctuant ainsi défini montre des caractéristiques similaires à celles du champ fluctuant d'un fluide turbulent homogène et isotrope [*Taylor*, 1921]. Le temps intégral ainsi que la diffusivité sont du même ordre de grandeur que ceux établis pour l'océan de surface. Cependant, les distributions de vitesses fluctuantes sont des exponentielles et non des gaussiennes comme c'est le cas dans l'océan ou l'atmosphère par exemple.
- (v) Plus généralement, le champ de vitesse de la banquise montre des propriétés d'intermittence, exprimées par une invariance d'échelle multifractale des incrément de vitesse.
- (vi) Cette intermittence n'est pas l'empreinte directe de la turbulence océanique, et ne peut être expliquée uniquement par la nature des forçages océaniques et atmosphériques. La réponse mécanique de la banquise à ce forçage, et particulièrement son comportement elasto-fragile, joue probablement un rôle dans cette intermittence.

- (vii) Le champ de déformation de la banquise Arctique peut être caractérisé grâce aux propriétés de dispersion de bouées qui sont enchaînées dans la couverture de glace. Ainsi nous avons montré que la banquise se dispersait suivant des lois qui lui sont propres et qui se démarquent de celles obtenues pour la dispersion de traceurs dans les fluides turbulents.
- (viii) Le champ de déformation de la banquise Arctique est caractérisé par une forte intermittence et une forte hétérogénéité, y compris aux grandes échelles (plusieurs mois et plusieurs centaines de km). De ce fait, l'hypothèse qui voudrait que la banquise ait un comportement visqueux-plastique à des échelles suffisamment grandes est fausse, ce qui contribue à remettre en question l'efficacité des modèles de banquise actuels qui utilisent cette hypothèse.
- (ix) L'intermittente et l'hétérogénéité de la déformation de la banquise Arctique sont exprimées par une invariance d'échelle où temps et espace sont couplés.

Tous ces résultats offrent des pistes nouvelles de recherche en termes de concept de modélisation de la banquise, mais également de manière plus générale sur les lois d'échelle et le couplage espace-temps accompagnant la déformation elasto-fragile des solides géophysiques. Plus généralement, ce travail de thèse nous montre que les effets non linéaires, présents aussi bien en mécanique du solide que celle des fluides, ont un caractère universel.

2. Discussion et perspectives

2.1 Intensification de la boucle de rétroaction de l'albédo

Nous avons vu dans le Chapitre I que les vitesses de dérive et de déformation de la banquise ont sensiblement augmentées entre 1979 et aujourd’hui. Cette intensification de la cinématique de la banquise peut être incorporée à la boucle de rétroaction de l’albédo (présentée en Introduction de ce mémoire en figure 5, et actualisée ci dessous dans la figure IV-1), où elle pourrait jouer un rôle essentiel en la renforçant sensiblement.

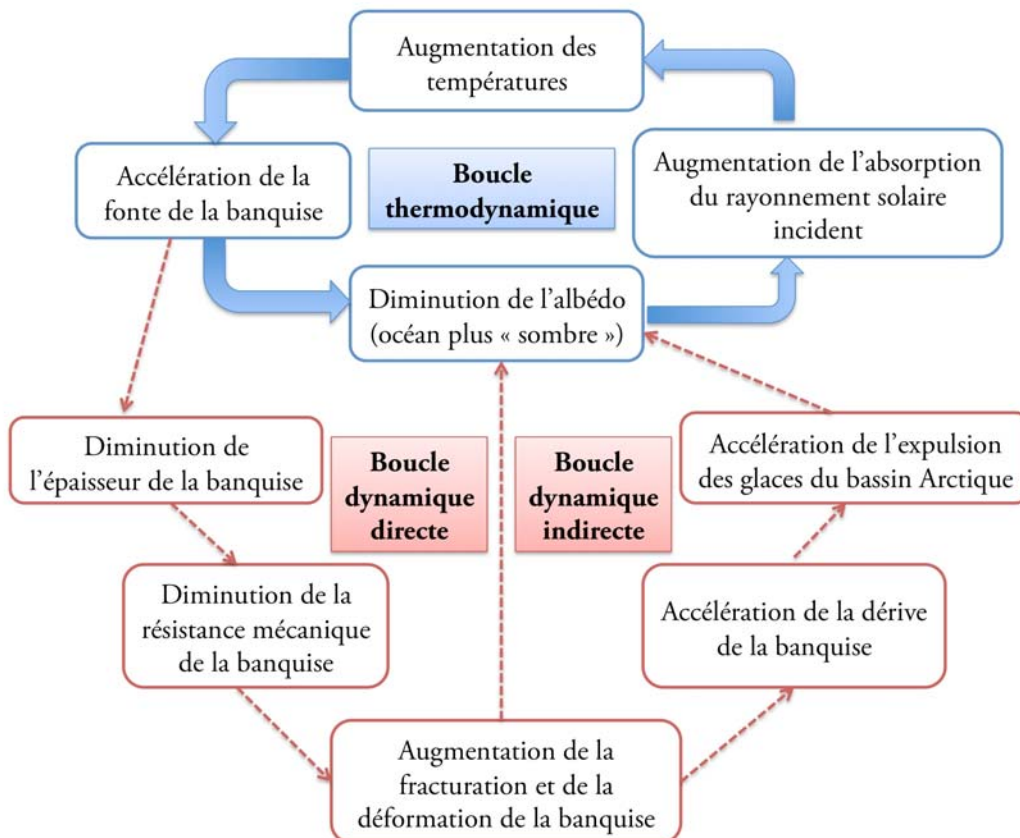


Figure IV-1. Boucle de rétroaction de l’albédo modifiée, montrant l’interaction possible entre les processus thermodynamiques (en bleu) et mécaniques (en rouge).

En effet, la diminution de l’épaisseur moyenne des glaces de mer a pour conséquence de rendre la banquise plus fragile et donc plus sensible à la fracturation, qui à son tour peut entraîner un accroissement de la fonte estivale, une accélération de la dérive et éventuellement de l’export de

glace hors du bassin Arctique par le détroit de Fram. La conséquence en terme d'accélération de la dérive de la banquise peut être illustrée par le voyage qu'a effectué le voilier polaire Tara (<http://www.taraexpeditions.org/tara>). Parti en septembre 2006 du port de Tiksi au nord de la Sibérie, c'est à dire sensiblement du même point que le Fram 113 ans plus tôt, le Tara s'est laissé prendre dans les glaces pour dériver tel un traceur passif de la banquise. Ainsi, Tara a traversé le bassin Arctique via le courant transpolaire en 2 fois moins de temps que le navire de Fridtjof Nansen, pour finalement poser l'ancre dans l'archipel du Svalbard en Février 2008.

2.2 Prise en compte du processus de fracturation dans les modèles

Le constat est sans appel : les modèles climatiques actuels sous-estiment la disparition de la banquise Arctique (voir e.g. Stroeve *et al.* [2007] et figure IV-2). On est donc amené à se demander si l'une des causes de cette sous-estimation n'est pas une mauvaise prise en compte des processus mécaniques impliqués dans la boucle de rétroaction modifiée de l'albédo.

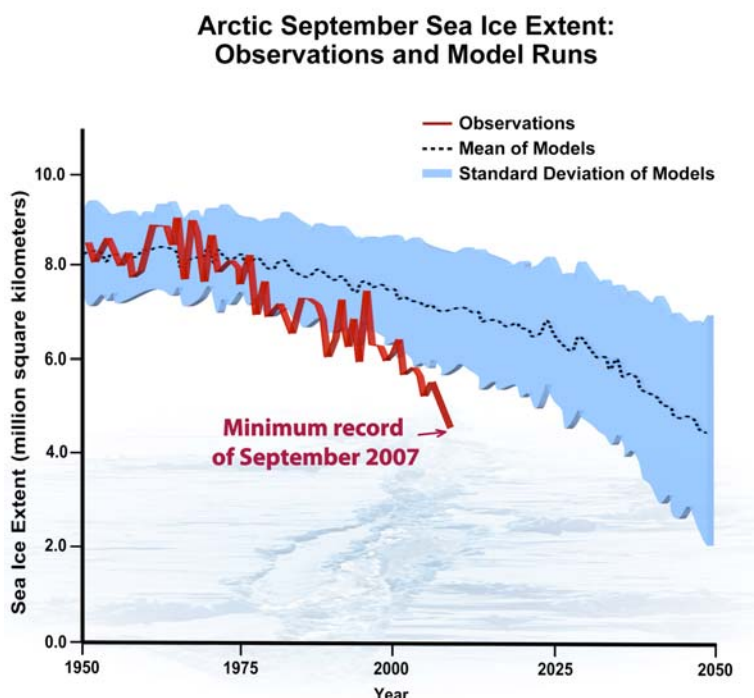


Figure IV-2. Evolution de l'extension spatiale de la banquise, prédicté par les modèles (en pointillés noirs), et observée (en rouge).
Source : Stroeve *et al.* [2007]

Ceci nous amène alors à revenir sur l'idée que la banquise Arctique ait pu dépasser un seuil critique via un amincissement important de sa couverture ayant conduit à une diminution sensible

de sa résistance mécanique. Du fait de l'importance du processus de fracturation dans la boucle de rétroaction de l'albédo présentée plus haut, une modélisation approprié de celui-ci apparaît comme essentielle si l'on veut tenter de prédire l'avenir de la banquise, et plus généralement celui du climat de la planète. Malheureusement, nous avons rappelé en introduction, et montré dans les chapitres I et III, que la banquise est actuellement modélisée tel un fluide visqueux-plastique qui, de toute évidence, ne peut reproduire de manière satisfaisante le processus de fracturation. Récemment, une analyse statistique de la cinématique de la banquise issue de sorties de modèles confirme que les propriétés d'intermittence du champ de vitesse (Chapitre II), mais également celles d'intermittence et d'hétérogénéité du champ de déformation (Chapitre III) ne sont pas reproduites [*Girard et al., en prép.*]. Cela n'est pas une grande surprise au regard de la rhéologie qui est adoptée pour modéliser la banquise dans les MGC, donnant de manière générale des champs beaucoup trop « lisses ».

Les recherches effectuées durant cette thèse nous ont donc conduit à réfléchir sur le développement d'une nouvelle approche afin de mieux modéliser la banquise. Elle s'appuie sur une rhéologie elasto-fragile qui pourrait permettre de reproduire les processus mécaniques observés, ces derniers résultant de tout évidence d'une mécanique de seuil (Voir section 3 et l'Annexe I pour plus de détails). Des travaux ont d'ores et déjà été engagés sur la modélisation de la banquise au LGGE, dans le cadre de la thèse de Lucas Girard qui a débuté en septembre 2007. Des premiers résultats convaincants ont été obtenus grâce à l'utilisation d'un modèle de rupture fragile développé par *Amitrano et al. [1999]*, ce modèle étant initialement utilisé pour mettre en évidence la complexité émergeant du comportement des solides sous contraintes. Pour finir sur ce point, il est également bon de rappeler ici qu'une fois ce modèle mis au point, son intégration dans les MGC représentera alors à plus long terme un réel défi pour la communauté scientifique...

2.3 La banquise: un objet géophysique modèle

D'un point de vue plus fondamental, il est également intéressant d'étudier la déformation et la fracturation de la banquise, ainsi que les lois d'échelles espace-temps associées (Chapitre III). En effet, une analogie poussée peut-être faite entre la dynamique de la banquise et la dynamique de la croûte terrestre.

2.3.1 Origine des propriétés d'échelle de la banquise Arctique

On pourrait en premier lieu se demander si les propriétés d'échelle de la banquise ne sont pas dues aux propriété d'échelle du forçage dynamique principal auquel elle est soumise, a savoir les vents. La réponse est négative, puisque (i) le comportement de la banquise est cassant, matérialisé par les multiples fractures qui s'y forment et (ii) les exposants des lois d'échelles de la dispersion diffèrent de ceux établis pour la turbulence atmosphérique (voir Chapitre III).

L'hypothèse que nous pourrions alors formuler est que la banquise est le support d'une « turbulence solide » conduite par le processus de fracturation s'effectuant à toutes les échelles de temps et d'espace. Là où la turbulence fluide est dictée par des cascades de tourbillons et de filaments de vorticité, la turbulence de la banquise serait donc dictée par une multitudes de fractures de taille variable. C'est ici qu'une analogie entre croûte terrestre et banquise peut s'établir. Cowie *et al.* [1995], par exemple, réussirent grâce à un modèle de rupture à reproduire l'invariance d'échelle multifractale du champ de déformation qui est observée pour une plaque tectonique. Ce modèle était basé sur les hypothèses suivantes : Corrélation à longue distance des contraintes élastique s'opérant dans le milieu, une rhéologie caractérisée par une mécanique de seuil et un bruit appliqué sur des paramètres du système (e.g. sur le seuil de rupture). Nous avons donc proposé de reproduire les lois d'échelle de la déformation de la banquise grâce à un modèle simple de fracturation multi-échelle (voir Weiss *et al.* [2008] en Annexe 1 de ce mémoire).

2.3.2 Un modèle de fracturation multi-échelle afin d'expliquer les lois d'échelle de la banquise ainsi que le couplage espace-temps

Le modèle présenté dans l'article de Weiss *et al.* [2008] est basé sur des hypothèses communément faites dans le cadre de l'étude de la croûte terrestre et de sa sismicité, a savoir :

- (i) La déformation d'un domaine de taille R est accommodée par N événements de fracturation indépendants

- (ii) Le déplacement moyen u effectué le long des fractures dépend de la longueur L de ces dernières
- (iii) Les événements de fracturation sont amassés dans l'espace, en imposant une distribution fractale de leurs barycentres
- (iv) Les événements de fracturation sont amassés dans le temps, en imposant une distribution fractale de leurs dates d'occurrence
- (v) Les tailles M des événements sont distribuées selon une loi de Lévy, équivalente à la loi de Gutenberg-Richter opérant pour les tremblements de terre

2.3.3 Conclusion

La conclusion que nous pouvons faire de ce travail est que le couplage espace-temps de la déformation de la banquise est similaire au couplage espace-temps existant pour la déformation de la croûte terrestre. Dans les deux cas, le couplage est dû à la sismicité s'opérant dans le milieu, qui se matérialise par des séquences de répliques faisant suite à chaque événement de fracturation. Les séquences de réplique peuvent de ce fait être vues comme le témoin d'un processus de cascade qui caractérise la « diffusion » de la déformation dans ces matériaux solides. Plus généralement, on peut se demander si le couplage espace-temps des lois d'échelle de la déformation ne pourrait pas être le témoin d'un caractère universel des objets présentant un comportement fragile aux échelles géophysiques...

Bibliographie

- Alam, A. and J. A. Curry (1997), Determination of surface turbulent fluxes over leads in Arctic sea ice, *J. Geophys. Res.*, 102(C2), 3331-3343.
- Amitrano, D., J.-R. Grasso and D. Hantz (1999), From diffuse to localized damage through elastic interaction, *Geophys. Res. Lett.*, 26, 2109–2112.
- Batchelor, G. K. (1951), Diffusion in a field of homogeneous turbulence, 2, The relative motion of particles, *Proc. Cambridge Philos. Soc.*, 48, 345-362.
- Batchelor, G. K. (1960), The theory of Homogeneous Turbulence, 197 pp., Cambridge University Press.
- Bauer, S., M. S. Swenson, A. Griffa, A. J. Mariano and K. Owens (1998), Eddy-mean flow decomposition and eddy-diffusivity estimates in the Tropical Pacific Ocean, 1, Methodology, *J. Geophys. Res.*, 103, 30,855-30,871.
- Biferale, L., G. Boffeta, A. Celani, A. Lanotte and F. Toschi (2006), Lagrangian statistics in fully developed turbulence, *J. Turb.*, 7(6).
- Bouchaud, J. P. and A. Georges (1990), Anomalous diffusion in disordered media, *Phys. Rep.*, 195, 127.
- Bourgoin, M, N. T. Ouellette, H. Xu, J. Berg and E. Bodenschatz (2006), The role of pair dispersion in turbulent flow, *Science*, 311, 835-838.
- Chapman, W. L. and J. E. Walsh (2003), Observed climate change in the Arctic, updated from Chapman and Walsh, 1993. Recent variations of sea ice and air temperatures in high latitudes, *Bull. Am. Meteor. Soc.*, 74(1), 33-47.
- Colin de Verdière, A. (1983), Lagrangian eddy statistics from surface drifters in the eastern North Atlantic, *J. Mar. Res.*, 41, 375-398.
- Colony, R. and A. S. Thorndike (1980), The horizontal coherency of the motion of summer Arctic sea ice, *J. Phys. Ocean.*, 10, 8, 1281-1289.
- Colony, R. and A.S. Thorndike (1984), An estimate of the mean field of Arctic sea ice motion, *J. Geophys. Res.*, 89(C6), 10,623-10,629.
- Comiso, J. C. (2001), Satellite observed variability and trend in sea ice extent, surface temperature, albedo, and clouds in the Arctic, *Ann. Glaciol.*, 33, 457-473.

- Comiso, J. C. (2002), A rapidly declining Arctic perennial ice cover, *Geophys. Res. Lett.*, 29(20), 1956, doi:10.1029/2002GL015650.
- Comiso, J. C. (2003a), Warming trends in the Arctic, *J. Clim.*, 16(21), 3498-3510.
- Comiso, J. C., D. J. Cavalieri and T. Markus (2003b), Sea ice concentration, ice temperature, and snow depth, using AMSR-E data, *IEEE TGRS*, 41(2), 243-252.
- Comiso, J. C. (2005), Impacts of the variability of 2nd year ice types on the decline of the perennial ice cover, *Ann. Glaciol.*, 44.
- Comiso, J. C. (2006), Abrupt decline in the Arctic winter sea ice cover, *Geophys. Res. Lett.*, 33, L18504, doi:10.1029/2006GL027341.
- Coon M., G. A. Maykut, R. S. Pritchard, D. A. Rothrock and A. S. Thorndike (1974), Modeling the pack ice as an elastic-plastic material, *AIDJEX Bull.*, 24:1–105.
- Coon, M. et al. (2007), Arctic Ice Dynamics Joint Experiment (AIDJEX) assumptions revised and found inadequate, *J. Geophys. Res.*, 112, C11S90, doi:10.1029/2005JC003393.
- Cowie, P. A., D. Sornette and C. Vanneste (1995), Multifractal scaling properties of a growing fault population, *Geophys. J. Int.*, 122(2), 457-469.
- Davis, R. E. (1985), Drifter observations of coastal Surface currents during CODE: The statistical and dynamical views, *J. Geophys. Res.*, 90(C3), 4756–4772.
- Deser, C., and H. Teng (2008), Evolution of Arctic sea ice concentration trends and the role of atmospheric circulation forcing, *Geophys. Res. Lett.*, 35, L02504, doi:10.1029/2007GL032023.
- Dudko, Y. V. (1999), Analysis of seismo-acoustic emission from ice fracturing events during SIMI'94, in *Oceanographic Engineering*, Massachusetts Institute of Technology: Boston, MA.
- Einstein, A. (1905), Investigations on the theory of the Brownian motion, *Ann. Phys.*, 17, 549-560.
- European Centre for Medium-Range Weather Forecasts (2004), ERA-40 reanalysis, http://data.ecmwf.int/data/d/era40_mnfh/.
- Figueroa, H. A. and D. B. Olson (1994), Eddy resolution versus eddy diffusion in a double gyre GCM. Part I: The Lagrangian and Eulerian description, *J. Phys. Oceanogr.*, 24, 371-386.
- Freeland, H. J., P. B. Rhines and T. Rossby (1975), Statistical observations of the trajectories of neutrally buoyant floats in the North Atlantic, *J. Mar. Res.*, 33, 383-404.
- Frisch, U. (1995), Turbulence: the legacy of A.N Kolmogorov, *Cambridge Univ. Press*.
- Gandin, L. S. (1963), The objective analysis of meteorological fields Leningrad, *Hydrometeorological Publishing House*.

- Gascard, J. C. et al. (2008), Exploring arctic transpolar drift during dramatic sea ice retreat, *Eos Trans. AGU*, 89(3), doi:10.1029/2008EO030001.
- Gifford, F. (1955), A simultaneous Lagrangian-Eulerian turbulence experiment, *Mon. Wea Rev.*, 83, 12, 293-301.
- Girard, L., J. Weiss, J. M. Molines, B. Barnier and S. Bouillon, Evaluation of sea ice models on the basis of statistical and scaling properties of Arctic sea ice deformation, **in prep.**
- Hanna, S. R. (1980), Lagrangian and Eulerian time-scale relations in the daytime boundary layer, *J. App. Meteor.*, 20, 242-249.
- Hay, J. S. and F. Pasquill (1959), Diffusion from a continuous source in relation to the spectrum and scale of turbulence, *Advances in Geophysics*, 6, Academic Press, 345-365.
- Haynes, R., and E. D. Barton (1991), Lagrangian observations in the Iberian coastal transition zone, *J. Geophys. Res.*, 96(C8), 14,731-14,741.
- Heil, P., and W. D. Hibler (2002), Modeling the high-frequency component of Arctic sea ice drift and deformation, *J. Phys. Oceanogr.*, 32, 3039–3057.
- Hibler, W. D. (1977), A viscous sea ice law as a stochastic average of plasticity, *J. Geophys. Res.*, 82(27).
- Hibler, W. D. (1979), A dynamic thermodynamics sea ice model, *J. Phys. Ocean.*, 9, 815-846.
- Hibler, W. D. and E. Schulson (2000), On modelling the anisotropic failure and flow of flawed sea ice, *J. Geophys. Res.*, 105, 17,105-17,120.
- Hunke, E. C. and J. K. Dukowicz (1997), An elastic-viscous-plastic model for sea ice dynamics, *J. Phys. Oceanogr.*, 27(9), 1849-1867.
- Hunkins, K. (1967), Some inertial oscillations of Fletcher's Ice Island, *J. Geophys. Res.*, 72, 1165-1174.
- Hurrell, J. W. (1995), Decadal trends in the North Atlantic Oscillation: Regional temperatures and precipitation, *Science*, 269, 676-679.
- Hutchings, J., P. Heil and W. D. Hibler (2005), Modeling linear kinematic features in sea ice, *Month. Weather Rev.*, 133, 3481-3497.
- International Arctic Buoy Program, <ftp://iabp.apl.washington.edu/pub/IABP/C>.
- Jullien, M. C., J. Paret and P. Tabeling (1999), Richardson pair dispersion in two-dimensional turbulence, *Phys. Rev Lett.*, 82(14).
- Kraichnan, R. H. (1966), Dispersion of Particle pairs in Homogeneous Turbulence, *Phys. Fluids*, 9, 1937-1943.
- Krauss, W., and R. H. Käse (1984), Mean circulation and eddy kinetic energy in the eastern North Atlantic, *J. Geophys. Res.*, 89, 3407-3415.

- Krauss, W., and C. W. Böning (1987), Lagrangian properties of eddy fields in the northern North Atlantic as deduced from satellite-tracked buoys, *J. Mar. Res.*, 45, 259-291, 1987.
- Kwok, R. (1998), The RADARSAT geophysical processor system, in *Analysis of SAR Data of the Polar Oceans*, edited by C. R. Tsatsoulis and R. Kwok, Springer-Verlag, 235-237.
- Kwok, R. and D.A. Rothrock (1999), Variability of Fram Strait ice flux and North Atlantic Oscillation, *J. Geophys. Res.*, 104, 5177-5189.
- Kwok, R. (2001), Deformation of the Arctic ocean sea ice cover between November 1996 and April 1997: a qualitative survey, in *Scaling Laws in Ice Mechanics*, edited by H. H. Shen, Kluwer Academic, 315-322.
- Kwok, R. (2004), Annual cycles of multiyear sea ice coverage of the Arctic Ocean: 1999–2003, *J. Geophys. Res.*, 109, C11004, doi:10.1029/2003JC002238.
- Kwok, R. (2006), Contrasts in sea ice deformation and production in the Arctic seasonal and perennial ice zones, *J. Geophys. Res.*, 111, C11S22, doi:10.1029/2005JC003246.
- Lemke, P. et al. (2007), Observations: Changes in Snow, Ice and Frozen Ground. In: Climate Change 2007: The Physical Science Basis. Contribution of Working Group I to the Fourth Assessment Report of the Intergovernmental Panel on Climate Change. Cambridge University Press, Cambridge, United Kingdom and New York, NY, USA.
- Lien, R-C., E. A. D'Asaro and G. T. Dairiki (1998), Lagrangian frequency spectra of vertical velocity and vorticity in high-Reynolds-number oceanic turbulence, *J. Fluid Mech.*, 362, 177.
- Lindsay, R. W. and D. A. Rothrock (1995), Arctic sea ice leads from advanced very high-resolution radiometer images, *J. Geophys. Res.*, 100(C3), 4533-4544.
- Lindsay, R., J. Zhang and D. Rothrock (2003), Sea-ice deformation rates from satellite measurements and in a model, *Atmosphere-Ocean*, 41, 35-47.
- Lindsay, R. and J. Zhang (2005), The thinning of Arctic sea ice, 1988-2003: Have we passed a Tipping Point?, *J. Clim.*, 18, 4879-4894.
- Lindsay, R., J. Zhang, A. Schweiger, M. Steele and H. Stern (2008), Arctic sea ice retreat in 2007 follows thinning trend, *J. Clim.*, doi:10.1175/2008JCLI2521.
- Lüpkes, C., T. Vihma, G. Birnbaum and U. Wacker (2007), The influence of leads in sea ice on the temperature of the atmospheric boundary layer during polar night, *Geophys. Res. Lett.*, 35, L03805, doi:10.1029/2007GL032461.
- Maslowski, W. and W. Lipscomb (2003), High resolution simulations of Arctic sea ice, 1979-1993, *Polar Research*, 22, 67-74.
- McBean, et al. (2005), Chapter 2: Arctic climate: Past and present, in *Arctic Climate Impact Assessment report*.

- McPhee, M. G. (1978), A simulation of inertial oscillations in drifting pack ice, *Dyn. Atmos. Oceans*, 2, 107-122.
- McPhee, M. G., and L.H. Kantha (1989), Generation of internal waves by sea ice, *J. Geophys. Res.*, 94(C3), 3287–3302.
- Marsan, D., J. Weiss, R. Lindsay and H. Stern (2004), Scale dependence and localization of the deformation of Arctic sea ice, *Phys. Rev. Lett.*, 93, 17.
- Martin, S., and A. S. Thorndike (1985), Dispersion of sea ice in the Bering Sea, *J. Geophys. Res.*, 90(C4), 7223-7226.
- Martins, C. S., M. Hamann and A. F. G. Fiúza (2002), Surface circulation in the Eastern North Atlantic from drifters and altimetry, *J. Geophys. Res.*, 107(C12), 3217.
- Maykut, G. A., and N. Untersteiner (1971), Some results from a time-dependent thermodynamic model of sea ice, *J. Geophys. Res.*, 76(6), 1550–1575.
- Maykut, G. A. (1982), Large-scale heat exchange and ice production in the central Arctic, *J. Geophys. Res.*, 87(C10), 7971-7984.
- Mordant, N., J. Delour, E. Léveque, O. Michel, A. Arnéodo and J.-F. Pinton (2003), Lagrangian velocity fluctuations in fully developed turbulence: scaling, intermittency, and dynamics, *J. Stat. Phys.*, 113, 516
- Morel, P. and M. Larchevèque (1974), Relative dispersion of constant-level balloons in the 200-mb general circulation, *J. Atmos. Sc.*, 31, 2189-2196.
- Moritz, R. E. and H. L. Stern (2001), Relationships between geostrophic winds, ice strain rates and the piecewise rigid motions of pack ice, in *Scaling Laws in Ice Mechanics and Ice Dynamics*, edited by J. P. Dempsey and H. H. Shen, Kluwer Academic Publishers: Dordrecht. p. 335-348.
- Moritz, R. E., C. M. Bitz and E. J. Steig (2002), Dynamics of recent climate change in the Arctic, *Science*, 297, 1497-1502.
- National Weather Service, NOAA, <http://www.cpc.ncep.noaa.gov/products/>.
- Nghiem, S. V., I. G. Rigor, D. K. Perovich, P. Clemente-colon and J. W. Weatherly (2007), Rapid reduction of Arctic perennial sea ice, *Geophys. Res. Lett.*, 34, L19505, doi:10.1029/2007GL031138.
- Nye, J.F. (1973), Is there any physical basis for assuming linear viscous behaviour for sea ice?, *AIDJEX Bulletin #21*, 18-19, July.
- Okubo, A. (1971), Oceanic diffusion diagrams, *Deep Sea Res.*, 18, 789-802.

- Overland, J. E., M.C. Spillane, D. B. Percival, M. Wang and H. Mojfeld (2004), Seasonal and regional variation of pan-Arctic surface air temperature over the instrumental record, *J. Clim.*, 17, 17, 3263-3282.
- Pavlov, V. K. and O. A. Pavlova (2007), Increasing sea ice drift velocities in the Arctic Ocean, 1979-2005, *Geophys. Rev. Abst.*, 9, 07124.
- Perovich, D. K., J. A. Richter-Menge, K. F. Jones, and B. Light (2008), Sunlight, water, and ice: Extreme Arctic sea ice melt during the summer of 2007, *Geophys. Res. Lett.*, 35, L11501, doi:10.1029/2008GL034007.
- Polar Remote Sensing Group, <http://www-radar.jpl.nasa.gov/rgps/>.
- Poulain, P.-M., and P. P. Niiler (1989), Statistical Analysis of the surface circulation in the California current system using satellite-tracked drifters, *J. Phys. Ocean.*, 19, 1588-1603.
- Poulain, P.-M., A. Warn-Varnas, and P. P. Niiler (1996), Near-surface circulation of the Nordic seas as measured by Lagrangian drifters, *J. Geophys. Res.*, 101, 18,237-18,258.
- Qureshi, N.M, M. Bourgoin, C. Baudet, A. Cartellier and Y. Gagne (2007), Turbulent transport of material particles: An experimental study of finite size effects, *Phys. Rev. Lett.*, 99, 184502.
- Rampal, P., J. Weiss, D. Marsan, R. Lindsay and H. Stern (2008), Scaling properties of sea ice deformation from buoy dispersion analysis, *J. Geophys. Res.*, 113, C03002, doi:10.1029/2007JC004143.
- Richardson, L. F. (1926), Atmospheric diffusion shown on a distance-neighbour graph., *Proc. R. Soc. London, A110*, 709-737.
- Richardson, L. F. and H. Stommel (1949), Note on eddy diffusion in the sea, *J. Meteorol.*, 5, 238-240.
- Richter-Menge, J. et al. (2006), State of the Arctic Report. NOAA OAR Special Report, NOAA/OAR/PMEL, Seattle, WA, 36 pp.
- Rigor, I., R. Colony and S. Martin (2000), Variations in surface air temperature observations in the Arctic, 1979 - 1997, *J. Climate*, 13, 5, 896-914.
- Rigor, I. G. et al. (2002), On the response of sea ice to the Arctic Oscillation, *J. Clim.*, 15(18), 2546-2663.
- Riser, S. C., and H. T. Rossby (1983), Quasi-Lagrangian structure and variability of the subtropical western North Atlantic circulation, *J. Mar. Res.*, 41, 127-162.
- Rothrock, D., Y. Yu and G. A. Maykut (1999), Thinning of the Arctic sea-ice cover, *Geophys. Res. Lett.*, 26, 3469-3472.

- Rothrock, D., D. B. Percival and M. Wensnahan (2008), The decline in arctic sea-ice thickness: Separating the spatial, annual, and interannual variability in a quarter century of submarine data, *J. Geophys. Res.*, 113, C05003, doi:10.1029/2007JC004252.
- Sawford, B. L. (1991), Reynolds number effects in Lagrangian stochastic model of turbulent dispersion, *Phys. Fluids A*, 3(6), 1577-1586.
- Schmitt, F. (2006), Linking Eulerian and Lagrangian structure function's scaling exponents in turbulence, *Physica A*, 368, 2.
- Scholz, C. H. and P. A. Cowie (1990), Determination of total strain from faulting using slip measurements, *Nature*, 346, 837-839.
- Schluson, E. M. (2004), Compressive shear faults within the arctic sea ice: Fracture on scales large and small, *J. Geophys. Res.*, 109, C07016, doi:10.1029/2003JC002108.
- Serreze, M. C. et al. (2003). A new record minimum Arctic sea ice and extent in 2002, *Geophys. Res. Lett.*, 30, 1110, doi:10.1029/2002GL016406.
- Serreze, M. C., M. M. Holland and J. Stroeve (2007), Perspectives on the Arctic's shrinking sea-ice cover, *Science*, 315, 1533-1536.
- Sornette, D. (2000), Critical phenomena in natural sciences, Springer Series in Synergetics, Berlin: Springer.
- Spall, M. A., P. L. Richardson and J. Price (1993), Advection and eddy mixing in the Mediterranean salt tongue, *J. Mar. Res.*, 51, 797-818.
- Steele, M., J. Zhang, D. Rothrock and H. Stern (1997), The force balance of sea ice in a numerical model of the Arctic Ocean, *J. Geophys. Res.*, 102, 21,061-21,079.
- Steele, M., W. Ermold and J. Zhang (2008), Arctic ocean surface warming trends over the past 100 years, *Geophys. Res. Lett.*, 35, L02614, doi: 10.1029/2007GL031651.
- Stern, H. and R. E. Moritz (2002), Sea ice kinematics and surface properties from RADARSAT synthetic aperture radar during the SHEBA drift, *J. Geophys. Res.*, 107, doi:10.1029/2000JC000472.
- Stroeve, J. C. et al. (2005), Tracking the Arctic's shrinking ice cover: Another extreme September minimum in 2004. *Geophys. Res. Lett.*, 32, doi:10.1029/2004GL021810.
- Stroeve, J., M. M. Holland, W. Meier, T. Scambos and M. C. Serreze (2007), Arctic sea ice decline: Faster than forecast, *Geophys. Res. Lett.*, 34, L09501, doi:10.1029/2007GL029703.
- Stroeve, J., et al. (2008), Arctic sea ice extent plummets in 2007, *Eos Trans. AGU*, 89(2), doi:10.1029/2008EO020001.

- Sundermeyer, M. A., and J. F. Price (1998), Lateral mixing and the North Atlantic tracer release experiment: Observations and numerical simulations of Lagrangian particles and a passive tracer, *J. Geophys. Res.*, 103, 21,481-21,497.
- Taylor, G. I. (1921), Diffusion by continuous movements, *Proc. London Math. Soc.*, (20), Ser. 2.
- Thomas, D. (1999), The quality of sea ice velocity estimates, *J. Geophys. Res.*, 104(C6), 13,627-13,655.
- Thompson, D. W. J. and J. M. Wallace (1998), The Arctic oscillation signature in the wintertime geopotential height and temperature fields, *Geophys. Res. Lett.*, 25(9), 1297-1300.
- Thorndike A. S., and R. Colony (1982), Sea ice motion in response to geostrophic winds, *J. Geophys. Res.*, 87(C8), 5845-5852.
- Thorndike, A.S. (1986a), Sea Ice Kinematics, *Geophysics of Sea Ice*, edited by N. Untersteiner, Plenum, New York.
- Thorndike, A. S. (1986b), Diffusion of Sea ice, *J. Geophys. Res.*, 91(C6), 7691-7696.
- Timmermann, R., H. Goose, G. Madec, T. Fichefet, C. Ethe and V. Dulire (2005), On the representation of high latitude processes in the orca-lim global coupled sea ice-ocean model, *Ocean Modeling*, 8, 175-201.
- Tucker, W. B. III, J. W. Weatherly, D. T. Eppler, L. D. Farmer and D. L. Bentley (2001), Evidence for rapid thinning of sea ice in the western Arctic Ocean at the end of the 1980s, *Geophys. Res. Lett.*, 28, 2851-2854.
- Van Atta, C. W., and W. Y. Chen (1970), Structure functions of turbulence in the atmospheric boundary layer over the ocean, *J. Fluid Mech.*, 44, 145-159.
- Voth, G. A., K. Satyanarayan and E. Bodenschatz (1998), Lagrangian acceleration measurements at large Reynolds numbers, *Phys. Fluids*, 10, 2268.
- Weiss, J. (2003), Scaling of fracture and faulting in ice on Earth, *Surveys of Geophysics*, 24, 185-227.
- Weiss, J., and D. Marsan (2004), Scale properties of sea ice deformation and fracturing, *C. R Physique* 5.
- Weiss, J., E. M. Schulson, and H. Stern (2007), Sea ice rheology from in-situ, satellite and laboratory observations: Fracture and friction, *Earth Planet. Sci. Lett.*, 255, 1-8.
- Weiss, J. (2008a), Intermittency of principal stress directions within Arctic sea ice, *Phys. Rev. Lett.* E, 77, doi:10.1103/PhysRevE.77.056101.
- Weiss, J., D. Marsan and P. Rampal (2008b), Space and time scaling laws induced by the multiscale fracturing of the Arctic sea ice cover, in *Scaling in solid mechanics*, edited by F. Borodich, Springer, New York.

Wells, D. L. and K. J. Coppersmith (1994), New empirical relationships among magnitude, rupture length, rupture width, rupture area, and surface displacement. *Bull. Seism. Soc. Am.*, 84(4), 974-1002.

Yaglom, A. M. (1966), The influence on the fluctuation in energy dissipation on the shape of turbulent characteristics in the inertial interval, *Sov. Phys. Dokl.*, 2, 26.

Zhang, J., D. Rothrock, and M. Steele (2000), Recent changes in Arctic sea ice: the interplay between ice dynamics and thermodynamics, *J. Clim.*, 13, 3099-3114.

Zhang, H-M. (2001), Isopycnal lagrangian statistics from the North Atlantic Current RAFOS float observations, *J. Geophys. Res.*, 106(C7), (13) 816-836.

Annexe :

Space and time scaling laws induced by the multiscale fracturing of the Arctic sea ice cover

D'après :

Weiss, J., D. Marsan and **P. Rampal** (2008) Space and time scaling laws induced by the multiscale fracturing of the Arctic sea ice cover, in *Scaling in Solids Mechanics*, P. Borodich Ed..

Abstract:

Recent analyses of in-situ and satellite observations of arctic sea ice stresses and strain-rates revealed a highly intermittent and heterogeneous dynamics characterized by temporal and spatial scaling laws, a vision at odds with the classical smooth, fluid-like modeling framework of the sea ice cover. We propose here a simple multiscale fracturing model that explains the observed scaling properties of the deformation fields from the fractal properties of fracturing.

1. Introduction

The arctic sea ice cover, which extends during winter over about 14 million km² and shrinks to 7 million km² at the end of summer, with an average thickness of a few meters, can be considered as a very thin solid plate that deforms and fractures under the action of winds, ocean currents, thermal stresses and boundary conditions (coasts). Consequently, plane stress conditions are fulfilled and the ice cover can be considered as a 2D geophysical object. Sea ice deformation and fracturing are important, as they largely control the thickness distribution, the concentration of open water, and thus the global sea ice mass balance, which are important climatic parameters. Indeed, the sea ice cover insulates the ocean from the atmosphere: for an ice cover fractured at 0.5%, 50% of the thermodynamic and radiative fluxes take place along these fractures [*Heil and Hibler, 2002*]. Consequently, sea ice models have been implemented into climate models to be coupled to ocean and atmospheric models.

The classical modelling framework for sea ice dynamics is based on continuum mechanics and a viscous-plastic rheology [*Hibler, 1979*]. This rheology implies that for stress states inside the plastic yield curve the mechanical behaviour is that of a viscous fluid, while the ice flows as a perfect plastic when the stress reaches the yield curve, without further increase of the stress. This framework has been widely used as it is suited for a numerical coupling with oceanic and atmospheric models. By construction, this continuum mechanics approach homogenizes the properties at the model's discretization scale. This fluid-like view seems at odds with in-situ and satellite observations that reveal a highly fractured sea ice cover [*Schulson, 2004, Weiss and Marsan, 2004*] characterized by a highly intermittent and heterogeneous deformation process. Deformation is localized along linear features [*Moritz and Stern, 2001*] that are active Coulombic faults [*Schulson, 2004, Weiss et al., 2007*]. From an analysis of in-situ stress data and satellite-derived strain-rates, it has been shown recently that the average effect of many faulting events does not give rise to an (apparent) viscous behaviour, even at large spatial (> 300 km) and time (> 1 month) scales [*Weiss et al., 2007*]. Instead, the interplay of various fracturing episodes at various scales generates complex deformation fields, intermittency (from seconds to months), as well as spatial heterogeneity (from meters to hundreds of km). Here, we first show that this complexity is characterized by space and time scaling laws that mimic the scaling laws of fluid turbulence, although the power law exponents differ, as the physical mechanisms responsible for dispersion/deformation strongly differ. Then, we propose a simple statistical model of multiscale fracturing that allows us to reproduce these scaling laws and therefore argue for an elasto-brittle

behaviour of the sea ice cover [Weiss *et al.*, 2007; Nye, 1973], whose deformation is accommodated by a hierarchy of faulting events.

2. Scaling of sea ice dispersion and deformation

Like molecules in a gas or a turbulent fluid, nearby pieces of sea ice gradually move apart as the result of deformation [Martin and Thorndike, 1985; Rampal *et al.*, 2008]. In the case of fluid turbulence, it is customary to characterize this dispersion by the mean square change in separation r of pairs of fluid particles, $\langle \Delta r^2 \rangle$. For 3D fully developed turbulence, Richardson [1926] proposed the time scaling, $\langle \Delta r^2 \rangle \sim t^3$. In the case of the arctic sea ice cover considered as a solid plate, it seems more pertinent to translate this dispersion in terms of a deformation rate \dot{S} , which scales as $\dot{S} \sim \langle (\Delta r / R)^2 \rangle^{1/2} / t$, where R is the (initial) separation of the pair. Rampal *et al.* [2008] applied this methodology to a set of about 500 trajectories of drifting buoys of the International Arctic Buoy Program, deployed in the Arctic between 1979 and 2001 and corresponding to 680 pairs of buoys working simultaneously, in order to analyze the scaling properties of sea ice deformation. Although S only depends on deformation, i.e. not on solid rotation, the full strain-rate tensor cannot be determined from pairs of trajectories, i.e. shear and divergence cannot be discriminated on this basis. Using binning in space and time of this dataset, they obtained the following temporal and spatial scaling.

The temporal scaling of sea ice strain-rate \dot{S} is characterized by:

$$\dot{S} \sim t^{-\alpha(R)} \quad (A-1)$$

where the power law exponent $\alpha(R)$ decreases with increasing spatial scale (initial separation), from $\alpha = 0.89$ for $R \sim 1$ km to $\alpha = 0.30$ for $R \sim 300$ km in winter (respectively 0.87 and 0.25 for summer). Relation (1) expresses the intermittency of the process. Indeed, a non-intermittent viscous flow would be characterized by $\alpha = 0$, whereas the boundary value $\alpha = 1$ would correspond to a deformation accommodated by a single cracking event. Although the intermittent character, i.e. α , decreases towards large spatial scales as the result of averaging an increasing number of fracturing events, sea ice deformation does not mimic viscous flow even at scales close to the Arctic basin scale.

On the other hand, the following spatial scaling is obtained:

$$\dot{S} \sim R^{-\beta(t)}$$

where the exponent $\beta(t)$ decreases with increasing time scale, from $\beta=0.85$ for $t \sim 1$ hour to $\beta=0.35$ for $t \sim 1$ month in winter (respectively 0.85 and 0.42 for summer). In this case, β expresses the degree of heterogeneity of sea ice deformation, bounded by $\beta=2$ for a deformation localized along a single fracture, and by $\beta=0$ for a homogeneous deformation field (e.g. elastic or viscous). Sea ice deformation appears more homogeneous as one increases the time scale and therefore the number of fracturing events, but a significant heterogeneity remains even at the scale of months. This spatial scaling is in full agreement with a previous work [Marsan *et al.*, 2004] that analyzed the scaling properties of the sea ice strain-rate field measured from successive SAR satellite images, at the time scale of 3 days (the time scaling was not considered in this work).

Relations (A-1) and (A-2) therefore express the strongly intermittent and heterogeneous character of sea ice deformation, as well as the complex space/time coupling illustrated by the dependence of α on R and β on t . In what follows, using a simple multiscale statistical model of sea ice fracturing, we argue that these coupled scaling laws are the fingerprints of a deformation process accommodated by discrete fracturing events at various scales.

3. A multiscale statistical model of sea ice fracturing and deformation

We consider here that nearly all the sea ice deformation is accommodated by multiple fracturing and faulting events at various scales, i.e. the contribution of dislocation-related creep is negligible [Weiss *et al.*, 2007]. To each event of length L is associated an offset u , averaged along L . In this simple scalar model, the fracture modes are undifferentiated, i.e. u can represent an opening for a tensile fracture, a shear offset for a shear fault, or convergence during a ridging event. Here, u represents the offset resulting from a brief, transient episode of fracturing, and not the total displacement that could accumulate along a fault over a long time as the result of multiple episodes. In agreement with the aspect ratio of the ice cover, the model is 2D, i.e. the thickness w of the fractures is considered to be constant and corresponds to the ice cover thickness. The model is isotropic and does not consider fracture orientations. The idea that sea ice dispersion and deformation could be accommodated by the offsets of multiple fracturing events was already proposed by Thorndike [1986]. However, this author considered a Poisson distribution of events in space and time, i.e. assumed that sea ice fracturing was a purely random process without space and/or time correlations, in disagreement with observations now available (see below). In addition, he associated for simplicity to each event a constant offset $u_0 = 2$ km. In what follows, we consider a more complex situation characterized by a wide distribution of event sizes as well as fractal patterns in space and time, i.e. long-range correlations.

Spatial scaling of deformation is considered first. The strain increment ε induced by a fracturing event of length L and offset u over a region of size R (i.e. of area R^2) is:

$$\varepsilon = \frac{u}{L} \times \frac{L^2}{R^2} = \frac{uL}{R^2} \quad (\text{A-3})$$

Following earlier work on Earth's crust faulting (e.g. Scholz and Cowie [1990]), we then assume that u is proportional to L , i.e. $u = \gamma L$. For the Earth's crust, γ is around 10^{-5} [Wells and Coppersmith, 1994]. This proportionality is compatible with fracture mechanics principles, but γ is unknown for the sea ice cover and possibly depends on the driving stress.

We then consider a fractal fracture pattern characterized by a number of event barycenters within a region of area R^2 , $N(R)$, scaling as:

$$N(R) \sim R^D \quad (\text{A-4})$$

where $0 \leq D \leq 2$ is a fractal dimension. As shown later, D might depend on the time scale considered, t , as an increasing t implies a decreasing clustering of the events as correlations weaken, or, in other words, a “densification” of the fracture network. Such a fractal pattern is in qualitative agreement with the fractal character of fracture networks as observed from satellite image [Weiss and Marsan, 2004], as well as with power law distributions of fracture spacing revealed from an analysis of high resolution radiometer images [Lindsay and Rothrock, 1995; Weiss, 2003]. To estimate the deformation accumulated over the region, we need to know the probability density function (pdf) of the strain increments ε , $f(\varepsilon)$, i.e., following (A-3), the pdf of the faulted surfaces $u \times L$. The length L refers to a length involved in a transient fracturing event, and u is a kinematic parameter. It is therefore impossible to estimate $f(\varepsilon)$ from “static” photographs. An alternative way is to consider seismic data. Like faulting events within the Earth’s crust generating earthquakes, sea ice fracturing events generate icequakes whose magnitude is a measure of the event size. However, seismic experiments over the sea ice cover are extremely scarce. To the authors’ knowledge, only the work of Dudko [1995] provided a significant dataset of icequakes magnitudes m , characterized by the following pdf:

$$f(m) \sim 10^{-bm} \quad (\text{A-5})$$

with $b \approx 1.25$ [Weiss and Marsan, 2004]. This is very similar to the Gutenberg-Richter law for earthquakes, with the difference that $b \approx 1$ is generally reported for the crust. Following what is well documented for earthquakes, we assume that the icequake magnitude is related to the seismic moment M through:

$$M \sim 10^{am} \quad (\text{A-6})$$

with $a = 1.5$, and that M is related to u and L through:

$$M = wuL \quad (\text{A-7})$$

i.e., M represents a faulted surface $N(R)$ (as w is constant here) that becomes a deformation increment after normalization by the considered area R^2 (see (A-3)). Combining (A-5) and (A-6), we obtain the pdf of M :

$$f(M) \sim M^{-1-b/a} \quad (\text{A-8})$$

We now assume that, for a given time interval t , the deformation of a region of area R^2 results from the cumulative effect of $N(R)$ independent events distributed following (A-8). As the pdf of the seismic moments, i.e. of $u \times L$, is a Lévy law of parameter $b/a < 2$ (relation (A-8)), the total faulted surface ΣR scales as [Sornette, 2000]:

$$\Sigma R \sim N(R)^{\frac{a}{b}} \sim R^{\frac{a}{b}} \quad (\text{A-9})$$

Therefore, the strain $\varepsilon(R)$ reads:

$$\varepsilon(R) = \frac{\Sigma(R)}{R^2} \sim R^{\frac{a}{b}-2} \quad (\text{A-10})$$

The same scaling will be obtained for the strain-rate $\varepsilon(R)/t$, as t is a constant here. The above expression has the form of relation (A-2), with:

$$\beta(t) = 2 - D \frac{a}{b} \quad (\text{A-11})$$

Therefore, this simple model of multiscale fracturing is able to reproduce the observed spatial scaling of sea ice deformation rate, as long as the fractal dimension D increases with increasing time scale. This increase of D expresses a memory effect of the system that slowly weakens with time: being on a fracture at time $t=0$, nothing can be said about the initiation of fractures nearby at $t=\infty$ (years), and $D \rightarrow 2$. At the time scale of a few hours, $\beta=0.85$ for both winter and summer. Taking $a=1.5$ and $b=1.25$ (see above), this corresponds to $D=0.96$, suggesting that at these short time scales the fracturing events organize in space along 1D-like features. This is significantly different from the boundary value $D=0$ corresponding to an isolated event, suggesting that the transient fracturing episodes occur at much shorter time scales than a few hours. At long time scales (months), $\beta=0.35$ in winter and 0.42 in summer, corresponding respectively to $D=1.38$ and 1.32. This is significantly below the boundary value $D=2$ corresponding to a dense, homogeneously distributed (Poisson) network. A memory effect remains within the system after several months. This is another way to express the heterogeneous character of sea ice deformation and fracturing up to very large time scales.

We now consider the temporal scaling of sea ice deformation rate. Compared to what has been detailed above, an additional hypothesis is introduced: for a given region of area R^2 , the deformation over this region during the time t results from the cumulative effect of $N(t)$ independent events (i.e. the size of event of rank n is independent of the size of events $n-1$ or $n+1$) distributed following (A-8), with $N(t)$ following:

$$N(t) \sim t^\delta \quad (\text{A-12})$$

with $0 \leq \delta \leq 1$. This fractal scaling is in agreement with the power law scaling of the power spectrum of in-situ ice stress records [Weiss and Marsan, 2004]. The boundary value $\delta=0$ would correspond to an isolated event, whereas $\delta=1$ represents the Poisson hypothesis of purely random, uncorrelated events, i.e. the situation assumed by Thorndike [1986]. Following (A-3), as the area R^2 is considered here as a constant, the pdf of the strain increments ε has the form of (A-8), i.e. $f(\varepsilon) \sim \varepsilon^{-1-b/a}$. Following the same argument as above about Lévy distributions, we obtain for the deformation accumulated during time t , $\varepsilon(t)$:

$$\varepsilon(t) \sim N(t)^{\frac{a}{b}} \sim t^{\frac{\delta a}{b}} \quad (\text{A-13})$$

This gives for the strain-rate:

$$\dot{\varepsilon}(t) \sim t^{\frac{\delta a - 1}{b}} \quad (\text{A-14})$$

which has the form of relation (A-1), with:

$$\alpha(R) = 1 - \delta \frac{a}{b} \quad (\text{A-15})$$

Like the fractal dimension D depending on the time scale, the exponent δ increases with increasing spatial scale R , illustrating once again the complex space/time coupling of Arctic sea ice dynamics. Indeed, at small spatial scales (1 km), $\alpha=0.89$ for winter (0.87 for summer), which leads from (A-15) to $\delta=0.09$ for winter (0.11 for summer). These values are rather small, meaning that at these small spatial scales, the deformation process is highly intermittent with bursts of events separated generally by long quiescent episodes. At very large spatial scales (a few hundreds of km), $\alpha=0.30$ for winter (0.25 for summer) corresponding to $\delta=0.58$ (0.62 for

summer). This is significantly below the boundary value $\delta=1$, meaning that the Poisson hypothesis is never pertinent, even at the scale of the Arctic basin.

4. The contribution of small *vs* large events to global sea ice deformation

Previous results [Weiss *et al.*, 2007; Rampal *et al.*, 2008; Marsan *et al.*, 2004] as well as the model detailed in section A-3 argue for a deformation of Arctic sea ice accommodated by multiple fracturing and faulting events, with a very wide range of fracture sizes, from sub-km scales to scales close to the Arctic basin scale. We can now wonder to what extent small *vs* large fractures/events contribute to the global deformation. We take the basin scale ($R \sim 2000$ km) as the reference scale, i.e. a given event of length L and offset u will result into a strain increment $\varepsilon = uL/4 \times 10^6$ if u and L are expressed in km.

We estimate first how the deformation accommodated by the fractures of size L (i.e. whose length lies between L and $L+dL$), ε_L , depends on L . As $u \sim L$ and $M \sim uL$, $L \sim M^{1/2}$. Therefore, from (A-8), the pdf of L and so the number N_L of fractures of size L scale as $L^{-1-2b/a}$. Consequently, using (A-3), we obtain:

$$\varepsilon_L = N_L \times \varepsilon(L) \sim L^{-1-\frac{2b}{a}} \times L^2 \sim L^{1-\frac{2b}{a}} \quad (\text{A-16})$$

that gives $\varepsilon_L \sim L^{-2/3}$ for $b=1.25$ and $a=1.5$. This seems to indicate that small fractures, i.e. small scales, are very important, as the contribution of fractures of size L increases with decreasing L .

On the other hand, one might have a different impression when we consider the total deformation for the full population of events, ε_{tot} . The pdf of ε has the form $f(\varepsilon) \sim \varepsilon^{-1-b/a}$ (see above). Consequently, ε_{tot} is given by:

$$\varepsilon_{tot} = \int_{\varepsilon_{min}}^{\varepsilon_{max}} f(\varepsilon) \varepsilon d\varepsilon \sim \int_{\varepsilon_{min}}^{\varepsilon_{max}} \varepsilon^{-\frac{b}{a}} d\varepsilon = \left[\frac{\varepsilon^{-\frac{b}{a}+1}}{-\frac{b}{a}+1} \right]_{\varepsilon_{min}}^{\varepsilon_{max}} \quad (\text{A-17})$$

ε_{min} corresponds to a lower bound for the scaling of relation (A-8) that might be related to a physical length scale such as the ice cover thickness (-m) or an average grain size (-cm). However, the exact value of ε_{min} is not really important here. Indeed, as $b/a < 1$, the above integral is always defined whatever ε_{min} and the global deformation is dominated by large events. To illustrate this more quantitatively, we can estimate the threshold fracture length L_{th} such that half of the deformation is accommodated by events of length $L > L_{th}$, and half by events of length $L < L_{th}$.

The upper bound ε_{\max} is set by the region scale R , as no fracture can be longer than R , i.e. $L_{\max} \sim 2000$ km in the present case. If we call ε_{th} the strain corresponding to an event of length L_{th} , we have from (A-17)

$$\varepsilon_{\max}^{-\frac{b}{a}+1} - \varepsilon_{th}^{-\frac{b}{a}+1} = \varepsilon_{th}^{-\frac{b}{a}+1} - \varepsilon_{\min}^{-\frac{b}{a}+1} = \frac{\varepsilon_{tot}}{2} \approx \varepsilon_{th}^{-\frac{b}{a}+1} \quad (\text{A-18})$$

In (A-18), we considered for simplicity that ε_{\min} was negligible compared to ε_{th} (see above). Therefore, (A-18) implies:

$$\varepsilon_{th} = 2^{\frac{a}{b-a}} \varepsilon_{\max} \quad (\text{A-19})$$

, i.e. $\varepsilon_{th} = \varepsilon_{\max}/64$ with $b=1.25$ and $a=1.5$. Then, as $\varepsilon \sim u \times L \sim L^2$ (relation (A-3)), we obtain $L_{th} = L_{\max}/8 \approx 250$ km: The fracturing events longer than 250 km dissipate half of the total deformation. We note that this estimation is independent of the proportionality coefficient γ relating u and L , which is unknown for sea ice. This strikingly illustrates the heterogeneous character of sea ice deformation, with very large events, spanning a significant part of the Arctic, contributing a lot to global deformation of the sea ice cover. It is in full agreement with the animations of strain-rate fields at the basin scale (see e.g. *Kwok* [2000]) showing intermittent, linear-like features spanning the Arctic basin.

These two points of view, expressed respectively by relations (A-16) and (A-19), might appear contradictory. Actually, they are not, but simply illustrate the fact that for such a multi-scale deformation process, small scales cannot be arbitrarily disconnected from large scales, and all are important. It is therefore not surprising that a smooth, fluid-like view of sea ice deformation does not match in-situ and/or satellite observations.

5. Conclusion

Recent analyses of in-situ and satellite observations of arctic sea ice stresses and strain-rates revealed a highly intermittent and heterogeneous dynamics characterized by temporal and spatial scaling laws, a vision at odds with the classical smooth, fluid-like modelling framework. Instead, these observations suggest an elasto-brittle behaviour of the sea ice cover, with the deformation essentially accommodated by transient fracturing events at various scales. Here, we proposed a simple multiscale fracturing model that reinforces this view, as it explains the observed scaling properties of the strain-rates from the scaling properties of fracturing. The exponents α and β , which express respectively the intermittent and heterogeneous character of sea ice deformation (relations (A-1) and (A-2)) can now be directly linked, through respectively relations (A-11) and (A-15), to the fractal exponents δ and D . The complex space/time coupling characterizing sea ice dynamics is now illustrated by the dependence of δ upon spatial scale, and of D upon time scale.

Acknowledgements We would like to thank the International Arctic Buoy Program (IABP; <http://iabp.apl.washington.edu/>) and particularly Dr. I. Rigor from APL for the buoy trajectories dataset, as well as H. Stern and an anonymous referee for valuable comments.

